Multi-Carrier Communications Over Underwater Acoustic Channels

by

Kai Tu

A Dissertation Presented in Partial Fulfillment
of the Requirements for the Degree
Doctor of Philosophy

Approved October 2011 by the
Graduate Supervisory Committee:

Tolga M. Duman, Chair
Junshan Zhang
Cihan Tepedelenlioğlu
Antonia Papandreou-Suppappola

ARIZONA STATE UNIVERSITY

December 2011

ABSTRACT

Underwater acoustic communications face significant challenges unprecedented in radio terrestrial communications including long multipath delay spreads, strong Doppler effects, and stringent bandwidth requirements. Recently, multi-carrier communications based on orthogonal frequency division multiplexing (OFDM) have seen significant growth in underwater acoustic (UWA) communications, thanks to their well well-known robustness against severely time-dispersive channels. However, the performance of OFDM systems over UWA channels significantly deteriorates due to severe intercarrier interference (ICI) resulting from rapid time variations of the channel.

With the motivation of developing enabling techniques for OFDM over UWA channels, the major contributions of this thesis include (1) two effective frequency-domain equalizers that provide general means to counteract the ICI; (2) a family of multiple-resampling receiver designs dealing with distortions caused by user and/or path specific Doppler scaling effects; (3) proposal of using orthogonal frequency division multiple access (OFDMA) as an effective multiple access scheme for UWA communications; (4) the capacity evaluation for single-resampling versus multiple-resampling receiver designs. All of the proposed receiver designs have been verified both through simulations and emulations based on data collected in real-life UWA communications experiments. Particularly, the frequency domain equalizers are shown to be effective with significantly reduced pilot overhead and offer robustness against Doppler and timing estimation errors. The multiple-resampling designs, where each branch is tasked with the Doppler distortion of different paths and/or users, overcome the disadvantages of the commonly-used single-resampling receivers and yield significant performance gains. Multiple-resampling receivers are also demonstrated to be necessary for UWA OFDMA systems. The unique design effectively mitigates interuser interference (IUI), opening up the possibility to exploit advanced user subcarrier assignment schemes. Finally, the benefits of the multiple-resampling receivers are further demonstrated through channel capacity evaluation results.

TABLE OF CONTENTS

iii

LIST OF TABLES

LIST OF FIGURES

Chapter 1

INTRODUCTION

Underwater communications refer to techniques of transmission and reception of messages below the water surface. Its applications include offshore oil industry, pollution monitoring, scientific data collection, and military use (e.g. communication between submarines) [1]. There are different technologies for underwater communications such as those through cables or optical signals; however, they all have severe limitations. Acoustic waves, in spite of the challenges they face (e.g. scarce bandwidth resources, strong Doppler effects, and large multipath delay spreads), are still the most promising means for communications below the water surface [3].

This thesis is devoted to novel system designs that cope with the challenges of UWA communications, in particular, orthogonal frequency division multiplexing based multicarrier designs are explored. Conventionally, UWA communications are based on single-carrier signaling, which usually brings the issue of intersymbol interference (ISI) due to large multipath delay spreads of the UWA channel [3]. Recently, multi-carrier signaling, which is commonly implemented in the form of orthogonal frequency division multiplexing (OFDM), has emerged as a promising alternative to the single-carrier schemes [1]. The key advantage of OFDM systems is their superior robustness to severely time dispersive channels, typical of UWA communications [4]. In fact, some encouraging results have already been obtained with OFDM systems through real-world at-sea UWA communications experiments [5–11].

The major challenge, which hinders the use of OFDM systems more pervasively in UWA communications, is the problem of inter-carrier interference (ICI) due to fast channel variations. These are caused by randomness of the propagation environment (e.g. due to sea surface movements) and by motion-induced Doppler scaling effects [1]. To tackle the ICI problem, a commonly-used receiver design adopts a two-step strategy. The first step deals with the average Doppler scaling effect that is common to all the signal arrivals [12], while the second step focuses on ICI mitigation due to the residual

1

Doppler effects [13]. Two major open problems are: (1) how a receiver should be designed when Doppler scaling effects are significantly different for different arrivals, for which compensation of the average Doppler by resampling alone will not be effective? In this case, residual Doppler effect will be significant only if the average Doppler is dealt with; (2) how the ICI mitigation stage can be improved to reduce the pilot overhead or to remove assumptions made on the statistical behavior of the UWA channel?

It is also of interest to research methods of supporting multiple users in applications such as underwater acoustic sensor networks, where the scarce UWA channel bandwidth is shared by (potentially) a large number of communication nodes [14, 15]. Currently, the research has been focused on (1) improving the overall multiuser system throughput and/or reliability, and (2) delivering multiple-access capabilities over the UWA channel to a large number of users. For these purposes, a variety of multiuser multiple-input multiple-output (MIMO) technologies and multiple-access schemes have been developed. Examples of these advancements include time-reversal mirror systems in [16], multiuser MIMO OFDM systems in [17], time division multiple access (TDMA) system in [18], and code division multiple access (CDMA) system in [19]. Two open problems in UWA multiuser communications are (1) dealing with non-stationary users (bringing the challenge of user-specific Doppler effects), and (2) investigation of orthogonal frequency division multiple access (OFDMA) as a candidate scheme for multiple access over the UWA channels.

With the motivation of delivering enabling techniques for OFDM for UWA communications, in this thesis, we invent various OFDM receiver designs coping with the severe ICI induced by fast UWA channel variations. We also extend our results to multiuser communication scenarios, where the focus is on dealing with ICI and inter-user interference (IUI) resulting from user-specific Doppler scaling effects. Furthermore, the channel capacity offered by the proposed receiver designs are evaluated and compared with those associated with the conventional designs, yielding general design guidelines for future systems.

1.1 Contributions of the Thesis

The key contributions of this thesis are summarized as following. To address the problem of effective ICI mitigation, we design two adaptive frequency-domain (FD) equalizers, namely the FD-DFE (decision feedback equalizer) and the FD-MMSE (linear minimum mean squared error equalizer). Exploiting the tentative decisions obtained from the standard detector that neglects the ICI, both equalizers improve the detection performance through adaptive equalization across the subcarriers. They are also seamlessly integrated with a specially designed phase tracking loop, which properly handles the phase rotations (of the equalizer coefficients) due to timing synchronization errors. The effectiveness of the proposed schemes is demonstrated not only with simulated conditions but also with real data collected in the KAM08 (Kauai Acomms MURI 2008) shallow water acoustic communications experiment.

Responding to the challenges posed by the path and/or user-specific Doppler scaling effects, we also invent a family of multiple-resampling (MR) single-user and multiuser receivers. With each resampling branch being tasked with the Doppler distortion of a particular path and/or user, these receivers are capable of significantly reducing the ICI levels, and thus offering superior error rate performance unprecedented by the traditional single-resampling (SR) designs. The performance advantage of the MR design is further enhanced by coupling the MR receiver front end with custom-designed data detection schemes and advanced sparse channel estimation algorithms. We demonstrate the effectiveness of the overall receiver design in practical UWA communication scenarios through real data-based emulations – using data from the KAM08 and the recent MACE10 experiment (Mobile Acoustic Communications Experiment 2010) – as well as through case studies using extensive simulations.

Furthermore, aiming at developping a robust and flexible multiple access scheme for UWA multiuser communications, we investigate the applicability of OFDMA for scenarios involving non-stationary users. We discover that for effective IUI management, the multiple resampling design is necessary, the result of which is a unified OFDMA

receiver design with IUI mitigation, channel estimation, and data detection and decoding of different user subcarrier assignment schemes under a common design framework. This enables us to easily compare different resource allocation strategies in terms of their ability to exploit the multipath diversity of the UWA channel. In particular, we find that the interleaved scheme, which spreads the user subcarriers across the entire band, may be beneficial when bandwidth allocated to each user is comparable to the coherence bandwidth of the UWA channel.

Finally, we investigate the difference between the single-resampling and the multiple-resampling receivers in terms of channel capacity with a discrete channel model based approach. Considering the equivalent linear systems resulting from different front end designs, the approach allows us to boil down the non-trivial channel capacity evaluation problem into a relatively simple problem, i.e., the capacity evaluation of fixed MIMO channels. We discover that the channel capacity achieved by the MR receiver is generally higher than that achieved by the SR receiver, provided that different signal arrivals have different Doppler scaling effects. Further, it appears that the MR design can exploit the Doppler rate difference as a performance benefit (to increase the channel capacity) while the SR receiver almost always suffers in terms of reduced capacity.

1.2   Organization of the Thesis

The thesis is organized as follows. Chapter 2 gives the background materials of multi-carrier communications over UWA channels, and provides a summary of existing works. In Chapters 3 and 4, we propose solutions to address the challenge of fast time variations posed by UWA-based multicarrier communications. Particularly, Chapter 3 focuses on inter-carrier interference mitigation for general time-varying UWA channels, while Chapter 4 is devoted to the advanced receiver designs for UWA channels with path/user-specific Doppler scaling factors. In Chapter 5, we present the designs for multiple-resampling OFDMA receivers and investigate the performance impact of different subcarrier assignment schemes. In Chapter 6, we derive discrete channel models for the single-resampling and the multiple resampling receivers, evaluate and compare the resulting channel capacities. Finally, Chapter 7 concludes the thesis.

4

Chapter 2

BACKGROUND AND PRELIMINARIES

In Chapter 1, we have given a general introduction of the thesis, summarizing the major existing works and pointing out the key contributions of the thesis. In this chapter, we will give a much detailed introduction to UWA communications, and use it as the background material for the rest of the thesis. To start with, we describe the history and background of UWA communications, commenting on the major challenges for communicating over UWA channels, leading to the introduction of OFDM as a bandwidth-efficient solution for multi-carrier communications. We then outline the challenges involved, such as peak-to-average power ratio (PAPR) control and timing and frequency synchronization, and focus on dealing with the inter-carrier interference (ICI) problem arising from the fast time variations of UWA channels. We introduce different strategies based on the nature of these time variations, and migrate to the discussion of multiuser systems that are tailored to UWA communications.

2.1 Underwater Acoustic Communications

Since the world's first underwater telephone was developed in 1945 [3], which enabled wireless communications among submarines, bandwidth-efficient and reliable underwater acoustic (UWA) communication systems have been widely studied. From simple analog systems with single-sideband (SSB) amplitude modulation in the early years, to modern digital systems employing advanced signal designs (coding and modulation schemes) and signal processing algorithms (adaptive equalization and diversity combining techniques), tremendous advances have been made in the world of wireless (tetherless) UWA communications [5, 20–22]. With the emergence of these new technologies, UWA communication systems are no longer restricted to be used solely for military purposes as it was in their early days; instead, their applications have been broadened to diverse commercial areas, such as remote control for off-shore oil industry, underwater monitoring of environmental systems, data collection in observatory science research, and so on [23, 24]. Recently, a new technical challenge for UWA communica-

tions has emerged with the objective of developing underwater networks that integrate instruments, sensors, robots, and vehicles in forming a "digital ocean" [14, 15]. For the dream of a fully-networked digital ocean to come true, in addition to developing network topologies and protocols suitable for the stochastic behavior of the underwater channels, reliable, high speed physical layer links among those instruments, vehicles, operators, platforms, and sensors of all types, are also highly demanded.

We point out that while other methods than acoustic waves can also be used for underwater communications, they have severe limitations. For instance, wired links are sometimes used for the control of underwater robots; however, the use of cables greatly limits the range of these links and reduces their flexibility. Radio waves have been widely used for communications over the air, but since water is a good conductor, electromagnetic waves are not suitable for underwater communications due to significant attenuation. The only other viable option seems to be the use of optical waves; however, they have major limitations as well [1, 15] (e.g. primarily due to strong scattering effects). In other words, acoustic waves represent the most promising means for tetherless (wireless) communications under water [3].

2.2   Characteristics of Underwater Acoustic Channels

While sharing similarities with terrestrial radio communications, UWA communications are much more challenging due to their unique characteristics. Specifically, dominant features of UWA links are extremely long multipath spreads, significant Doppler distortions, and range and frequency dependent signal attenuation [1]. The long delay spreads and strong Doppler effects are both due to the low speed of sound in water, i.e., about 1500m/s. For instance, a path length difference of only ten meters can result in a relative delay of 6.7 milliseconds. As a result, multipath spreads observed in typical mid-range UWA transmissions are usually in the order of tens or even hundreds of milliseconds (see Fig. 2.1 for an example), bringing about severe intersymbol interference (ISI) for single-carrier systems. With the speed of sound being low, we also have more noticeable Doppler effects, originating from relative motion between the transmitter and the receiver, and due to the variations in the medium. For instance, the involun-

tary drifting motion of underwater vehicles, with a speed of about 1.5 m/s, can cause the transmitted signal to be compressed or dilated by a factor of 10^{-3} (i.e., the ratio between the change in signal length and the original signal length in time), which is several orders of magnitude larger than what is commonly observed in terrestrial radio communications.

It is also worth mentioning that with path attenuation being scaled by a frequency-dependent absorption coefficient to the power of the communications range, the useful frequency band for UWA communications shrinks rapidly as the range and frequency increase as shown in Fig. 2.2. As such, UWA communications are commonly ultra-wideband in nature, i.e., characterized by a large bandwidth to carrier frequency ratio. It is because of this reason that for UWA communications, the Doppler induced frequency shifts are not uniform as it is the case for typical terrestrial radio communications.
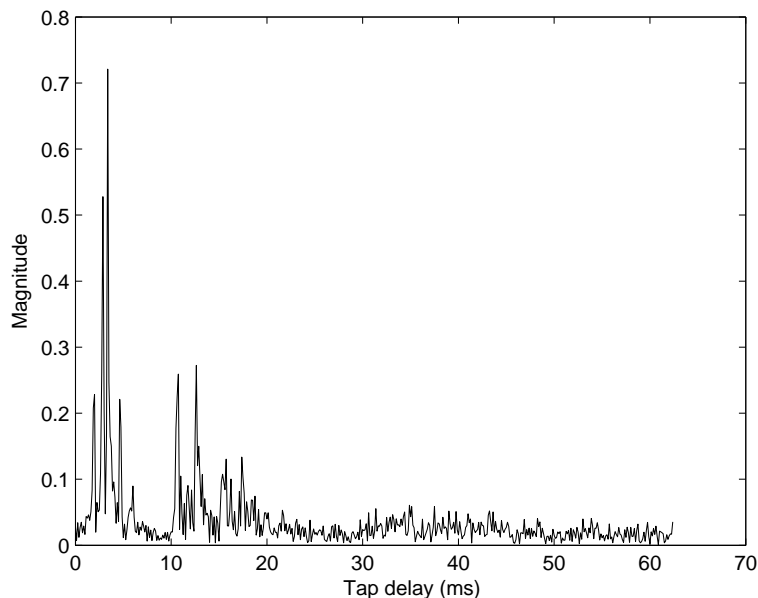
Figure 2.1: A typical UWA channel impulse response.

2.3 Multi-Carrier Communication over UWA Channels

Unique characteristics of UWA channels greatly impact the receiver designs. One important aspect is the choice of signaling strategies. For UWA communications, single-carrier signaling has been used for decades while the use of multi-carrier signaling has
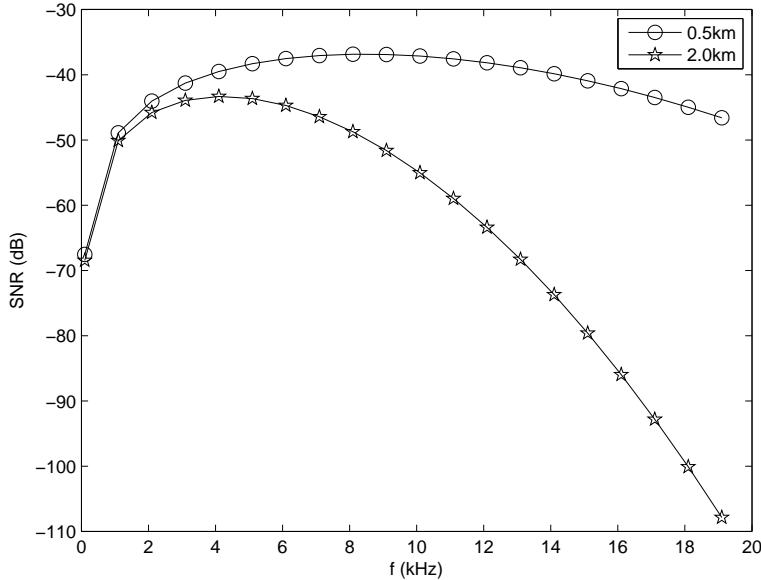
Figure 2.2: Range-dependent signal-to-noise ratio for UWA links as a function of frequency [1].

only emerged recently. For single-carrier systems, the entire frequency band is allocated to a single carrier, resulting in short symbol durations, which can be two to three orders of magnitude smaller than the multipath spreads [3]. This makes intersymbol interference (ISI) a significant challenge for single-carrier systems requiring complicated channel equalization schemes [3]. On the other hand, multi-carrier systems, which instead of using the full bandwidth for one channel, divide the bandwidth into many sub-channels in which different symbols are transmitted, are less affected by the long delay spreads. The reason is that with the bandwidth of the sub-channels becoming very small, each subchannel sees an approximately flat fading channel, and hence no ISI effects are observed.

Using frequency division multiplexing (FDM) may require relatively large sub-channel separations resulting in: (1) an inefficient use of bandwidth as part of the bandwidth is devoted as guard bands among different sub-channels, instead of transmitting useful signals; (2) a high demand for the hardware design, i.e., narrow-band analog filters need to be designed with very sharp cut-off frequencies to suppress the inter-channel interference. To overcome these problems, in the 1970s, orthogonal fre-

quency division multiplexing (OFDM) [25] was invented in Bell labs. For OFDM, the transmitted signal is given by

$$s(t) = \text{Re} \left\{ \sum_{k=0}^{N-1} d_k e^{j2\pi f_k t} R(t) \right\} \tag{2.1}$$

where k is the sub-carrier index, d_k is the constellation symbol modulated on the frequency $f_k = f_0 + k/T$ (where T is the OFDM block length and f_0 is the frequency of the lowest subcarrier), and $R(t)$ is the modulation pulse.

There are different implementations of OFDM, among which two most commonly used ones are the cyclic-prefixed (CP)-OFDM and the zero-padded (ZP)-OFDM. For the former, a cyclic prefix is attached to the beginning of an OFDM block, which is introduced to guard consecutive OFDM blocks to avoid inter-block interference (IBI). Note that the usage of cyclic prefix also turns the channel effect into circular convolution, which brings the ease of receiver-side processing [25]. For the ZP-OFDM, zeros are padded at the end of an OFDM block used as a guard period. Note that in this case, to make the channel effect a circular convolution, special receiver side processing is needed [25].

Passing $s(t)$ through a linear time-invariant multipath channel with additive white Gaussian noise (AWGN) results in a received signal given by

$$r(t) = \sum_{p=0}^{N_p-1} h_p s(t - \tau_p) + w(t), \tag{2.2}$$

where N_p is the number of propagation paths, h_p and τ_p are the path gain and path delay of the p-th path, and $w(t)$ is the additive Gaussian noise with power spectral density $\frac{N_0}{2}$. The OFDM scheme exploits frequency orthogonality among sub-channels to avoid both inefficient use of bandwidth and complexity in the hardware design. Here, the significantly improved spectral efficiency results from the fact that with the use of orthogonal center frequencies for the sub-channels, the resulting sub-bands, instead of being required to be well-separated, can be overlapping with each other. Note that the orthogonality of the sub-channels could be maintained at the receiver side regardless of the multipath spread, provided that the length of guard interval is not less than the multipath spread [25]. The reduced transceiver complexity is made possible because the

modulation and demodulation of OFDM signals can be effectively implemented using inverse fast Fourier Transform (FFT) and FFT, respectively. Further, as a result of the sub-channel orthogonality, single-tap frequency domain equalization can be applied for decoding the transmitted symbols [25].

2.4 Challenges for Multi-Carrier Systems Based on OFDM

General issues in OFDM include control of peak to average power ratio (PAPR), need for accurate time and frequency synchronization, and necessity of mitigation of Doppler-induced ICI when the channel is time-varying. Specifically, for UWA communications, the received signal is usually distorted by strong Doppler effects and fast channel variations. That is, for a time-varying channel, the received signal is given by

$$r(t) = \sum_{p=0}^{N_p-1} h_p(t) s\left(t - \tau_p(t)\right) + w(t), \tag{2.3}$$

where $h_p(t)$ and $\tau_p(t)$ are the time-varying tap gain and tap delay of the p-th path as detailed in [26]. The time variations in the channel destroy the orthogonality among the subcarriers, and hence ICI arises, rendering the ICI mitigation extremely important for UWA OFDM systems.

While time variations can in general take arbitrary forms, it was reported that in many cases they are caused by motion-induced Doppler scaling effects [9, 12], i.e.,

$$r(t) \approx \sum_{p=0}^{N_p-1} h_p s\left(t + a_p t - \tau_p\right) + w(t), \tag{2.4}$$

is a good model, where a_p, defined as $\frac{v_p}{c}$, is the Doppler scaling factor of the p-th path, and v_p and c are, respectively, the speed of transmitter-receiver motion along the p-th propagation path and the speed of sound in water. Note that while almost negligible in terrestrial radio transmissions, due to low propagation speed of sound, a_p is much more significant in UWA transmissions. For instance, a relative transmitter-receiver motion of 1.5 meters per second, which can be the consequence of an involuntary drift due to an underwater current, will result in a Doppler scaling factor of 0.001, which is extremely high and will make the signal undecodable if not compensated for.

Assuming that Doppler factors differ among different paths only by a very small amount (e.g., in the order of 10^{-4}), commonly-adopted methodologies for ICI mitigation usually involve two steps: the first step utilizes a preprocessing stage in the form of single-rate resampling, which aims to compensate for the common Doppler distortion experienced by all the propagation paths [12]; and the second step adopts different ICI-aware post data detection schemes to deal with the ICI caused by residual path-specific Doppler distortions [9] and/or random channel variations [26, 27].

A commonly-adopted approach to address the problem is to first estimate the ICI coefficients with a proper pilot assignment, and then mitigate the ICI exploiting the obtained ICI estimates [9, 13, 26, 28]. The ICI estimation phase is highly model dependent. For instance, in [26] it is assumed that the ICI is a consequence of tap coefficient variations which are different for different taps. Based on this assumption, a model that represents the tap-delay-dependent variations in the frequency domain is built, and therefore, the channel estimation problem boils down to the estimation of these frequency-domain tap coefficients, which resemble a scattering function. In [9], however, the ICI is assumed to be the result of a residual Doppler effect, and therefore, the ICI model takes the form of a sinc function whose influence attenuates inversely with increasing frequency separation. Different from [26] and [9], which base their derivations on exact underlying physical models, the algorithm in [13], is based upon the wide sense stationary uncorrelated scattering (WSSUS) assumption of the UWA channel and could potentially reduce the pilot overhead.

Most of the existing approaches for ICI mitigation obtain a frequency domain channel matrix which characterizes each individual subcarrier gain and the interference it casts over its neighbors. Based on the channel matrix, different ICI cancelation schemes can be applied. Among these, the most commonly-used are minimum mean square error (MMSE) type linear ICI cancelation [13], parallel interference cancellation (PIC) [28], and serial interference cancellation (SIC) [29]. It is worth mentioning that due to the large number of subcarriers, direct MMSE type linear cancelation is computationally complicated. Hence, to reduce the computational complexity, a technique

called Q-tap MMSE linear cancelation [13] may be utilized, acknowledging the fact that the channel matrix is quite sparse, with each subcarrier only affecting a limited number of its neighbors.

2.5 Receiver Design for OFDM over Doppler-Distorted Underwater Acoustic Channels

We now consider scenarios, where different signal arrivals are associated with significantly different Doppler scaling factors. For these scenarios, standard single-resampling designs, which count on resampling the received signal by a nominal Doppler scaling factor, might not be appropriate since significant path-specific Doppler distortions still remain in the resampled signal. In this case, most post data detection schemes are likely to fail or at least experience significant performance degradation due to strong ICI caused by the residual (path-specific) Doppler effects.

To address the challenges posed by the disparate Doppler scaling factors, Yerramalli and Mitra have recently proposed a remedy within the framework of the single-resampling designs [30]. Aiming at obtaining an accurate approximation to the sufficient statistics for data detection, the key idea of their approach is to optimize the resampling rate in such a way that the resultant equivalent discrete channel model has a Fisher information which is close to that associated with the channel model characterizing the sufficient statistics. To achieve this goal, the authors look at different optimization criteria: (1) minimization of Cramér-Rao Lower Bound (CRLB); (2) minimization of Hammersley-Chapman-Robbins Bound (HCRB). While conceptually appealing, due to the complexity of the cost function, the closed-form expression of the optimal resampling rate is intractable, and therefore, a brute-force approach is taken. To make this approach more practical, the authors summarize some empirical results based on their observation. Particularly, they point out that when the impulse response is dominated by one strong path, the resampling rate should be the Doppler scaling factor of this strong path, while when the paths have almost equal power, the resampling rate should be the average of their associated Doppler scaling factors.

2.6 Multi-User Communications over UWA Channels

With the rapidly growing interest in underwater sensor networks (USN) [14, 15], UWA multiuser communications have become an active research area in the past few years. To meet the demanding requirements for the USN applications (e.g., the support of potentially large number of nodes with very limited UWA bandwidth resources), different specially-tailored multiple access schemes have been proposed. For example, spread spectrum techniques in the form of direct sequence code-division-multiple-access (DS-CDMA) have been prototyped, acknowledging their capability to exploit multipath diversity through RAKE receivers [31]. The biggest challenge, however, is how effective power control can be managed with the large UWA channel latency. Besides CDMA systems, TDMA systems [18] – benefitting from their simplicity – have also been considered. These systems are particularly useful for delay insensitive applications, where the problem of large guard intervals (caused by UWA channel's long multipath delay spreads) can be circumvented. Recently, with their rapidly growing success in radio terrestrial communications [32, 33], OFDMA-based techniques have been proposed as a promising alternative to the other multiple access schemes [34]. The major advantages of OFDMA systems include robustness to large multipath delay spreads, high spectral efficiencies, and the ability to exploit the multiuser and/or multipath diversity through flexible user/carrier assignment. Currently, most works for OFDMA have been focused on power-saving scheduling methods as in [34, 35].

As in the case of radio communications, for UWA multiuser systems, user cooperation is possible by allowing different users (possibly operating on the same frequency band and at the same time) to coordinate with each other to bring significant multiplexing/diversity gains benefitting UWA communications systems, and therefore significantly improve utilization of the limited acoustic bandwidth [17]. To fulfill this goal, several underwater MIMO systems have been designed, some of which using OFDM [7, 8, 11], and others employing traditional single-carrier signaling [36]. While demonstrating improved spectral efficiencies, most of these MIMO systems use central-

ized transmitting/receiving elements, preventing them from enjoying the full spatial and multiuser diversity over UWA channels. As such, recently, there have been increasing interest in decentralized systems, where users/nodes are spatially separated. For instance, in [17] intermediate nodes located between source and destination are utilized as relays to offer extra diversity through distributed space-time block codes (DSTBC).

Alternatively, the overall multiuser system capacity can be increased through spatial multiplexing, where multiple users, simultaneously transmitting/receiving independent data streams on the same frequency band, are grouped together to form a multiuser MIMO system [37]. As an example, recently some progress have been made utilizing time reversal (TR) mirror theory with single-carrier signaling [38]. The fundamental idea is to use a large centralized TR array to achieve directional transmissions towards spatially separated users, where by combining a large number of transmit elements with the help of the time-reversed channel impulse response (CIR) of each transmitter-receiver pair, the equivalent channel model characterizing the receiver demodulation outputs is transformed into a channel that only suffers from very limited residual ISI and co-channel interference [16, 39]. The underlying assumption is that as compared to a rapidly time-varying CIR of each pair, the equivalent channel changes very slowly such that adaptive equalization schemes can be used to deal with the slowly-varying residual interference when a set of out-dated CIRs, estimated at the beginning of each transmission, are used at the transmit array for time-reversal processing.

2.7   Chapter Summary

In this chapter, we have reviewed basics of UWA communications and focused on bandwidth-efficient multi-carrier communications implementation via OFDM. While robust to multi-path, OFDM has a number of issues when used over time-varying channels. Particularly, for UWA channels, many challenges arise due to ICI problems caused by fast UWA channel variations. We have reviewed various ICI mitigation strategies, which usually include a single-rate resampling stage tasked with the compensation of nominal Doppler scaling effect, and a post ICI-aware data detection stage to mitigate the ICI due to uncompensated Doppler distortions/channel variations. Besides OFDM

receiver designs, we have also reviewed works on UWA multiuser systems, where the major focus is on different multiple access schemes and the system enhancement through multiuser cooperation.

Chapter 3

MITIGATION OF INTERCARRIER INTERFERENCE FOR OFDM OVER
TIME-VARYING UNDERWATER ACOUSTIC CHANNELS

Orthogonal frequency division multiplexing (OFDM) has emerged as a promising modulation scheme for underwater acoustic (UWA) communications, thanks to its robustness to channels with severe time dispersion. Compared to conventional single-carrier systems, for which complicated equalization schemes are usually required, OFDM systems are in general much simpler to implement as detection can be carried out symbol-by-symbol over time-dispersive channels.

In this chapter, we focus on cyclic-prefixed OFDM over time-varying UWA channels. To cope with the intercarrier interference (ICI) that arises at the receiver side because of the time variations in the channel, we consider two ICI-mitigation techniques [10, 40]. In the first scheme, the ICI coefficients are explicitly estimated, and minimum mean square error linear equalization based on such estimates is performed. In the second approach, no explicit ICI estimation is performed, and detection is based on an adaptive decision-feedback equalizer applied in the frequency domain across adjacent subcarriers. To cope with the phase variations of the ICI coefficients, phase-tracking loops are introduced in both ICI-mitigation schemes. The effectiveness of the presented schemes is demonstrated through simulation results, as well as real data collected in a recent experiment conducted in shallow water off the western coast of Kauai, Hawaii, in June 2008.

The rest of the chapter is organized as follows. Section 3.1 reviews some of the existing ICI mitigation techniques and outlines of the proposed methods. Section 3.2 introduces the system model for OFDM transmissions over time-varying UWA channels and describes the pre-detection synchronization stage. In Section 3.3, we discuss different detection schemes, with and without ICI mitigation. In Section 3.4, we present numerical results of the considered detection schemes for simulated channels as well as results obtained in the KAM08 experiment. Finally, Section 3.5 concludes the chapter.

3.1   Introduction

Underwater acoustic (UWA) channels are generally considered as one of the most challenging communication media, mainly because of their high time-frequency selectivity [1]. Compared to terrestrial radio channels, shallow-water UWA channels typically exhibit a much greater time dispersion, even on the order of hundreds of milliseconds [1]. In classical single-carrier communication systems, such multipath spreads cause severe intersymbol interference, which requires sophisticated and computationally-demanding equalization techniques. Transmission schemes based on orthogonal frequency division multiplexing (OFDM) have recently emerged as an attractive solution for UWA communications [5, 6, 12, 21, 41]. For example, promising results have been obtained in a recent UWA communication experiment, AUVfest07, performed in June 2007 off the coast of Panama City, where an OFDM-based scheme was able to provide reliable communications at horizontal distances up to 3500 m, with rates up to 50 kbps [6].

The key advantage provided by OFDM transmissions is that, for time-invariant channels, modulation symbols transmitted over different subcarriers do not interfere with each other even after propagating over frequency-selective channels, so that simple symbol-by-symbol detection can be adopted [41]. Unfortunately, this property no longer holds on time-varying channels, as intercarrier interference (ICI) arises [13, 26, 29, 42, 43]. In wireless radio communications, the time variations is typically very small with respect to the duration of the OFDM symbols; therefore, satisfactory detection performance can be achieved even if ICI is neglected. For example, the ICI due to the Doppler effect can safely be neglected in most wireless channels, since the relative speed between the transmitter and the receiver is usually several orders of magnitude lower than the speed of light (e.g., seven orders of magnitude for a relative speed of 100 km/h). On the contrary, the speed of sound in water is about 1.5 km/s, hence even relative speeds of a few meters per second may cause significant ICI.

Techniques for Doppler shift estimation and compensation can be found in [5,12], where it is also shown that in many cases no significant ICI is present after proper com-

pensation of the Doppler shift. Here, we focus on more challenging UWA environments, where the Doppler shift is not the only significant source of ICI. Most of the existing ICI-mitigation schemes are based on a two-step approach: first, an estimate of the ICI coefficients is obtained; then a suitable ICI-mitigation technique exploiting such estimates is employed. For these approaches, the most critical part appears to be estimation of the ICI coefficients, which generally exploits pilot symbols in the transmitted sequence [13, 26, 42, 44]. Several ICI-mitigation schemes exploiting the basis expansion model (BEM) [45] have been proposed [27, 43, 46–49]. However, it was shown in [50] that many cases exist where ICI mitigation based on the blind decomposition of the channel variations through the BEM is outperformed even by the standard ICI-neglecting receivers. A promising alternative consists of explicitly modeling the channel variations and exploiting the model in the receiver design (for example, see [51]). Some algorithms, such as the one presented in [13], rely on the wide sense stationary uncorrelated scattering (WSSUS) assumption for the channel model, which may be acceptable for most wireless radio channels, but is unlikely to be satisfied in UWA channels [1]. Some algorithms, such as the one presented in [9], rely on pilot symbols with a very particular structure. In all these cases, the frequency-domain equalization performed by the ICI-mitigation techniques is computationally much simpler than the time-domain equalization that would be required for single-carrier communications over the same channel [13, 26, 29, 42, 43].

In this chapter, we consider two ICI-mitigation techniques that do not rely on any particular assumption on the channel statistics, nor on the structure of the pilot symbols. In the first scheme, the ICI coefficients are estimated by means of a closed-loop tracking system, based on which minimum mean square error (MMSE) linear equalization [4] is performed in the frequency domain. In the second scheme, no explicit ICI estimation is performed, and detection is made by means of an adaptive decision-feedback equalizer (DFE) [4] in the frequency domain. To cope with the phase variations of the ICI coefficients, phase-tracking schemes are introduced in both cases. We present simulation results showing that the considered schemes can provide significant performance improvements with respect to the standard receivers that neglect
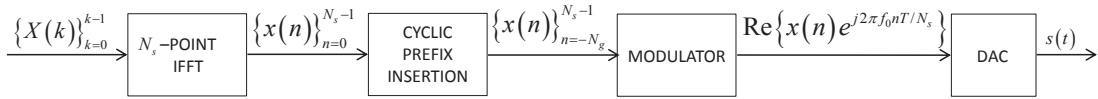
Figure 3.1: Block diagram of a CP-OFDM transmitter.

the ICI. We also discuss decoding of UWA-communication data recorded in the Kauai Acomms MURI 2008 (KAM08) experiment [2], which was conducted in shallow water off the western coast of Kauai, Hawaii, in June 2008. Particularly, we present results for a 4-km link with no motion between the transmitter and the receiver, and a 2-km link in which the transmitting transducer was towed at a speed of 3 knots.

3.2 System Model

An OFDM system with K subcarriers is considered, where K is an integer power of two. An OFDM frame consists of K symbols $\{X(k)\}_{k=0}^{K-1}$, obtained by mapping a sequence of (possibly channel-coded and interleaved) bits into a suitable complex-valued constellation, such as phase-shift keying (PSK) or quadrature amplitude modulation (QAM). A subset of the K symbols are typically used as pilot symbols, to be exploited for channel estimation at the receiver side. The continuous-time OFDM waveform $s(t)$ is obtained by modulating the symbols $\{X(k)\}_{k=0}^{K-1}$ over a set of orthogonal subcarriers, as follows

$$s(t) = \mathrm{Re}\left\{\sum_{k=0}^{K-1} X(k)e^{j2\pi f_k t}\right\}, \quad t \in \{-T_g, T\}, \tag{3.1}$$

where $f_k = f_0 + k/T$ is the frequency of the k-th subcarrier, $1/T$ is the spacing between consecutive subcarriers, and $T_g < T$ is the duration of the cyclic prefix [41]. The structure of an OFDM transmitter is illustrated in Fig. 3.1. An efficient all-digital OFDM implementation is obtained by means of the inverse fast Fourier transform (IFFT) [41]. Let $\{x(n)\}_{n=0}^{N_s-1}$ be the sequence obtained by taking the N_s-point IFFT of the symbols $\{X(k)\}_{k=0}^{K-1}$, as follows

$$x(n) = \sum_{k=0}^{K-1} X(k)\exp\left\{j2\pi\frac{kn}{N_s}\right\}, \quad n \in \{0, 1, \ldots, N_s - 1\}, \tag{3.2}$$

where $N_s \geq K$. A cyclic prefix is inserted between consecutive OFDM frames to prevent interframe interference at the receiver side [41]. Appending the last $N_g =$

19

$N_s T_g/T$ samples of the sequence $\{x(n)\}_{n=0}^{N_s-1}$ at the beginning of the sequence itself [41], we obtain the complete CP-OFDM word $\{x(n)\}_{n=-N_g}^{N_s-1}$. As shown in Fig. 3.1, the lowpass signal is then modulated onto the desired carrier frequency f_0, and the waveform $s(t)$ that finally feeds the acoustic transducer is generated by means of a digital-to-analog converter (DAC).

The block diagram of the considered receiver is depicted in Fig. 3.2. The very first block is an analog-to-digital converter (ADC), which, after proper anti-aliasing filtering, samples the continuous-time signal with period $T_s = T/N_s$, producing the sequence $u(n)$. In the following, we briefly review the blocks that precedes the detection block, which is the main target of our work and is discussed in Section 3.3.

The first impairment that the considered receiver tries to mitigate is the Doppler effect due to the relative speed between the transmitter and the receiver, which is quantified by the Doppler rate a, i.e., the ratio between that speed and the speed of sound in water. We will consider wideband UWA signals, for which the Doppler effect causes, besides a frequency shift, a significant frequency spread [12]. Once a coarse estimate $\widehat{a}$ of the Doppler rate a is obtained, the received signal is resampled with period $T_s/(1 + \widehat{a})$, producing the sequence $v(n)$ — see [12] for details on this stage. We point out that the described strategy, though based on the assumption that all propagation paths are characterized by the same time-invariant Doppler rate, is still useful when this assumption does not hold completely, since all path-dependent mismatches with respect to the estimated Doppler rate can be considered as residual impairments to be handled in the detection stage. This point will be studied in detail for the case of the data collected in the KAM08 experiment.

After the resampling stage, the receiver works in the complex-envelope domain, defined with respect to the frequency f_0. We will denote by $z(n)$ the complex-envelope sequence corresponding to the real-valued sequence $v(n)$. The next processing stage at the receiver side is aimed at achieving time synchronization, that is, at finding which samples in $z(n)$ correspond to the transmitted sequence $x(n)$. Also, frequency synchronization is to be achieved, because of possible clock frequency errors/jitters, and
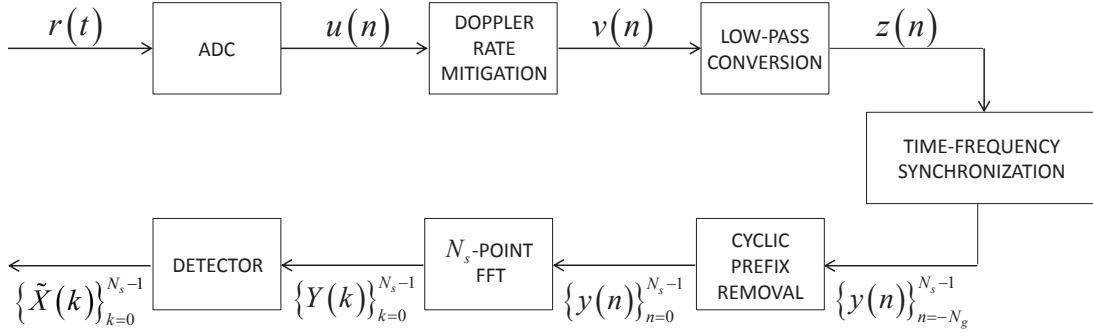
Figure 3.2: Block diagram of the considered receiver.

possible uncompensated Doppler shifts. For instance, an estimation error in the Doppler rate on the order of 10^{-4}, which is typical in most scenarios [12], produces a frequency offset of 1.6 Hz for a subcarrier centered at 16 kHz, which is significant for OFDM with subcarrier separation of a few Hz, as in the KAM08 experiment, and should thus be compensated. We adopt the joint time-frequency synchronization scheme proposed in [52], which exploits the presence of a cyclic prefix and, yet originally designed for frequency-flat channels, is known to be very effective also over channels with multipath propagation.

The sequence $\{y(n)\}_{n=-N_g}^{N_s-1}$ at the output of the time-frequency synchronization block contains samples related to both the cyclic prefix and the actual OFDM data. At this stage, the samples corresponding to the cyclic prefix are no longer useful and can be discarded. A very general discrete-time channel model is given by

$$y(n) = \sum_{\ell=0}^{L} c(n;\ell)x(n-\ell) + \eta(n) \ , \tag{3.3}$$

where $c(n;\ell)$ is the time-varying channel impulse response (CIR) and $\eta(n)$ is additive white Gaussian noise (AWGN). The considered model defines the class of all linear, causal, time-varying channels of delay order L, observed in AWGN. Note that $c(n;\ell)$ describes the explicit time variations in the CIR, but also includes the uncompensated synchronization parameters. The samples $\{y(n)\}_{n=0}^{N_s-1}$ are processed by a fast Fourier transform (FFT)-based demodulator [41], which generates the samples

$$Y(k) = \frac{1}{N_s} \sum_{n=0}^{N_s-1} y(n) \exp\left\{-j2\pi \frac{nk}{N_s}\right\} \ .$$

21

The relevant channel model can be written as

$$Y(k) = \sum_{m=0}^{K-1} C(k;m)X(m) + N(k) , \qquad (3.4)$$

which is of interest for $k \in \{0, 1, \dots, K-1\}$, that is, only for subcarrier indices at which symbols were actually transmitted. In (3.4), $N(k)$ is AWGN and

$$C(k;m) = \frac{1}{N_s} \sum_{n=0}^{N_s-1} \sum_{\ell=0}^{L} c(n;\ell) \exp\left\{j2\pi \frac{n(m-k)-ml}{N_s}\right\} . \qquad (3.5)$$

The reported formulations are correct under the assumption that the duration of the cyclic prefix is at least equal to that of the CIR, that is, $N_g \geq L$. In the case of time-invariant channels, that is, when $c(n;\ell)$ does not depend on the time index n, the coefficients $C(k;m)$ are non-zero only for $k = m$, so that the model (3.4) simplifies to

$$Y(k) = C(k;k)X(k) + N(k) . \qquad (3.6)$$

In practice, provided that the cyclic prefix is long enough, the orthogonality of the subcarriers is maintained even after propagation over a time-dispersive channel, which is the key motivation for the success of OFDM systems [41]. In this chapter, we address a more general scenario in which ICI arises due to significant time variations in the channel. The correct channel model is then given by (3.4). Comparing (3.4) and (3.6), we see that the coefficient $C(k;m)$ describes the ICI due to the m-th subcarrier on the k-th subcarrier. In the following, we will often refer to the ICI coefficients using the notation "ICI coefficient with index i", where i is the difference between the indices of the interfering subcarriers. For example, the ICI coefficient with index 1 (-1) describes the ICI due to the closest higher (lower) subcarrier.

3.3   Channel Estimation and Data Detection

In this section, different approaches for channel estimation and data detection are described. All of them operate on the samples at the output of the FFT-based demodulator, which are described by the model (3.4).

3.3.1 Standard Receiver Neglecting ICI

The standard approach for OFDM detection consists of neglecting the ICI and assuming the model (3.6) instead of the model (3.4). This assumption reduces the channel estimation to the evaluation of the K complex-valued coefficients $C(k;k)$. Typically, a subset of the subcarriers is reserved for pilot symbols, which are used at the receiver side for channel estimation. Although the optimal placement of the pilot symbols depends on the frequency characteristics of the channel, for simplicity the pilots are usually equally spaced. A simple interpolation-based estimation method is reviewed in the following (see [12, 53, 54] for more advanced methods). For all values of k such that $X(k)$ is a pilot symbol, the coefficient $C(k;k)$ is estimated as $\hat{C}(k;k) = Y(k)/X(k)$. Then, the remaining coefficients $\hat{C}(k;k)$ are evaluated by linear interpolation — more advanced interpolation techniques are discussed in [53, 54]. Finally, the obtained estimates are assumed to be correct and standard coherent detection of the information symbols is carried out.

3.3.2 ICI-Mitigation Schemes

In this section, we review the state-of-the-art solutions for ICI mitigation and motivate our choice of focusing in the rest of the chapter on two specific algorithms, which are presented in the next two sections.

To mitigate Doppler-induced ICI, most recent works exploit the BEM [27,47–49]. With this model, possibly in conjunction with pulse shaping and receiver windowing [55], a sparse band representation of the frequency-domain channel matrix can be achieved. Therefore, block equalization algorithms such as those presented in [47–49] can be implemented with relatively low complexity. The most critical point in such approaches is the estimation of the BEM parameters [44]. Some recent works have shown that significant improvements can be achieved by applying the turbo principle, i.e., by iteratively improving the quality of the channel estimate based on the preliminary (soft) decisions made by the decoder [46].

When the channel spread is on the order of tens of milliseconds or more, a major drawback of most BEM-based approaches is that they do not exploit the time-domain sparseness of the UWA channel [1], thus requiring the estimation of a huge set of BEM coefficients [44]. Consequently, the ICI-mitigation ability is greatly compromised by the estimation errors, to the point that the BEM-based approaches may be even inferior to the ICI-neglecting receivers, as shown in [50]. A significant exception is given by the approach presented in [27], where by tracking the active taps of the channel impulse response the number of BEM parameters to estimate is significantly reduced. However, the underlying assumptions on the WSSUS nature of the channel and on the uniform power delay multipath profile are likely to be violated in many practical UWA scenarios. Additionally, the BEM-based approaches typically do not account for the wide-band nature of the UWA signals. Hence, a significant model mismatch arises even in the presence of a common phenomenon like the Doppler-induced time variations, which causes a frequency spreading that cannot be described by narrowband models.

Alternative ICI-mitigation approaches can be found in [9,50,51], where a specific source of ICI is addressed, i.e., the path-dependent Doppler rate. Yet very effective in such scenarios, these solution cannot be adopted when the main source of ICI has a different form.

In the following, we consider two ICI-mitigation techniques that do not rely on any particular assumption on the channel statistics, nor on the nature of the main source of ICI. The two approaches are based on the application in the frequency domain of MMSE linear equalization and DFE [4], respectively. As discussed in the next sections, we enhance these standard equalization techniques by introducing a phase-tracking loop that can cope with the linear phase variations characterizing the ICI coefficients.

3.3.3 First Approach to ICI Mitigation

A natural extension of the approximation in (3.6) consists of including in the channel model the ICI due to the two closest subcarriers, as follows [43, 55, 56]

$$Y(k) = \sum_{m=-1}^{1} C(k; k+m)X(k+m) + N(k) . \qquad (3.7)$$

The assumption motivating the approximation of (3.4) by (3.7) is that the ICI between two subcarriers becomes weaker as their separation increases. Note that the number of channel coefficients to be estimated is now $3K$, instead of K as in the standard approach described earlier. Although the indices in (3.7) are over frequency rather than over time, the model is formally identical to the well-known problem of single-carrier transmissions affected by time-varying intersymbol interference [4]. In such scenarios, an effective way to estimate the channel coefficients is given by closed-loop tracking based on the gradient algorithm (see [57] and references therein). In our case, the application of the gradient algorithm leads to the closed-loop estimation system described in the following. Let $\hat{C}(k; k+m)$ be the estimate of $C(k; k+m)$, for $m \in \{0, \pm 1\}$, and let us define the "error term"

$$\hat{E}(k) = Y(k) - \sum_{m=-1}^{1} \hat{C}(k, k+m)X(k+m) ,$$

where, as a first step, we assume that all symbols $X(k)$ are known. The channel coefficients at the subcarrier index $k+1$ are estimated as:[1]

$$\hat{C}(k+1; k+1) = \hat{C}(k; k) + \gamma_0 \hat{E}(k)X(k)^*, \qquad (3.8)$$

$$\hat{C}(k+1; k) = \hat{C}(k; k-1) + \gamma_{-1} \hat{E}(k)X(k-1)^*, \qquad (3.9)$$

$$\hat{C}(k+1; k+2) = \hat{C}(k; k+1) + \gamma_1 \hat{E}(k)X(k+1)^*, \qquad (3.10)$$

where γ_0, γ_{-1}, and γ_1 are the step sizes of the closed-loop update rules, to be numerically optimized [57]. Whenever time synchronization is not perfect, the channel coefficients are affected by a phase offset that increases linearly with the index k [52]. It is then

---

[1]The reported equations hold for PSK modulation alphabets. The formulations are more complicated for alphabets including symbols with different magnitude.

appropriate to account for such linear phase variations through the gradient algorithm. In this case, as shown in [57], the only modification to the estimation system is that the first-order loops (3.8), (3.9), and (3.10) become second-order loops [57].

The condition that all symbols $X(k)$ are known pilots is clearly not of interest for communication systems. Several approaches to manage unknown symbols in closed-loop estimation systems are discussed in [57]. Here, we adopt the decision-directed mode, driven by preliminary decisions made according to the approach described in Section 3.3.1. Finally, after estimation of the channel coefficients, the estimates are assumed to be correct and standard MMSE linear equalization (LE) is performed, as in [42]. Note that it is possible to apply the same principle iteratively, feeding the channel estimation loops with improved preliminary decisions at each iteration. This option has been studied in [46] for a different equalizer, where the benefits of iterating with an outer decoder were also investigated. With the understanding that the iterative approach can be exploited in the considered equalizer as well, for simplicity, in the following we will focus on the single-iteration case, which is adopted unless otherwise specified. The approach described in this section will be briefly referred to as frequency-domain (FD) LE (FD-LE).

3.3.4   Second Approach to ICI Mitigation

Let us now consider an ICI-mitigation scheme that, unlike the previous one, does not rely on an explicit estimation of the ICI coefficients. The idea is to exploit the equivalence between the model (3.4) and the channel model for single-carrier transmissions impaired by intersymbol interference, and extend adaptive-equalization concepts developed for such scenarios to our system. Particularly, we will consider the decision-feedback equalization (DFE) technique [4], introducing an additional second-order phase tracker able to cope with the already-mentioned phase offset due to imperfect time synchronization. This structure, which will be briefly referred to as frequency-domain DFE (FD-DFE), is the frequency-domain counterpart of the time-domain approach described in [20]. We point out that no assumption on the number of significant ICI coefficients is required, unlike in (3.7), since the coefficients are not explicitly estimated.

26
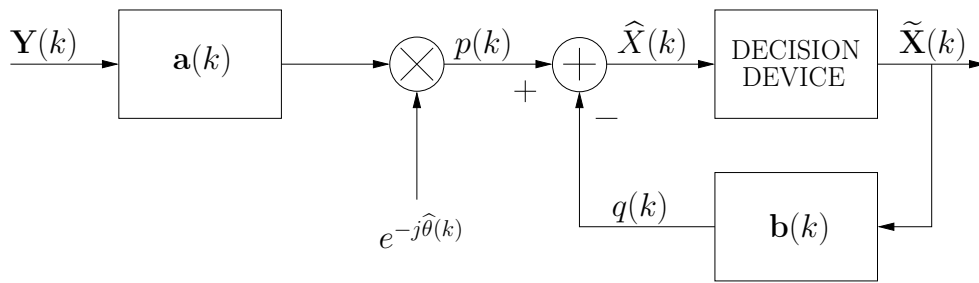
Figure 3.3: Block diagram of the FD-DFE with explicit phase compensation.

Fig. 3.3 shows a conceptual diagram of the equalizer. Denoting by k the index of the subcarrier, the feed-forward filter $\mathbf{a}(k)$ processes the samples $\mathbf{Y}(k)$, combining them and derotating the filter output, yielding to $p(k) = \mathbf{a}'(k)\mathbf{Y}(k)e^{-j\widehat{\theta}(k)}$.[2] In parallel, the feedback filter $\mathbf{b}(k)$ exploits the previously-made decisions $\widetilde{\mathbf{X}}(k)$ to compute $q(k) = \mathbf{b}'(k)\widetilde{\mathbf{X}}(k)$, producing the term $\widehat{X}(k) = p(k) - q(k)$ as an estimate of transmitted symbol $X(k)$. An error signal $e(k)$ is then computed as the difference between the estimate $\widehat{X}(k)$ and the desired symbol value $d(k)$, which could either be the transmitted symbol $X(k)$ for those subcarriers reserved as pilots, or the preliminary decisions $\widetilde{X}(k)$ for the remaining subcarriers. An optimization procedure is hence jointly run over the equalizer parameters $\{\mathbf{a}(k), \mathbf{b}(k), \widehat{\theta}(k)\}$, such that the mean squared error (MSE) $E[|e(k)|^2]$ is minimized, which requires the solution of the well-known Wiener filtering problem. To solve it, we adopt the recursive least square (RLS) procedure commonly used in the literature (see [4]).

In a similar way, we can pursue the MSE solution for the subcarrier phase offset $\widehat{\theta}(k)$. The recursion describing $\widehat{\theta}(k)$, according to a second-order gradient algorithm [57], can be written as

$$\widehat{\theta}(k+1) = \widehat{\theta}(k) + G_1\Phi(k) + G_2\sum_{i=0}^{k}\Phi(i) , \qquad (3.11)$$

where G_1 and G_2 are the step sizes of the loop, to be numerically optimized, and the gradient estimate $\Phi(i)$ is computed as

$$\Phi(i) = \mathrm{Im}\{p(i)(p(i) + e(i))^*\} = \mathrm{Im}\{p(i)e(i)^*\} . \qquad (3.12)$$

---

[2]Column vectors are written in lower-case bold fonts, and the symbol $(\cdot)'$ denotes conjugate transpose.

27

As for the FD-LE, the FD-DFE is initialized with preliminary decisions made according to the approach described in Section 3.3.1 and only one iteration of the equalizer is executed unless otherwise specified (see the discussion at the end of Section 3.3.3).

3.4 Numerical Results

To verify the effectiveness of the considered schemes, we present numerical results for simulated channels as well as for real data from the KAM08 experiment. Particularly, for the KAM08 experiment, both fixed- and towed-source scenarios are considered, the receiver being fixed in both cases.

3.4.1 Results for Simulated Channels

Our first goal is to obtain insights, through computer simulations, on the performance of different detection schemes when fast channel variations occur. The channel is simulated according to the model (3.3), with $L = 10$. The channel coefficients are obtained by independently generating each of the $L + 1$ taps according to an exponential power delay profile [58], the last tap having, on average, half the power of the first tap. Time variations are then obtained by perturbing the resulting coefficients by means of a zero-mean Gaussian random walk with tunable variance. We consider two channels, named channel A and channel B, which differ in the variance of the random walk. Namely, the ratio between the variance of the random walk and the expected power of the first tap is 10^{-4} for channel A and $2 \cdot 10^{-4}$ for channel B, so that the variations in channel B are faster. We remark that the simulated model, which is clearly not appropriate for most UWA channels, is used only with the aim of obtaining insights on how ICI affects the system performance. The importance of such insights will be clear when the actual experimental results are discussed, later in this section.

We consider an OFDM system with uncoded BPSK transmissions, first assuming that the receiver is perfectly synchronized in time, frequency, and Doppler rate. In this ideal scenario, perfect channel-state information (CSI) is also available and, for the FD-DFE, the preliminary decisions fed back are correct. Fig. 3.4 and Fig. 3.5 compare the performance of the considered detection schemes in terms of bit-error rate (BER)
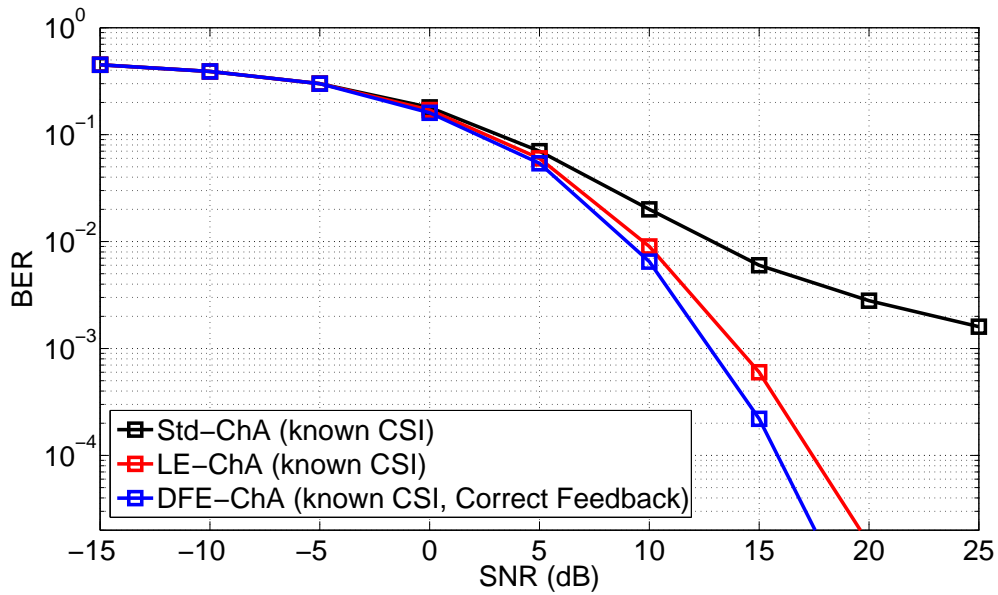
Figure 3.4: Performance comparison between a receiver that neglects the ICI and the considered ICI-mitigation techniques for the time-varying channel A.
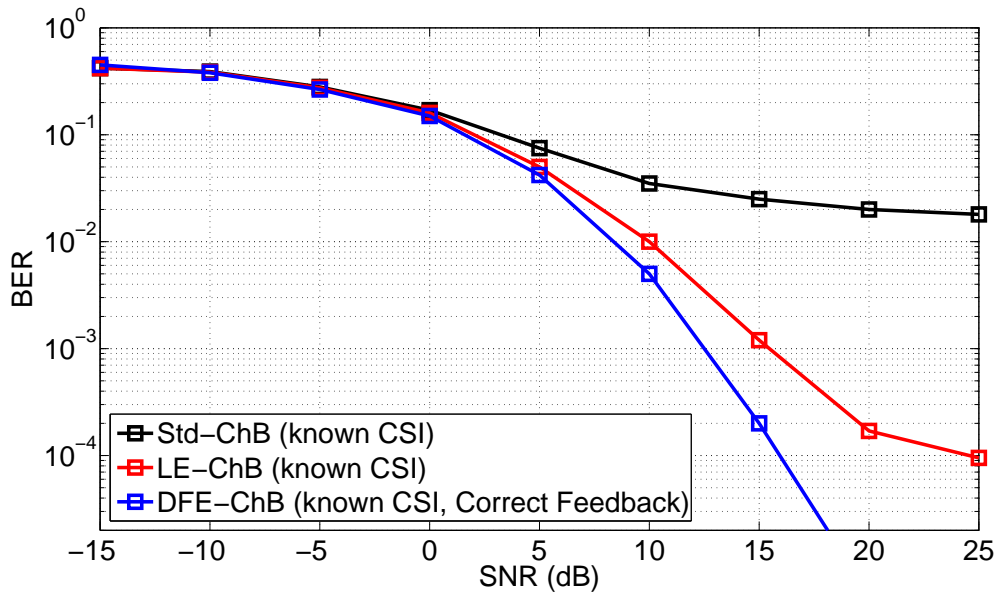
Figure 3.5: Performance comparison between a receiver that neglects the ICI and the considered ICI-mitigation techniques for the time-varying channel B.

versus signal-to-noise ratio (SNR), for the case $K = 2048$, $N_s = 12800$, and $N_g = 1000$. Considering (3.3), we define the SNR as

$$\text{SNR} = \frac{E\left[|x(n)|^2\right]}{E\left[|\eta(n)|^2\right]} \sum_{\ell=0}^{L} E\left[|c(n;\ell)|^2\right] ,$$

where $E[\cdot]$ denotes statistical expectation. Note that, in both simulated scenarios, BER floors are unavoidable when ICI is neglected, while they can be effectively mitigated when ICI-mitigation techniques are adopted. We also notice that, while both techniques are effective, the FD-DFE outperforms the FD-LE in both channels, the improvement becoming more noticeable as the time variations increase. Note that, at low values of the SNR, the performance of the classical approach is basically the same as that of the receivers with ICI mitigation. Hence, the simulations suggest that, given the statistics of the channel variations, two different regimes can be distinguished based on the SNR. In the former regime, which will be referred to as noise-limited, the ICI power is much lower than the noise power, so that no significant performance improvement can be achieved by ICI mitigation; in the latter, which will be referred to as ICI-limited, the ICI power is on the order of (or greater than) the noise power, so that the detection performance is remarkably improved by ICI mitigation.

We now investigate the performance of the same system when the assumptions of ideal CSI and error-free preliminary decisions are removed, and the detection algorithms work in the adaptive mode described in Section 3.3 exploiting the pilot symbols placed every four tones. Also, aimed at verifying the robustness of the considered approaches to synchronization errors, we assume that an error of 90 samples affects the detection of the start-of-CP sample — note that the error corresponds to less than 1% of the CP duration. As discussed in Section 3.3, the timing error causes a linear phase rotation of the frequency-domain channel coefficients, which motivated our choice of adopting a phase tracking loop in the ICI-mitigation receivers. The need for this solution is proved by the simulation results reported in Fig. 3.6 and Fig. 3.7, which both refer to channel A. Interestingly, while the FD-DFE exhibits a huge performance degradation in the absence of the phase-locked loop (PLL), the FD-LE is fairly robust to phase rotations even if a first-order gradient algorithm (GA) is adopted. This is due to the fact that

30
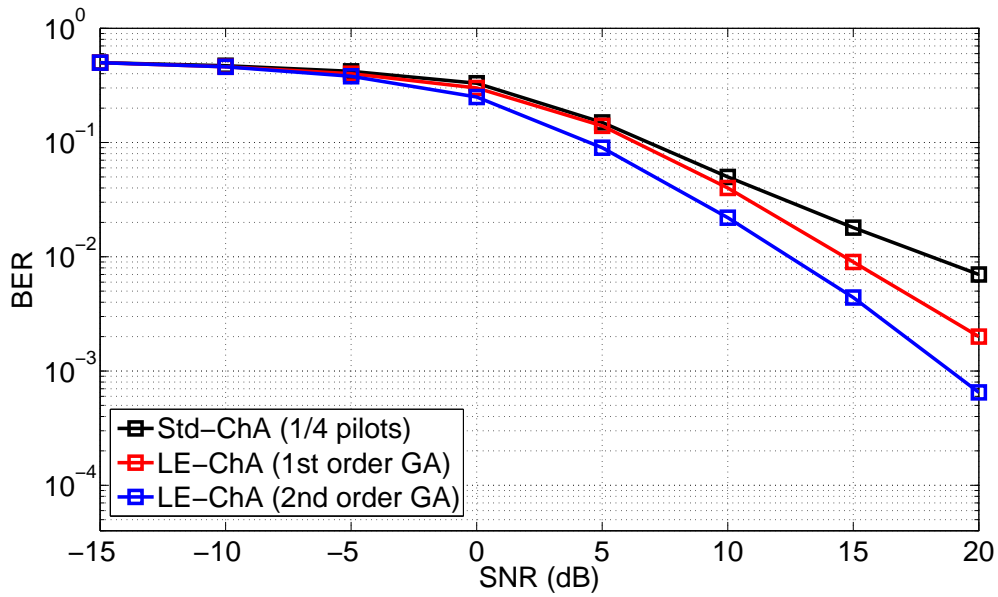
Figure 3.6: Performance of FD-LE with and without the PLL in the presence of a timing offset.
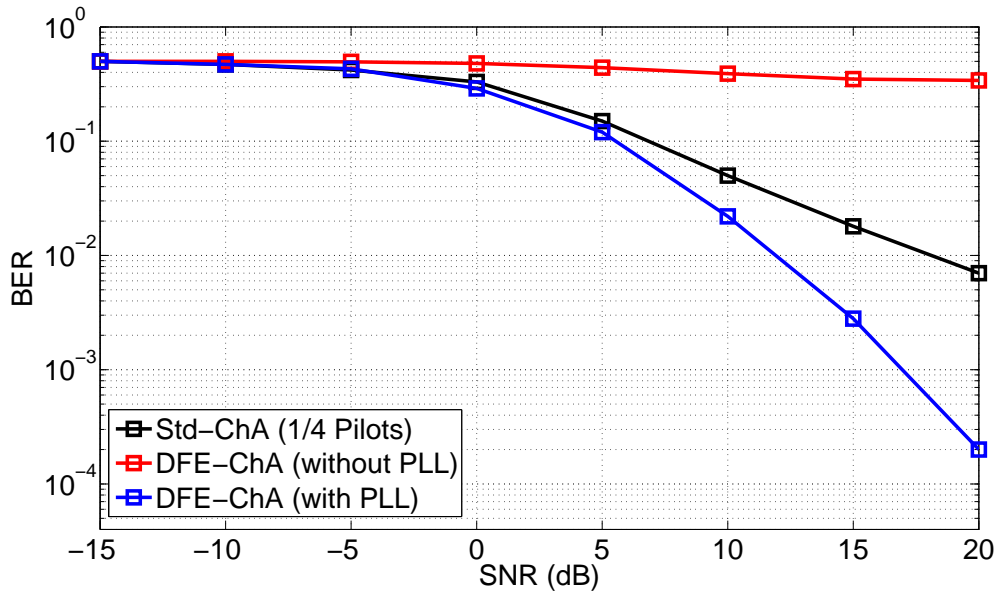
Figure 3.7: Performance of FD-DFE with and without the PLL in the presence of a timing offset.
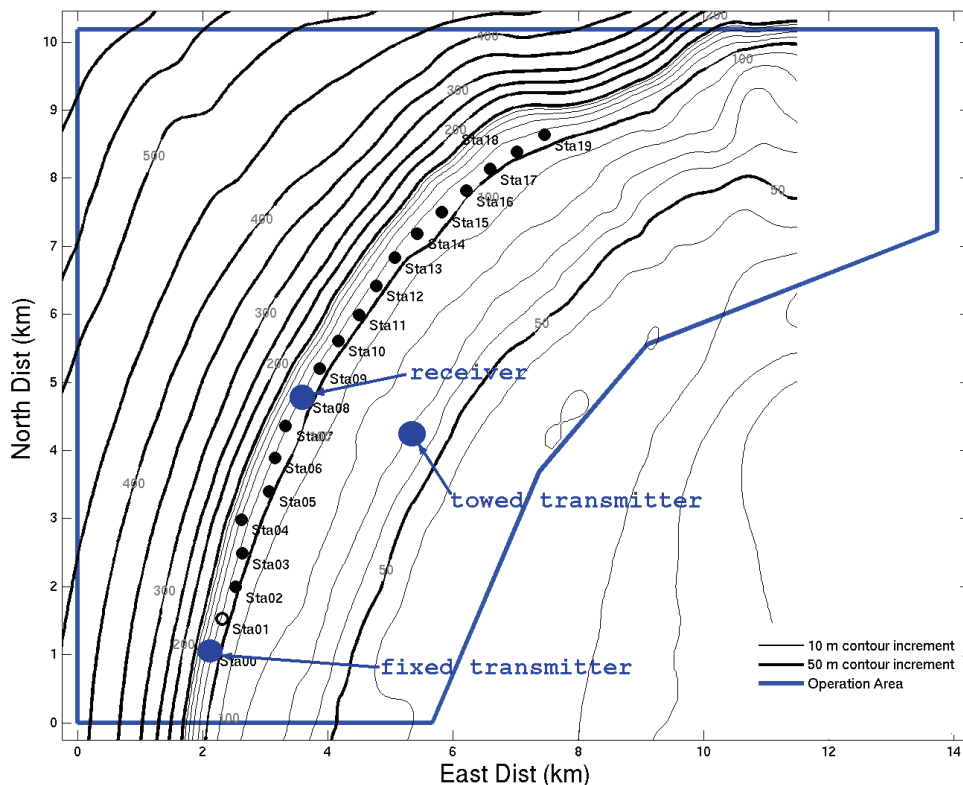
Figure 3.8: Bathymetry of the operation area of the KAM08 experiment, with depth in meters (taken from [2]).

the FD-DFE, utilizing a RLS-based algorithm, is effective only when the channel to equalize is stationary [4]. This condition clearly does not hold in presence of carrier phase rotations. On the contrary, for the FD-LE, there is no such strict constraint imposed, and therefore the absence of the second-order GA only results in a gradient estimate offset, proportional to the amount of phase rotations [57]. In our example, this offset is relatively small with respect to the actual value of the gradient.

3.4.2 Results for the KAM08 Experiment — Fixed-Source Scenario

Our experimental data were collected during the KAM08 experiment [2], which was conducted in shallow water off the western coast of Kauai, Hawaii, in June 2008. The bathymetry of the operation area is shown in Fig. 3.8. We present results for a fixed-source scenario and for a towed-source scenario (the relevant details are given later). The positions of the adopted transmitters and receivers are shown in Fig. 3.8.
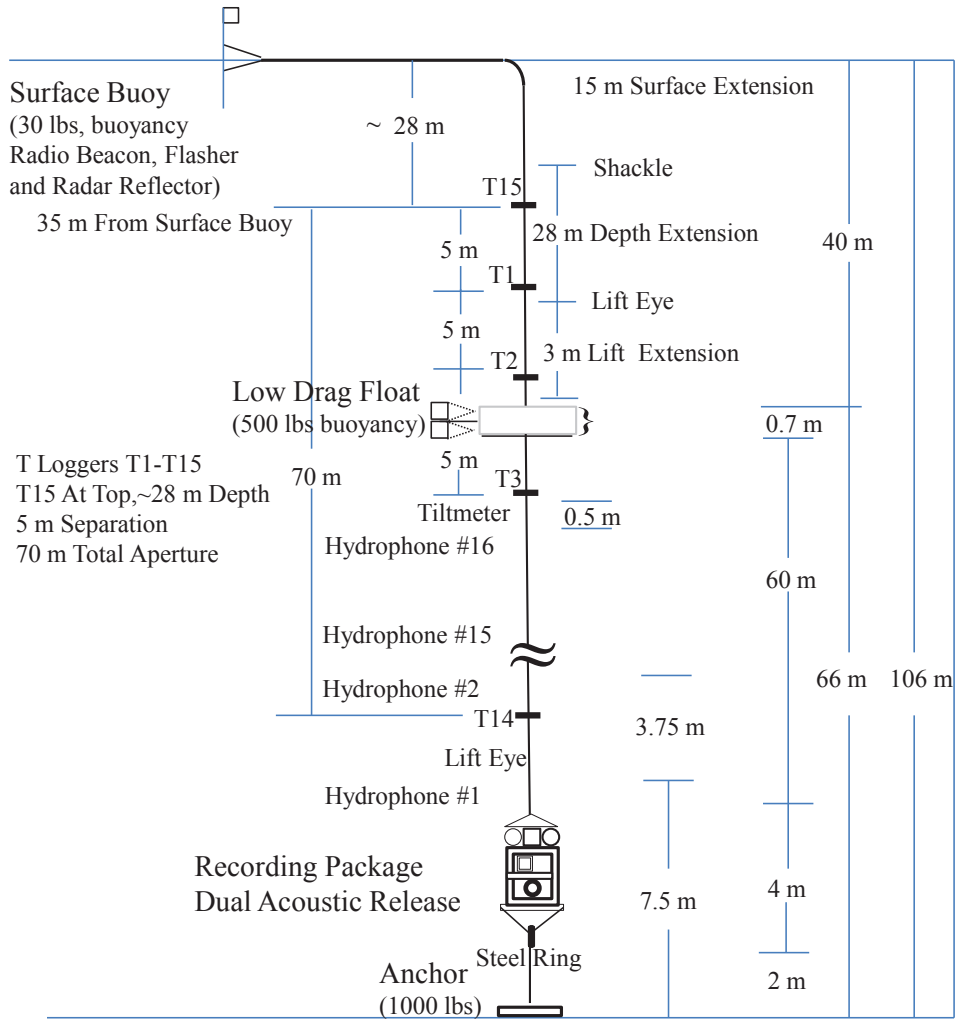
Figure 3.9: Scheme of the vertical-array transmitter adopted in the KAM08 experiment (taken from [2]).

Let us start from the fixed-source scenario, where no intentional motion between the transmitter and the receiver is present, and the resampling stage can thus be avoided. An 8-element vertical-array source was deployed with an inter-element separation of 7.5 m and an aperture of 52.5 m. The top element was at a nominal depth of 30 m, and the bottom element was not anchored to the sea floor. As receiver, a 16-element vertical array was deployed, at a distance of 4 km from the source. The sampling rate was 50 kHz. The inter-element spacing was 3.75 m, with the top element deployed at a nominal depth of 42.25 m. The pictorial descriptions of the adopted vertical transmitter array and the receiver array are given in Figs. 3.9 and 3.10.
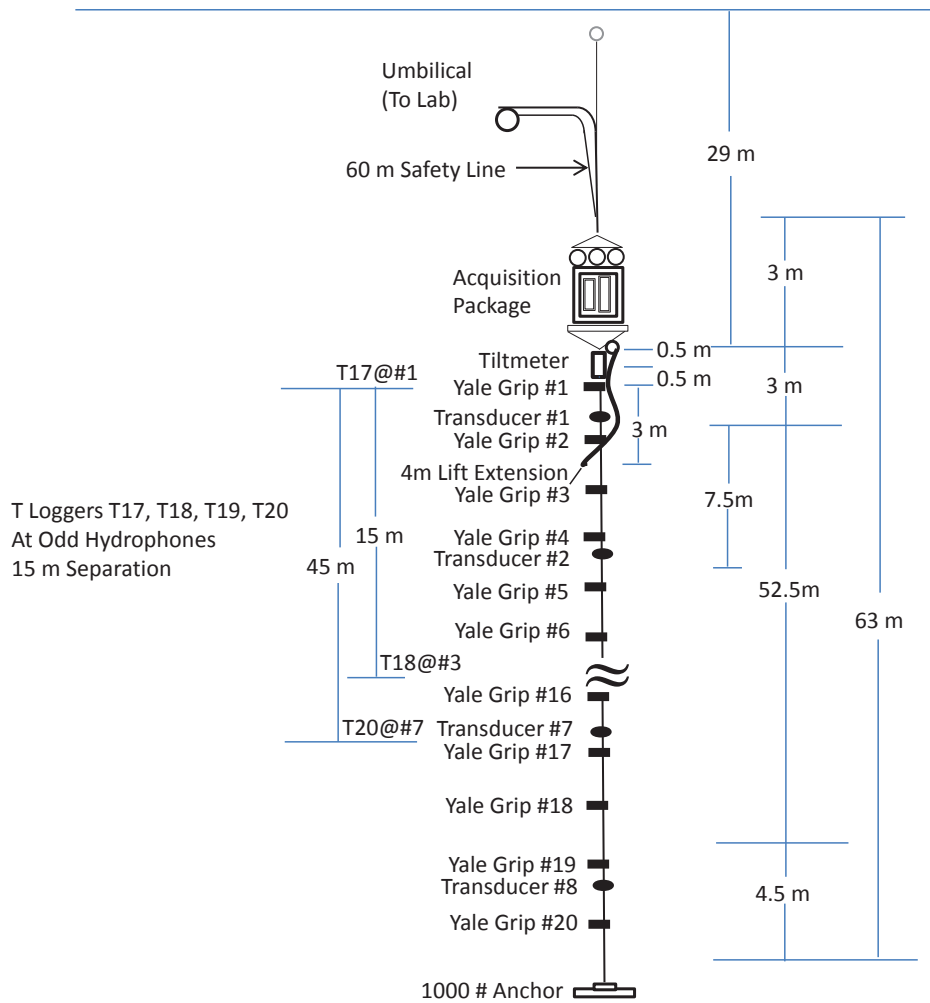
Figure 3.10: Scheme of the vertical-array receiver adopted in the KAM08 experiment (taken from [2]).

Our first purpose is to verify the presence of non-negligible ICI in the experimental data. To do this, we estimate the ICI power by exploiting a probe OFDM signal, operating in the band spanning 12.5 kHz to 25 kHz. The signal incorporates 2048 subcarriers, with a subcarrier spacing of 6.1 Hz, a frame length of 164 ms, and a silence interval of 100 ms between two consecutive frames — since the channel delay spread was estimated to be on the order of 10 ms [59], interframe interference can be safely selected. The OFDM signal was structured such that only one of every eight carriers was modulated with a BPSK symbol, while all other carriers were not used. According to (3.4), under the reasonable assumption that the ICI between subcarriers with a
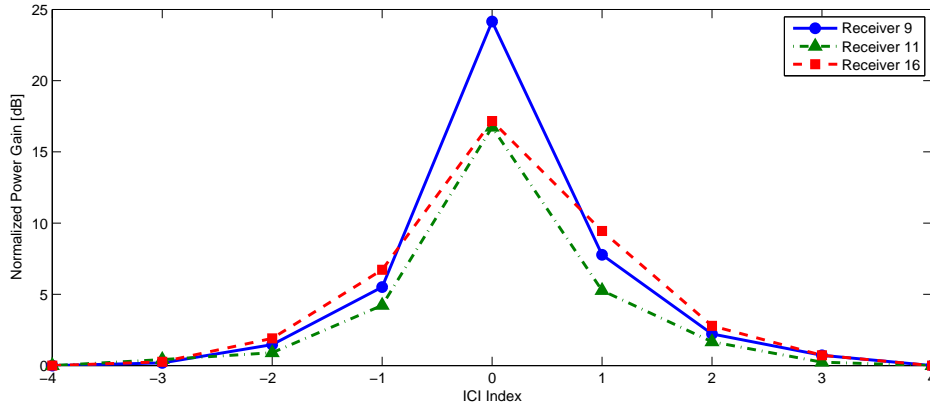
Figure 3.11: Estimates of the average power of the main tap (ICI index 0) and various ICI coefficients.

separation of at least eight positions is negligible, each sample $Y(k)$ can be rewritten as

$$Y(k) = C(k, \hat{m})X(\hat{m}) + N(k), \qquad (3.13)$$

where $\hat{m}$ is the index of the non-silent subcarrier closest to k. Hence, according to (3.13), the power of the sample $Y(k)$ provides a (noisy) estimate of the power of $C(k, \hat{m})$, since the BPSK symbols are such that $|X(\hat{m})| = 1$. Fig. 3.11 shows the average power of the estimated ICI coefficients for three different elements in the receiver array, in the case of transmissions from element 8 (that is, the deepest one, at a depth of 82.5 m) in the source array. At the receiver side, elements 9, 11, and 16 were at depths of 68.5 m, 61 m, and 42.25 m, respectively. As expected, the average ICI power decreases as the magnitude of the ICI index increases. Note that, on average, the ICI power from the two closest carriers (ICI index ± 1) is much lower than that of the main tap (ICI index 0), but significantly greater than that of the weakest ICI coefficients and that of the noise. Particularly, we point out that the ICI power from the two closest carriers is, on average, from 4-dB to 9-dB greater than the noise power, depending on the receiver considered, which suggests that the ICI should be accounted for in the receiver design. Also, Fig. 3.11 shows that the assumption of neglecting the ICI between non-consecutive carriers, as we did in the derivation of the FD-LE technique, is a good approximation.

Let us now consider communication data collected in the same experiment. We first focus on the results for a 2048-carrier OFDM system adopting a BPSK modula-

Receiving elements	Standard	FD-LE	FD-DFE
9	5.2%	4.3%	4.5%
16	12.1%	10.0%	10.8%
9 and 16 (MRC)	2.2%	1.4%	1.5%

Table 3.1: Uncoded BER in the fixed-source scenario

tion. The signal has a frequency band spanning 12 kHz to 20 kHz and a cyclic prefix of 20 ms, which implies a word duration of 276 ms. In each OFDM word, one symbol every four is used as a pilot symbol, and 36 symbols are reserved for peak-to-average power ratio (PAPR) reduction purposes, so that there are 1500 information bits. An example of the performance of different detection schemes is reported in Table 3.1, for the case of transmissions from element 8 and reception at elements 9 and 16. We considered single-element processing as well as multi-element processing with maximal-ratio combining (MRC). The reported results are obtained by averaging the uncoded BER over 12000 information bits transmitted in a few consecutive seconds. The equalizers have been implemented with one-tap filters and all parameters have been optimized for each OFDM word, which led to the following ranges: $\gamma_i \in [0.06, 0.15]$, $G_1 \in [0.25, 1.2]$, and $G_2 \in [0.00025, 0.012]$. Similar results were obtained by processing data recorded at different times during the experiment, and considering different elements both at the transmitter and the receiver side. According to the terminology of Section 3.4.1, this scenario is noise-limited, particularly when the receiving element 9 is considered: the performance improvement provided by ICI mitigation is relatively limited. The fact that the scenario is noise-limited might seem in contrast with the estimates in Fig. 3.11, which show that the power of the ICI due to the closest carriers is, on average, much greater than the noise power. Insights into this fact are given by the results reported in Fig. 3.12, where the estimated magnitude of the main coefficient (ICI index 0) is shown, together with the positions of the decoding errors for the FD-DFE technique. It is clear that the errors occur mostly where the channel has spectral notches, that is, where the system is very likely to be noise-limited, which is not in contrast with the estimates in Fig. 3.11, since the latter quantities are averages over the entire spectrum.
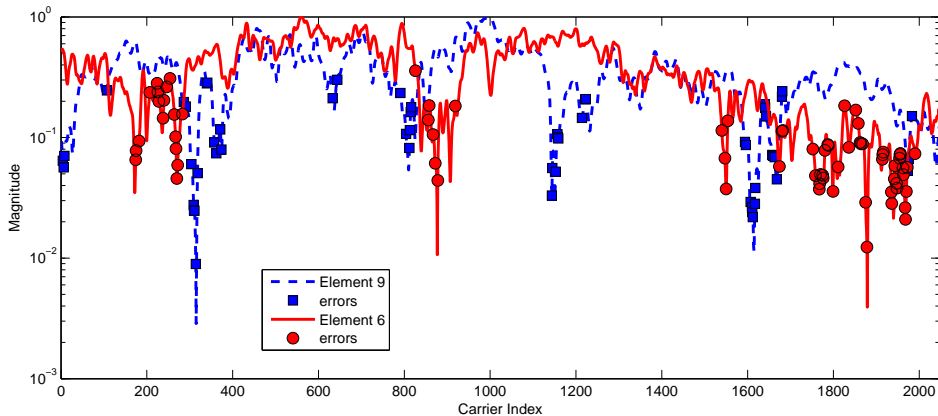
Figure 3.12: Estimated magnitude of the channel gain and positions of the decoding errors for two different receiving elements.

Finally, we point out that the BERs obtained in all considered scenarios are on the order of 2%-20% when only one receiving element is exploited, but it is possible to obtain BERs on the order of 1% (or lower) by combining the outputs of different receiving elements, that is, by exploiting the fact that the spectral notches occur at different frequencies for different elements (see Fig. 3.12). Particularly, by means of MRC over 3 elements, we are able to correctly detect all information bits in more than 95% of the processed frames. A very similar performance, i.e., no errors over 90% of the processed frames, is obtained also with QPSK-modulated signals, again by combining 3 receiving elements. In every considered scenario, the uncoded BER is well below the value that can be corrected by means of modern rate-1/2 channel codes. Hence, when such codes are used, we can confidently expect a BER on the order of 10^{-4} or less.

3.4.3   Results for the KAM08 Experiment — Towed-Source Scenario

We now consider the experimental data collected in the presence of motion between the transmitter and the receiver. Namely, the transmitter was submerged at a depth spanning 20 m to 50 m, depending on the specific experiment, and towed at a nominal speed of 3 knots (i.e., about 1.54 m/s), while the receiver was the same 16-element array described in Section 3.4.2. Particularly, we consider the case when the link range was approximately 2 km, and the towing ship was moving towards the fixed receiver, with

the transmitting transducer about 25 m below the sea surface. Unlike for the fixed-source experiment, no probe OFDM signal was transmitted. All reported results refer to communication signals adopting BPSK modulation, with the same OFDM format and pilot allocation as described in Section 3.4.2.

If the received signal is processed without the resampling stage, the information sequence cannot be recovered (a BER of 50% is observed). It is thus necessary to estimate the Doppler rate and to resample the received sequence accordingly. A coarse estimate of the Doppler rate can be obtained by exploiting the presence of the periodically-inserted probe signals that were transmitted in the KAM08 for Doppler-rate estimation. In this case, the estimate of the Doppler rate is $\widehat{a} = 1.14 \cdot 10^{-3}$, which is consistent with the actual status of the moving ship, since the value of $\widehat{a}$ corresponds to a speed of about 1.7 m/s towards the receiver, i.e., very close to the nominal speed of the towing ship. In the following, we show how the estimate $\widehat{a}$ impacts the performance of the various receiver blocks.

Let us start with the time synchronization algorithm, which immediately follows the resampling stage. We consider the time synchronization metric proposed in [52], implemented in the pure-correlation form. Fig. 3.13 shows the time synchronization metric obtained after resampling the signal received at element 5 with $\widehat{a} = 1.14 \cdot 10^{-3}$ (top figure) and $\widehat{a} = 1.67 \cdot 10^{-3}$ (bottom figure), both compared with the synchronization metric characterizing the transmitted signal, which is the metric obtained at the output of the transmitter and exhibits clear peaks every 276 ms (i.e., the duration of the OFDM word). Note that the metric obtained after resampling with $\widehat{a} = 1.14 \cdot 10^{-3}$ closely resembles the metric characterizing the transmitted signal, thus yielding to an effective time synchronization. On the other hand, Fig. 3.13 shows that, after resampling with $\widehat{a} = 1.67 \cdot 10^{-3}$, the metric is completely distorted and proper time synchronization cannot be achieved, which implies that no information can be recovered at the receiver side. By means of similar analyses, we could conclude that an accuracy of at least $5 \cdot 10^{-4}$ in the estimate of the Doppler rate is required for the time synchronization to work effectively.
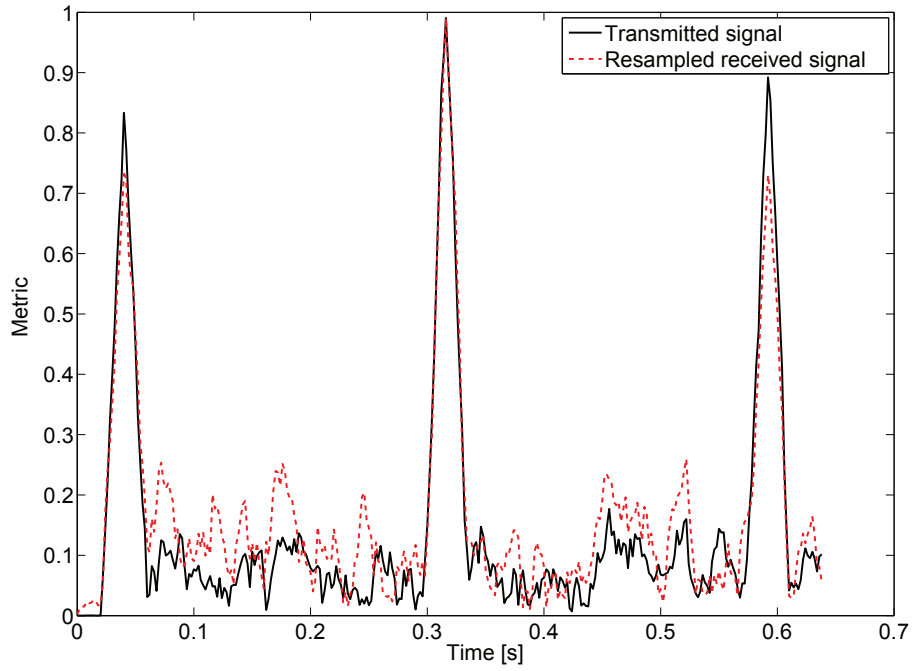
(a) Resampling with $\widehat{a} = 1.14 \cdot 10^{-3}$.
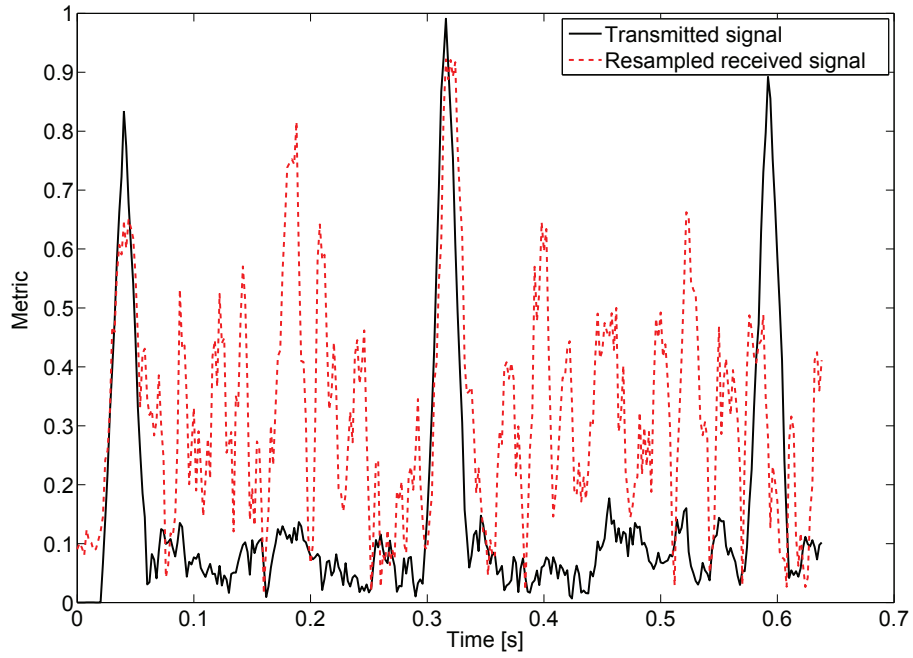
(b) Resampling with $\widehat{a} = 1.67 \cdot 10^{-3}$.

Figure 3.13: Comparison of different time synchronization metrics.

$\widehat{a} \cdot 10^3$	1.18	1.14	1.11	1.05	1.02	1.00
With Frequency Synchronization	2.9%	2.9%	2.9%	3.1%	3.1%	50.0%
No Frequency Synchronization	3.1%	3.0%	3.1%	14.9%	26.1%	36.3%

Table 3.2: Uncoded BER in the towed-source scenario when ICI is neglected

Next, we evaluate how the estimate $\widehat{a}$ affects the frequency synchronization stage. Table 3.2 compares the uncoded BER performance of the standard receiver that neglects the ICI, with and without the frequency synchronization stage of the signal received at element 5. Note that, when no frequency synchronization is performed, the accuracy of the Doppler rate estimation is very critical for the BER performance, while it is not critical when frequency synchronization is performed, for a wide range of values of $\widehat{a}$. These (and other) results suggest that, provided that the accuracy in the estimation of the Doppler rate is on the order of $1.4 \cdot 10^{-4}$ or less, the residual Doppler shift after resampling can be effectively compensated for by the frequency synchronization algorithm. However, when the residual Doppler shift is such that the resulting frequency offset does not belong to the acquisition range of the frequency synchronization algorithm, the ICI-neglecting receiver completely fails (see the entry $\widehat{a} = 10^{-3}$ in Table 3.2). Interestingly, as shown in Table 3.3 for the case of MRC of element 5, 8, and 16, the robustness to the residual Doppler shift can be greatly improved if ICI mitigation is adopted, again with FD-DFE outperforming FD-LE. In this case, the first run of both FD equalizers is effectively driven only by the pilot symbols, since the preliminary decisions obtained by standard detection are basically random (see the entry "Standard Approach" in Table 3.3). Hence, it is useful to execute multiple iterations of the equalizer, using as preliminary decisions the equalizer output at the previous iteration. The results shown in Table 3.3 refer to the case of six iterations for both ICI-mitigation schemes. The other parameters are: $\gamma_i \in [0.06, 0.09]$, $G_1 \in [0.8, 2.95]$, $G_2 \in [0.007, 0.0011]$, and three-tap filters. The improvements provided by ICI mitigation are consistent with the fact that, ultimately, the effect of a residual Doppler shift is ICI [9].

After evaluating the impact of the accuracy in the Doppler rate estimation, we finally discuss the detection performance obtained when the actual estimate $\widehat{a} = 1.14 \cdot 10^{-3}$

$\Delta a \cdot 10^3$	0.00	0.14	0.16	0.19	0.21	0.23	0.25
Standard Approach	0.3%	35.7%	43.1%	50.0%	50.0%	50.0%	50.0%
FD-LE	0.1%	4.5%	4.0%	3.3%	2.8%	3.2%	4.1%
FD-DFE	0.1%	0.7%	0.7%	0.9%	1.1%	1.1%	1.2%

Table 3.3: Uncoded BER in the towed-source scenario when frequency synchronization is not achieved

is adopted in the resampling stage. In this case, after proper compensation of the Doppler shift, most of the data collected in the KAM08 experiment seem to correspond to noise-limited scenarios, for which ICI mitigation does not provide a remarkable performance improvement with respect to the standard receivers. This fact suggests that, compared to the duration of the OFDM words, the channel variations were relatively slow in that environment. It is interesting to evaluate how such conclusions would change in a more challenging UWA environment, with faster time variations. A simple procedure that allows us to introduce artificial time variations in the experimental data consists of resampling the received signal with time-varying rate. Formally, the sequence is resampled so that, for the n-th sample, the difference between the nominal sampling time nT_s and the actual sampling time is $\Lambda(n)$. Note that the obtained sequence is basically equivalent to a sequence obtained with ideal sampling rate when the multipath propagation is characterized by the time-varying delay $\Lambda(n)$. We here consider $\Lambda(n)$ generated according to a zero-mean Gaussian random walk with standard deviation $\sigma_e \cdot T_s$, σ_e being a tunable parameter. A realization of the process $\Lambda(n)$ with $\sigma_e = 0.005$ is shown in Fig. 3.14. Note that, within an observation window of 250 ms (i.e., roughly the duration of the considered OFDM word), the variations of $\Lambda(n)$ are on the order of the nominal sampling interval $T_s = 20\mu$s. Interestingly, this value corresponds to a variation of about 2 cm in the length of the propagation paths, which seems to be a realistic variation in 250 ms, for many practical UWA environments. Average values of the uncoded BER obtained by processing the resampled sequences are reported in Table 3.4 for three different values of σ_e and three different detection algorithms with MRC of elements 5, 8, and 16. The results refer to the case of three iterations for both ICI-mitigation schemes. The other parameters are: $\gamma_i \in [0.06, 0.2]$,
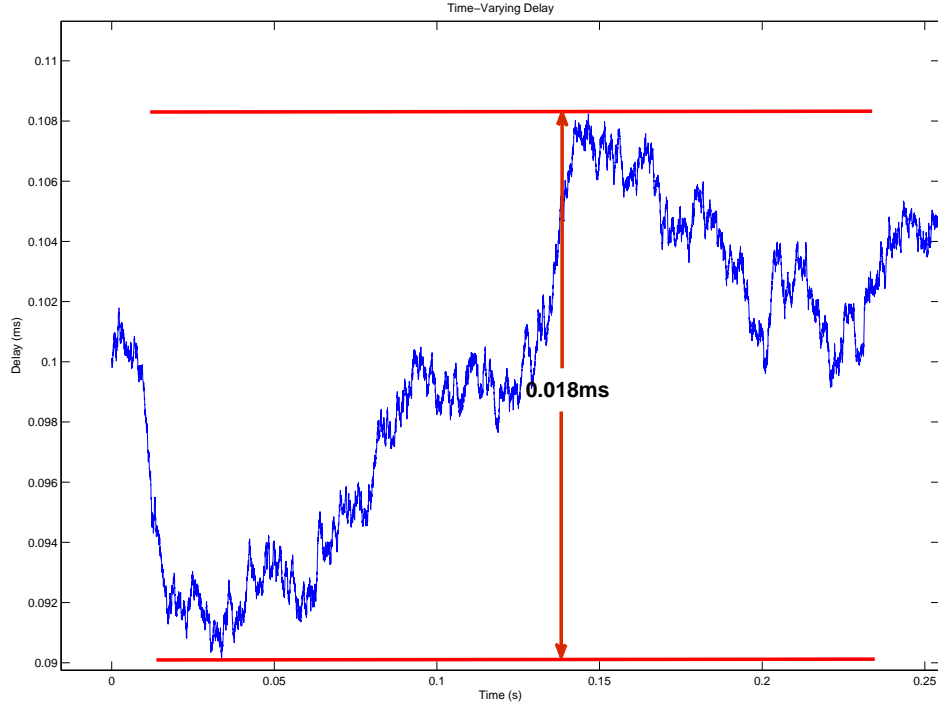
Figure 3.14: A realization of the process $\Lambda(n)$ with $\sigma_e = 0.005$.

$\sigma_\epsilon \cdot 10^3$	Standard Approach	FD-LE	FD-DFE
15.0	16.1%	13.6%	1.0%
10.0	7.3%	7.1%	0.5%
5.0	1.2%	0.9%	0.2%

Table 3.4: Uncoded BER for the intentionally-degraded experimental data

$G_1 = 0.8$, $G_2 = 0.007$, and three-tap filters. Note that the FD-LE does not provide a significant performance improvement with respect to the ICI-neglecting receiver, which shows that the effectiveness of the FD-LE is greatly compromised when the estimation of the ICI coefficients is critical. On the other hand, the FD-DFE is very robust to time-varying propagation delays, and emerges as a promising solution for UWA channels with more challenging time variations than those characterizing the data collected in the KAM08 experiment.

3.5 Chapter Summary

We have considered OFDM transmissions over time-varying UWA channels, comparing the performance of standard receivers neglecting ICI with that achievable by means of two ICI-mitigation schemes. In the first scheme, the ICI coefficients are explicitly estimated by means of a closed-loop tracking system, and FD-LE equalization based on such estimates is performed. In the second scheme, detection is performed by means of an adaptive FD-DFE, which does not require explicit ICI estimation. Simulation results show that in ICI-limited scenarios both techniques provide a significant performance improvement with respect to the standard OFDM receivers, typically with FD-DFE being more effective than FD-LE. Receivers employing ICI mitigation outperform the standard ones in the decoding of real UWA data from the recent KAM08 experiment, particularly when scenarios with motion between the transmitter and the receiver are considered. In these cases, ICI mitigation significantly increases the robustness of the receiver to imperfect compensation of the motion-induced Doppler shift. Finally, we have shown the potential of the ICI-mitigation schemes in coping with more challenging time variations than those characterizing the environment of the KAM08 experiment. These results serve as an encouragement to investigate related decision-feedback structures, such as those that exploit both forward and backward directions for adaptive detection of symbols in an OFDM block.

Chapter 4

RECEIVER DESIGN FOR OFDM OVER DOPPLER-DISTORTED UNDERWATER
ACOUSTIC CHANNELS

As discussed in Chapter 3, rapid time variations of UWA channels cause significant
ICI for systems using OFDM. Responding to this challenge, we have developed two
frequency domain adaptive equalizers, namely FD-DFE, and FD-LE, aiming at effec-
tive ICI mitigation with significantly reduced pilot overhead. To make these frequency
domain equalizers robust against phase rotations due to timing synchronization errors,
we have also integrated phase tracking loops into the overall equalizer designs. The
effectiveness of our frequency domain equalizers have been verified with simulated con-
ditions as well as real data recorded in the KAM08 experiment. Note that the UWA
channels in the simulations as well as those observed in the experiment all have very
similar Doppler scaling factors for different signal arrivals. In this case, after an initial
ICI mitigation stage (implemented as a single-rate resampling operation), the ICI due
to the residual Doppler distortion can be restricted to a few neighboring subcarriers
and effective ICI mitigation can be achieved.

In this chapter, we are particularly interested in scenarios where different clusters
of arrivals are characterized by significantly different Doppler scaling factors. These sce-
narios can be easily motivated for certain transmitter/receiver geometries, or in general,
by a cooperative communications framework, where distributed transmitter-receiver
pairs may experience significantly different Doppler distortions (e.g., two vehicles mov-
ing in different directions with respect to the receiver). As such, the conventional ap-
proach of front-end resampling that corrects for a *common* Doppler scaling factors may
fail, rendering a post FFT signal that is contaminated by path or transmitter-specific
inter-carrier interference. To counteract this problem, we propose a new family of front-
end receiver structures that utilize multiple resampling branches, each coping with the
Doppler scaling of a particular cluster of arrivals or transmitter. Followed by FFT
demodulation, the new structures yield a set of Doppler-mitigated frequency domain

samples, which are subsequently processed using custom-designed, linear or nonlinear detection schemes. To make these designs suitable for practical applications, a family of specialized channel estimators for the path gains and delays, as well as the Doppler scaling factors of each arrival are also developed. The effectiveness and robustness of the proposed receivers are demonstrated via simulations and with real data collected the 2010 MIMO acoustic communications experiment (MACE10) and the Kauai Acomms MURI 2008 (KAM08) experiment.

The chapter is organized as follows. Section 4.1 gives a review of the existing research results and summarizes the proposed approach. Section 4.2 contains the OFDM system description. In Section 4.3, for a SISO system with a path-specific Doppler distortion, we derive sufficient statistics for data detection, and outline the front-end receiver structure based on an efficient FFT implementation. In Section 4.4, we extend the results to cooperative MIMO scenarios and focus on the user-specific Doppler distortion. The custom-designed detection schemes are also discussed in the multiuser communication context. Section 4.5 is focused on some practical considerations involving sparse channel estimation schemes. Section 4.6 offers data decoding results via simulations and experimental data studies, and finally, Section 4.7 concludes the chapter.

4.1   Introduction

As demonstrated in several recent shallow-water acoustic communications experiments, both SISO and MIMO OFDM systems are able to yield successful results $[6, 8, 10, 11]$ without resorting to complicated equalizer structures essential for the case of single-carrier systems. While the previous OFDM systems are mostly tested for single-user (point-to-point) transmissions, it is also possible, and in fact may be preferable to deploy them in a multiuser environment. Multiuser MIMO systems, differently from their single user counterparts where both the transmitting and the receiving elements are collocated, are formed by transmitting and/or receiving elements that are geographically

separated [37]. Multiuser MIMO leverages multiple users as an extra degree of freedom and promises large gains for both capacity [60] and reliability [17]. While multiuser MIMO may include a broad range of configurations, such as MIMO broadcast in [61], MIMO multiple-access (MAC) in [62], and network MIMO in [63]; in this chapter, the focus is on MIMO MAC, where distributed users (operating in the same frequency band simultaneously) transmit independent data streams to a centralized receiver comprised of collated receiving elements. The major challenge for both single-user and multiuser systems is that with the low propagation speed of sound in water (nominally 1500 m/s), the Doppler distortion becomes much more severe than that typically observed in terrestrial radio communications, causing significant time variations and intercarrier interference (ICI).

To address the issues related to time variations and the Doppler-induced ICI, a variety of receiver designs have been proposed in the literature [9, 13, 26]. We note that although receivers with general ICI-mitigation techniques are available such as the adaptive frequency-domain equalizers proposed in Chapter 3 (reported in [10, 40]), most existing receiver designs are dedicated to channels where the only source of ICI is the motion-induced Doppler scaling, i.e., the time compression/dilation that the signal experiences during propagation [9, 12, 51]. In this case, it is typically assumed that all the propagation paths are characterized by approximately the same Doppler scaling factor, which can be mitigated by resampling the received signal in order to compensate for the time compression/dilation [12]. While this assumption may be accurate for certain cases, it does not hold true in general. For example, in a single-user environment, given a particular geometry of the propagation paths and the transmitter/receiver motion (as depicted in Figure 4.1), significant difference of the Doppler scaling factors may arise when different propagation paths have significantly different lengths and experience significantly different length variations. For multiuser systems, this disparate nature of Doppler scaling factors may be even more pronounced, since different users are likely to move in different directions with respect to the receiver, and hence observe significantly different Doppler scaling factors as illustrated in Figure 4.2. Here, node 0 moves perpendicularly with respect to the receiver, rendering $a_0 \approx 0$, while node 1 and 2 move

46
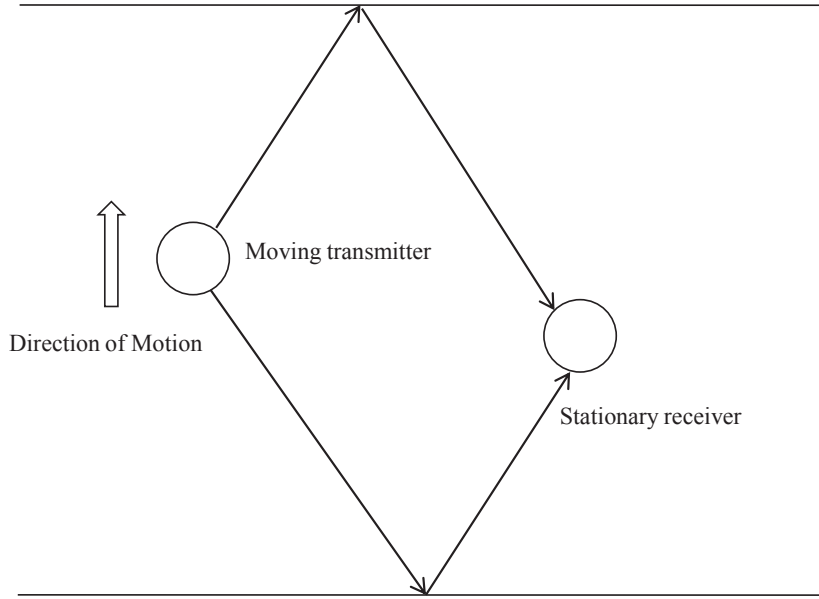
Figure 4.1: Path-specific Doppler arising from motion of the transmitter.

towards and away from the receiver, respectively, giving rise to $a_1 > 0$ and $a_2 < 0$.

To address the challenges posed by the disparate Doppler scaling factors, a remedy for the single-resampling designs has been proposed in [30]. Aiming at obtaining an accurate approximation to the sufficient statistics for data detection, the key idea of this approach is to optimize the resampling rate in such a way that the resultant equivalent discrete channel model has a Fisher information which is close to that associated with the channel model characterizing the sufficient statistics. To achieve this goal, the authors of [30] consider two different optimization criteria: (1) maximization of the trace of the Fisher Information Matrix (FIM), and (2) minimization of the mean square error (MSE) of a channel estimation problem. While conceptually appealing, due to the complexity of the cost function, the closed-form expression for the optimal resampling rate is intractable (particularly when the first criterion is applied), and therefore, a brute-force approach may be needed. Applying the second criterion, the authors obtain a suboptimal solution, which points out that when the received signal is dominated by one strong arrival, the resampling rate should be the Doppler scaling factor of this strong arrival, while when the arrivals have almost equal power, the resampling rate

47
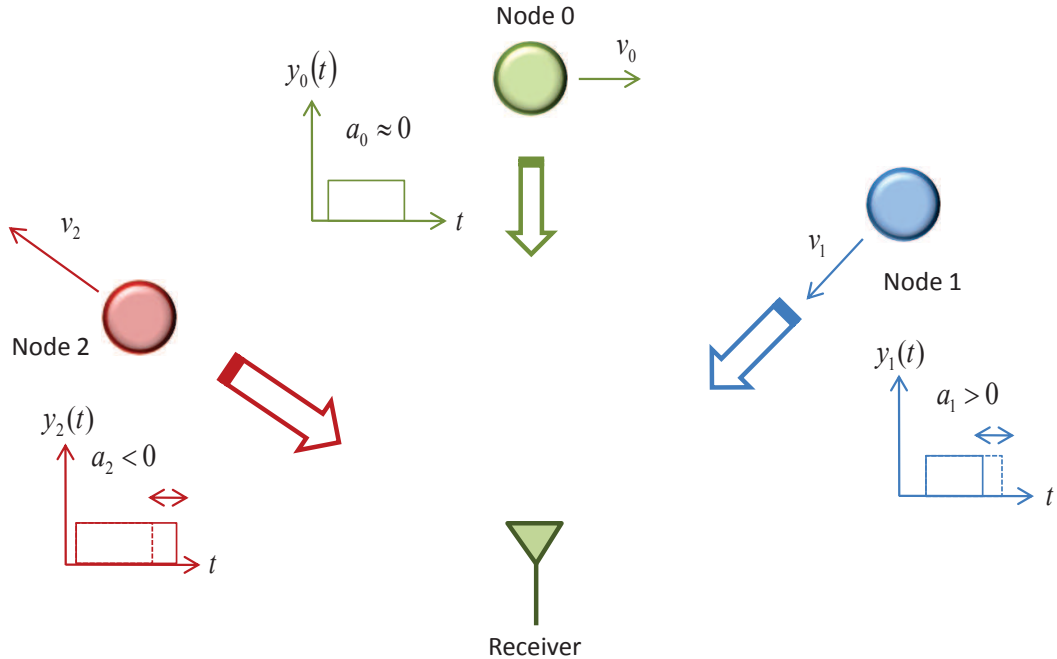
Figure 4.2: User-specific Doppler distortions arising from motion of the transmitting nodes.

should be the average of their associated Doppler scaling factors. We point out that while properly choosing the resampling rate may improve the performance, the system may still suffer from severe ICI when the Doppler scaling factors are significantly different for different paths. Also, note that this approach has only been investigated for single-user scenarios, while extensions to multiuser scenarios may also be of interest.

In this chapter, we address the design of an advanced receiver structure – in the sense of coping with the user/path-specific Doppler distortions – and find that the receiver should include multiple resampling branches, one for each distinct Doppler scaling factor associated with different users or different propagation paths of the same user [64, 65]. FFT demodulation of the resampling branch outputs yields a set of Doppler-mitigated frequency domain samples, which can be subsequently exploited by various detection schemes. For the single-user case, we focus on (1) maximum likelihood (ML) detection, and (2) linear detection based on least squares (LS) or minimum mean squared error (MMSE) optimization criteria. For the multiuser case (also appli-

48

cable to single-user MIMO communications), the detection is upgraded by (1) dealing with the redundancy in the observation vector, and (2) introducing a new nonlinear detection algorithm based on interference cancellation (IC). For all of these schemes, we explicitly estimate the path gains, delays, and Doppler scaling factors of different arrivals. Particularly, we propose a robust two-step sparse channel estimation approach which exploits the initial channel estimates obtained by standard compressive sensing techniques [51, 66] and provides a gradient-descend-based refinement step to cope with the basis mismatch problem. We demonstrate the effectiveness of these receiver designs both through extensive simulations and using data recorded in MACE10 [67] and KAM08 [2] experiments. In particular, to emulate a data set with an extensive set of Doppler rate differences for different users, we resample the recorded signal at different rates and add the resampled signals to form a compound signal, which is used as the input to different receiver structures. To assess the performance of the proposed receivers, we compare the results with those obtained by a standard receiver, for which only a single resampling branch is employed.

4.2 System Model and Preliminaries

In this section, we establish mathematical models for both single-user and multiuser UWA OFDM transmission scenarios. For the former, our focus is on the path-specific Doppler distortion, where a SISO system model is adopted, while in the latter, both path-specific and user-specific Doppler distortions are investigated, for which we use a distributed MIMO system setup.

4.2.1 Path-Specific Doppler

Consider an N-subcarrier OFDM system with a cyclic prefix (CP) duration T_g, a block duration T, and modulation symbols belonging to a complex-valued constellation. The transmitted signal can be written as [25]

$$s(t) = \text{Re}\left\{ \sum_{k=0}^{N-1} d_k e^{j2\pi f_k t} R(t) \right\} \tag{4.1}$$

49

where $\{d_k\}$ are the data symbols modulated onto the frequency $f_k = f_0 + k/T$, $R(t)$ is the modulation pulse of duration $T + T_g$, and Re$\{\}$ denotes the real part of its argument. Throughout the chapter we assume that the CP duration is sufficiently long to prevent inter-block interference. Hence, we focus on a single-block OFDM signal. Further, we assume that $R(t)$ is a rectangular pulse and note that the arguments in this chapter can be generalized to an arbitrary shaping pulse in a straight-forward manner.

Receivers for OFDM signals transmitted over time-invariant multipath channels have been well studied [25]. Here, we address the design of receivers for time-varying multipath channels in which the time variations are caused by path-specific and/or user-specific Doppler scaling factors, where the latter is typically seen in multiuser scenarios but also can be observed in single-user systems as well. For ease of illustration, we first focus on the path-specific Doppler distortion in SISO systems, deferring the extension to the MIMO systems to Section 4.2.2. In particular, we consider a UWA channel, whose propagation paths can be grouped into N_c clusters, each sharing a *common* Doppler scaling factor. The input-output relationship in the absence of noise is formulated as

$$y(t) = \sum_{c=0}^{N_c-1} \sum_{p=0}^{N_p^{(c)}-1} h_{c,p} s\left(t + a_c t - \tau_{c,p}\right) \tag{4.2}$$

where $N_p^{(c)}$ is the number of paths in the cth cluster, $h_{c,p}$, $\tau_{c,p}$, and a_c are, respectively, the path gain, delay, and Doppler scaling factor of the pth path in the cth cluster. For example, as illustrated in Figure 4.1, this model may apply to a scenario where the surface and bottom reflected paths are associated with significantly different angles of arrivals and the transmitter movement is towards the ocean surface. Note that while the channel is time-varying, in many cases the parameters change slowly and can be taken as constants for the frame duration. Denoting by $v^{(c)}$ the velocity of the relative transmitter-receiver motion along the propagation paths of the c-th cluster, the path-specific Doppler scaling factor is $a_c = v^{(c)}/v_s$, where v_s is the speed of sound in water. For typical UWA systems, we have $|a_c| \ll 1$.

Based on (4.2), we can write the received (bandpass) signal as

$$\widetilde{v}(t) = \text{Re}\left\{\sum_{k=0}^{N-1}\sum_{c=0}^{N_c-1}\sum_{p=0}^{N_p^{(c)}-1} d_k h_{c,p} e^{j2\pi f_k(t+a_ct-\tau_{c,p})} R(t + a_ct - \tau_{c,p})\right\} + \widetilde{w}(t) \quad (4.3)$$

where $\widetilde{w}(t)$ is additive white Gaussian noise (AWGN) with power spectral density (PSD) $N_0/2$.[1] Equivalently, adopting the complex envelope representation with respect to the frequency f_0, the model of the received signal yields

$$v(t) = \sum_{k=0}^{N-1} d_k P_k(t) + w(t) \quad (4.4)$$

where $w(t)$ is a circularly-symmetric complex AWGN with PSD N_0, and

$$P_k(t) = \sum_{c=0}^{N_c-1}\sum_{p=0}^{N_p^{(c)}-1} \alpha_p^{(c)}(k) e^{j2\pi a_c f_0 t} e^{j2\pi(t+a_ct)k/T} R\left(t + a_ct - \tau_{c,p}\right),$$

$$\alpha_p^{(c)}(k) = h_{c,p} e^{-j2\pi f_k \tau_{c,p}}. \quad (4.5)$$

4.2.2 User-Specific Doppler

We consider a scenario where N_t independent data streams $\mathbf{d}^{(1)}, \ldots, \mathbf{d}^{(N_t)}$ are transmitted simultaneously from N_t geographically separated transmitters, and received by a centralized receiver equipped with N_r receiving elements. This model is mathematically the same as that of a centralized MIMO system employing spatial multiplexing [68]. Denoting by $d_k^{(i)}$ the transmitted symbol at the k-th subcarrier of the i-th user, the transmitted signal from this user is given by

$$s_i(t) = \text{Re}\left\{\sum_{k=0}^{N-1} d_k^{(i)} e^{j2\pi f_k t} R(t)\right\}. \quad (4.6)$$

Similar to the SISO system model, a cyclic prefix (CP) of duration T_g is employed. In general, the Doppler scaling that arises in these systems is both user-specific and path-specific, the former being a direct consequence of different users' motion in different directions with respect to the receiver.

For simplicity, we consider a scenario with only a user-specific Doppler – interested readers are referred to Appendix A for the general case. The input-output

[1]Noise in a UWA channel is in general colored, but we focus for simplicity on the white noise case as an illustrative example. Extensions of the chapter's results to a specific noise PSD is straightforward as will become clear later in the chapter.

relationship (in the absence of noise) between the ith transmitter and the mth receiver can be modeled as

$$y_{i,m}(t) = \sum_{p=0}^{N_p^{(i,m)}-1} h_p^{(i,m)} s_i \left(t + a^{(i)}t - \tau_p^{(i,m)} \right) \tag{4.7}$$

where $N_p^{(i,m)}$ is the number of paths, $h_p^{(i,m)}$ and $\tau_p^{(i,m)}$ are respectively the path gain and delay of the pth path, and $a^{(i)}$ is the Doppler scaling factor associated with the ith transmitter. Denoting by $v^{(i)}$ the relative velocity of the i-th user with respect to the centralized receiver, the user-dependent Doppler scaling factor is $a^{(i)} = v^{(i)}/v_s$. Note that for relative velocities in the order of a few meters per second, the values of the Doppler scaling factor is in the order of $\cong 10^{-3}$.

Following a similar procedure as in Section 4.2.1, we express the baseband signal of the mth receiving element as

$$v_m(t) = \sum_{i=1}^{N_t} \sum_{k=0}^{N-1} d_k^{(i)} P_k^{(i,m)}(t) + w_m(t) \tag{4.8}$$

where $w_m(t)$ is a circularly-symmetric complex AWGN with power spectral density (PSD) N_0, and

$$\begin{aligned}
P_k^{(i,m)}(t) &= \sum_{p=0}^{N_p^{(i,m)}-1} \alpha_p^{(i,m)}(k) e^{j2\pi a^{(i)} f_0 t} e^{j2\pi \left(t+a^{(i)}t\right)k/T} R\left(t + a^{(i)}t - \tau_p^{(i,m)}\right), \\
\alpha_p^{(i,m)}(k) &= h_p^{(i,m)} e^{-j2\pi f_k \tau_p^{(i,m)}}.
\end{aligned} \tag{4.9}$$

4.3   Single-User Receiver Design with Path-Specific Doppler Scaling

We propose new receiver design to address the path-specific Doppler distortions for the aforementioned single-user transmissions.

4.3.1   Comments on the Sufficient Statistics

We consider transmission of a single OFDM block assuming perfect channel state information at the receiver, i.e. the knowledge of Doppler scaling factors as well as the channel path gains and delays. Since the noise process is white Gaussian, maximum-likelihood (ML) data detection aims to find the sequence $\mathbf{d} = [d_0, \ldots, d_{N-1}]^{\mathrm{T}}$ which

minimizes the metric

$$\Lambda \left(\mathbf{d} \right) = \int_{-\infty}^{\infty} \left| v(t) - \sum_{k=0}^{N-1} d_k P_k(t) \right|^2 dt \qquad (4.10)$$

which implies a set of sufficient statistics given by

$$y_k = \int_{-\infty}^{\infty} v(t) P_k{}^*(t) dt, \quad k = 0, 1, \ldots, N - 1. \qquad (4.11)$$

For the desired sufficient statistics (4.11), a direct implementation of parallel matched-filter branches for all N sub-carriers is clearly not a viable option. We thus focus on an alternative interpretation of the expression (4.11). Namely, we first restrict our attention to the time interval that contains the signal but not its cyclic extension, which effectively yields

$$\begin{aligned} y_k &\approx \int_0^{\frac{T}{1+a_c}} v(t) \sum_{c=0}^{N_c-1} \sum_{p=0}^{N_p^{(c)}-1} \alpha_p^{(c)}(k)^* e^{-j2\pi a_c f_0 t} e^{-j2\pi(t+a_c t)k/T} dt \\ &= \sum_{c=0}^{N_c-1} \int_0^{\frac{T}{1+a_c}} \underbrace{v(t) e^{-j2\pi a_c f_0 t}}_{v^{(c)}(t)} \sum_{p=0}^{N_p^{(c)}-1} \alpha_p^{(c)}(k)^* e^{-j2\pi(t+a_c t)k/T} dt, \end{aligned}$$

where, for each cluster index c, $v^{(c)}(t)$ is obtained by compensating for the Doppler-induced frequency shift $a_c f_0$. Defining

$$\alpha^{(c)}(k) = \sum_{p=0}^{N_p^{(c)}-1} \frac{\alpha_p^{(c)}(k)}{(1+a_c)}, \qquad (4.12)$$

a new time variable $\xi = (1 + a_c) t$, and

$$\tilde{y}_k^{(c)} = \int_0^T v^{(c)} \left(\frac{\xi}{1+a_c} \right) e^{-j2\pi k\xi/T} d\xi, \qquad (4.13)$$

equivalently, we can write

$$y_k \approx \sum_{c=0}^{N_c-1} \alpha^{(c)}(k)^* \tilde{y}_k^{(c)}. \qquad (4.14)$$

We point out that $\tilde{y}_k^{(c)}$ in this computation can be efficiently carried out for all the subcarriers at a single time, since the integration in Equation (4.13), when carried out in the discrete-time domain, is nothing but an FFT. With Equation (4.13), we also notice that evaluation of $\tilde{y}_k^{(c)}(t)$ requires resampling of $v^{(c)}(t)$ according to the Doppler

53
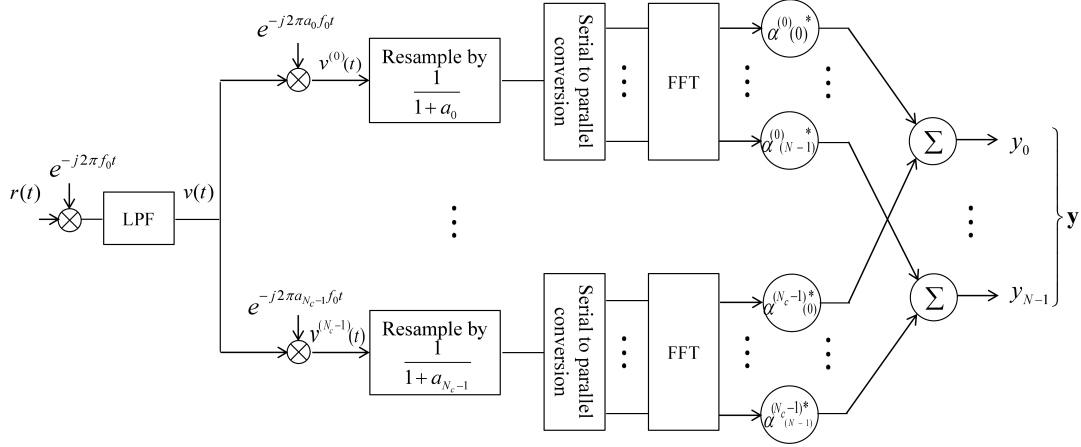
Figure 4.3: Proposed front-end receiver design for single-user systems.

scaling factor a_c when there are N_c distinct Doppler scaling factors. Inspired by the formulations in Equations (4.13) and (4.14), we propose to use a new receiver front-end design, which resamples the received signal $v(t)$ N_c times, each time according to a distinct Doppler scaling factor.

Figure 4.3 shows the block diagram of the receiver front-end. It consists of N_c parallel branches, each one associated with a group of arrivals with the same Doppler scaling. Each branch performs a frequency shift, resampling, and FFT. The implementation complexity is thus increased only linearly with the number of distinct Doppler scaling factors present, and the processing can be performed in parallel, rendering a computationally affordable solution.

4.3.2 Data Detection

We now describe post-processing schemes which aim at exploiting the output of the multiple resampling front-end design for high performance data detection.

4.3.2.1 Maximum-Likelihood Detection and Its Approximation

ML detection is the optimal solution in terms of minimizing the error rate. To pursue it, we first write the relevant discrete channel model for (4.11)

$$y_k = \sum_{m=0}^{N-1} \Phi_{k,m} d_m + w_k, \tag{4.15}$$

54

where

$$\Phi_{k,m} = \int_{-\infty}^{\infty} P_m(t)P_k^*(t)dt \tag{4.16}$$

and $\{w_k\}$ is additive Gaussian noise with autocorrelation

$$\Omega_{k,m} = E[w_k w_m^*] \approx N_0 T \Phi_{k,m} \tag{4.17}$$

The discrete channel model (4.15) is now formulated in the vectorial form, i.e.,

$$\mathbf{y} = \mathbf{\Phi d} + \mathbf{w} \tag{4.18}$$

where

$$\mathbf{d} = [d_0, \ldots, d_{N-1}]^{\mathrm{T}}$$

$$\mathbf{y} = [y_0, \ldots, y_{N-1}]^{\mathrm{T}}$$

$$\mathbf{w} = [w_0, \ldots, w_{N-1}]^{\mathrm{T}}$$

and $\mathbf{\Phi}$ represents the channel matrix, whose entries are defined by the expression in (4.16). Given the model in (4.18), we can write the joint probability density function (pdf) of the observation vector $\mathbf{y}$ conditioned on the data vector $\mathbf{d}$, i.e.

$$p(\mathbf{y}|\mathbf{d}) \propto \exp\left\{-(\mathbf{y} - \mathbf{\Phi d})^{\mathrm{H}} \, \mathbf{\Omega}^{-1} \, (\mathbf{y} - \mathbf{\Phi d})\right\} \tag{4.19}$$

where $^{\mathrm{H}}$ stands for the Hermitian transpose, and $\mathbf{\Omega}$ is the noise covariance matrix, whose entries are defined in (4.17).[2] With the conditional pdf, the ML solution can be written as

$$\tilde{\mathbf{d}}_{\mathrm{ML}} = \arg\max_{\mathbf{d}} \Lambda(\mathbf{d}) \tag{4.20}$$

where

$$\Lambda(\mathbf{d}) = (\mathbf{y} - \mathbf{\Phi d})^{\mathrm{H}} \, \mathbf{\Omega}^{-1} \, (\mathbf{y} - \mathbf{\Phi d}) \tag{4.21}$$

We then substitute the noise autocorrelation in (4.17) into (4.21), and hence obtain a simplified metric

$$\begin{aligned}
\Lambda(\mathbf{d}) &= (\mathbf{y} - \mathbf{\Phi d})^{\mathrm{H}} \left(\mathbf{\Omega}^{-1}\mathbf{y} - \gamma\mathbf{d}\right) \\
&= C_0 - 2\gamma \mathrm{Re}\left\{\mathbf{d}^{\mathrm{H}}\mathbf{y}\right\} + \gamma \mathbf{d}^{\mathrm{H}}\mathbf{\Phi}^{\mathrm{H}}\mathbf{d}
\end{aligned} \tag{4.22}$$

---

[2]$\mathbf{\Omega}$ is nonsingular except for some pathological cases, so the pdf can be written.

where $\gamma = (N_0 T)^{-1}$ and $C_0 = \mathbf{y}^{\mathrm{H}} \boldsymbol{\Omega}^{-1} \mathbf{y}$.

In general, the complexity of ML detection is prohibitive since the interference ranges over all N subcarriers. However, the correlation matrix $\boldsymbol{\Phi}^{\mathrm{H}}$ that defines the coupling of different subcarriers in (4.22) has a certain structure that can be exploited for an efficient implementation. Namely, if the Doppler scaling factors differ only by a small amount, this correlation metric will have only a few significant terms that relate the desired subcarrier to its close neighbors. As a result, when only the significant terms in (4.16) are kept, an approximate ML detector can be implemented using a proper application of the Viterbi algorithm. Otherwise, implementation of the Viterbi algorithm becomes infeasible, and suboptimal detectors must be considered.

4.3.2.2 Linear Detectors

With ML detection being computationally demanding even in an approximate form for larger Doppler scaling factor differences, we may alternatively pursue linear solutions for the data detection. These schemes, instead of minimizing the error probability, aim at minimizing the error between the linear detector output and the transmitted sequence. While the minimization of different error measures can result in various linear detectors, with the discrete channel model given in (4.18), we adopt two commonly used ones, namely the least squares (LS) detector

$$\tilde{\mathbf{d}}_{\mathrm{LS}} = \mathrm{Dec}\left(\left(\boldsymbol{\Phi}^{\mathrm{H}}\boldsymbol{\Phi}\right)^{-1}\boldsymbol{\Phi}^{\mathrm{H}}\mathbf{y}\right) \tag{4.23}$$

and the minimum mean squared error (MMSE) detector

$$\tilde{\mathbf{d}}_{\mathrm{MMSE}} = \mathrm{Dec}\left(\boldsymbol{\Phi}^{\mathrm{H}}\left(\boldsymbol{\Phi}\boldsymbol{\Phi}^{\mathrm{H}} + \boldsymbol{\Omega}\right)^{-1}\mathbf{y}\right) \tag{4.24}$$

where $\mathrm{Dec}\left(\cdot\right)$ represents the symbol decision. For instance, in binary shift keying (BPSK) the symbol decision is taken as the sign of the real part of the symbol estimate. The MMSE is usually a better option provided that the noise statistics are known.

4.4 Multiuser Receiver Design with User-Specific Doppler

With the advanced receiver structure derived for the single-user systems, we now pursue the advanced receiver design for the aforementioned multiuser MIMO scenario, where multiple geographically separated users transmit independent data streams to a centralized receiver. For these multiuser systems, users from different locations operate on the same frequency band and multiuser detection is made possible by combining signals received at multiple receiving elements exploiting the spatial diversity of the receiver array. We note that for the multiuser systems, both path and user-specific Doppler distortions are possible. For ease of illustration, we present the optimum receiver designs for a simplified case, for which only user-specific Doppler distortion occurs – interested readers are referred to Appendix A for extensions to more general scenarios, where both user and path-specific Doppler distortion may be encountered.

4.4.1 Comments on the Sufficient Statistics

Similar to Section 4.3, we consider the transmission of a single OFDM block assuming perfect receiver CSI. Since the noise is assumed white Gaussian, maximum-likelihood data detection, in the multiuser context, aims to find $\mathbf{d} = [\mathbf{d}^{(1)^{\mathrm{T}}}, \ldots, \mathbf{d}^{(N_t)^{\mathrm{T}}}]^{\mathrm{T}}$, which minimize the metric (since the noise is spatially and temporally white Gaussian)

$$\Lambda\left(\mathbf{d}\right) = \int_{-\infty}^{\infty} \sum_{m=1}^{N_r} \left| v_m(t) - \sum_{i=1}^{N_t} \sum_{k=0}^{N-1} d_k^{(i)} P_k^{(i,m)}(t) \right|^2 dt \tag{4.25}$$

where $\mathbf{d}^{(i)} = [d_0^{(i)}, d_1^{(i)}, \ldots, d_{N-1}^{(i)}]$. For the multiuser systems, the metric (4.25) implies a set of sufficient statistics given by

$$y_k^{(i,m)} = \int_{-\infty}^{\infty} v_m(t) P_k^{(i,m)^*}(t) dt, \quad k = 0, 1, \ldots, N-1. \tag{4.26}$$

With a similar complexity concern as in the single-user case, we aim to find a computationally efficient implementation for the acquisition of the sufficient statistics in (4.26). Following a procedure parallel to that in Section 4.3.1, we adopt the received signal in the interval that excludes the cyclic prefix, i.e.,

$$y_k^{(i,m)} \approx \alpha^{(i,m)}(k)^* \tilde{y}_k^{(i,m)} \tag{4.27}$$

57

where

$$\alpha^{(i,m)}(k) = \sum_{p=0}^{N_p^{(i,m)}-1} \frac{\alpha_p^{(i,m)}(k)}{1+a^{(i)}} \tag{4.28}$$

and

$$\widetilde{y}_k^{(i,m)} = \int_0^{\frac{T}{1+a^{(i)}}} \underbrace{v_m(t)e^{-j2\pi a^{(i)}f_0 t}}_{v_m^{(i)}(t)} e^{-j2\pi k\left(1+a^{(i)}\right)t/T}\,dt. \tag{4.29}$$

We then proceed by introducing a change of variable $\xi = \left(1 + a^{(i)}\right)t$ in expression (4.29), which results in

$$\widetilde{y}_k^{(i,m)} = \int_0^T v_m^{(i)}\left(\frac{\xi}{1+a^{(i)}}\right) e^{-j2\pi k\xi/T}\,d\xi. \tag{4.30}$$

Hence, the received signal $v_m(t)$ can first be shifted in frequency and resampled to obtain the signals $\left\{v_m^{(i)}\left(\frac{t}{1+a^{(i)}}\right)\right\}_{i=1}^{N_t}$. These signals can now be demodulated according to the expression (4.30), which, when cast in the discrete-time framework, is nothing but an FFT operation.

Figure 4.4 shows the block diagram of the receiver front-end. Similar to the single-user case, it consists of multiple parallel branches. The difference is that in the multiuser context one branch is associated with each individual user and there are N_t branches in total. Therefore, the implementation complexity of the proposed multiuser front-end design is increased only linearly with the number of users, which is computationally affordable by realizing that the computation of the N_t branches can be performed in parallel.

4.4.2   Data Detection

To arrive at the detection algorithms, it is helpful to define an equivalent discrete channel model that relates the acquired statistics (4.27) to the data symbols. Substituting the relations (4.8) and (4.9) into the expression (4.27), we obtain

$$y_k^{(i,m)} = \sum_{u=1}^{N_t} \sum_{l=0}^{N-1} \Phi_{k,l}^{(i,u)}(m)d_l^{(i)} + w_k^{(i,m)} \tag{4.31}$$

where

$$\Phi_{k,l}^{(i,u)}(m) = \int_0^T P_l^{(u,m)}(t)P_k^{(i,m)^*}(t)dt \tag{4.32}$$

58
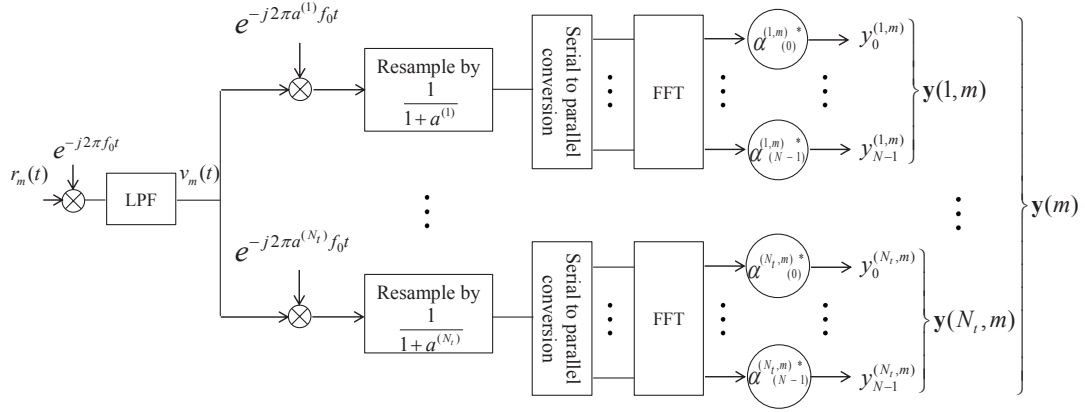
Figure 4.4: The multiple-resampling front-end for the mth receiving element.

and $w_k^{(i,m)}$ is additive Gaussian noise with autocorrelation

$$\Omega_{k,l}^{(i,u)}(m) = E[w_k^{(i,m)} w_l^{(u,m)^*}] \approx N_0 T \cdot \Phi_{k,l}^{(i,u)}(m).\tag{4.33}$$

Grouping all the carriers together, the above expressions can also be represented in a compact form as

$$\mathbf{y}(i,m) = \mathbf{\Phi}(i,m)\mathbf{d} + \mathbf{w}(i,m)\tag{4.34}$$

where

$$\mathbf{d} = [\mathbf{d}^{(1)^{\mathrm{T}}}, \ldots, \mathbf{d}^{(N_t)^{\mathrm{T}}}]^{\mathrm{T}}$$

$$\mathbf{\Phi}(i,m) = [\mathbf{\Phi}^{(i,1)}(m), \ldots, \mathbf{\Phi}^{(i,N_t)}(m)]$$

$$[\mathbf{\Phi}^{(i,u)}(m)]_{(k,l)} = \Phi_{k,l}^{(i,u)}(m)$$

$$\mathbf{y}(i,m) = [y_0^{(i,m)}, \ldots, y_{N-1}^{(i,m)}]^{\mathrm{T}}$$

$$\mathbf{w}(i,m) = [w_0^{(i,m)}, \ldots, w_{N-1}^{(i,m)}]^{\mathrm{T}}.$$

The vectors $\mathbf{y}(i,m)$ can now be grouped for all the transmitter-receiver pairs to obtain the overall MIMO system model:

$$\underbrace{\begin{bmatrix} \mathbf{y}(1,1) \\ \mathbf{y}(2,1) \\ \vdots \\ \mathbf{y}(N_t,N_r) \end{bmatrix}}_{\mathbf{y}} = \underbrace{\begin{bmatrix} \mathbf{\Phi}(1,1) \\ \mathbf{\Phi}(2,1) \\ \vdots \\ \mathbf{\Phi}(N_t,N_r) \end{bmatrix}}_{\mathbf{\Phi}} \mathbf{d} + \underbrace{\begin{bmatrix} \mathbf{w}(1,1) \\ \mathbf{w}(2,1) \\ \vdots \\ \mathbf{w}(N_t,N_r) \end{bmatrix}}_{\mathbf{w}}.\tag{4.35}$$

The aggregate noise vector $\mathbf{w}$ is characterized by the covariance matrix

$$\boldsymbol{\Omega} = \begin{bmatrix} \boldsymbol{\Omega}(1) & \mathbf{0} & \ldots & \mathbf{0} \\ \mathbf{0} & \boldsymbol{\Omega}(2) & \ldots & \mathbf{0} \\ \mathbf{0} & \mathbf{0} & \ddots & \mathbf{0} \\ \mathbf{0} & \mathbf{0} & \ldots & \boldsymbol{\Omega}(N_r) \end{bmatrix}$$

with

$$\boldsymbol{\Omega}(m) = \begin{bmatrix} \boldsymbol{\Omega}^{(1,1)}(m) & \ldots & \boldsymbol{\Omega}^{(1,N_t)}(m) \\ \vdots & \ddots & \vdots \\ \boldsymbol{\Omega}^{(N_t,1)}(m) & \ldots & \boldsymbol{\Omega}^{(N_t,N_t)}(m) \end{bmatrix}$$

whose entries are defined by (4.33).

4.4.2.1 Maximum Likelihood Detector and Its Approximation

We pursue an ML solution by direct minimization of the original metric (4.25). To start with, we reformulate it as

$$\Lambda(\mathbf{d}) = \sum_{m=1}^{N_r} \int_0^T |v_m(t)|^2 dt - \sum_{m=1}^{N_r} 2\mathrm{Re}\left\{ \sum_{i=1}^{N_t} \sum_{k=0}^{N-1} d_k^{(i)^*} \underbrace{\int_0^T v_m(t) P_k^{(i,m)^*} dt}_{y_k^{(i,m)}} \right\}$$

$$+ \sum_{m=1}^{N_r} \sum_{i=1}^{N_t} \sum_{k=0}^{N-1} d_k^{(i)^*} \sum_{u=1}^{N_t} \sum_{l=0}^{N-1} \underbrace{\int_0^T P_l^{(u,m)} P_k^{(i,m)^*} dt \, d_l^{(u)}}_{\Phi_{k,l}^{(i,u)}(m)}. \quad (4.36)$$

In each resampling branch, since the Doppler scaling for the desired user is perfectly compensated – by choosing the resampling rate according to the Doppler scaling factor of this user – we have $\Phi_{k,l}^{(i,i)}(m) \approx \Phi_{k,k}^{(i,i)}(m)\delta(k-l)$. Hence, expression (4.36) can be simplified to

$$\Lambda(\mathbf{d}) \approx C_0 - \sum_{m=1}^{N_r} \sum_{k=0}^{N-1} 2\mathrm{Re}\left(\sum_{i=1}^{N_t} d_k^{(i)^*} y_k^{(i,m)} \right) + \sum_{m=1}^{N_r} \sum_{i=1}^{N_t} \sum_{k=0}^{N-1} d_k^{(i)^*} \sum_{\substack{u=1 \\ u\neq i}}^{N_t} \sum_{l=0}^{N-1} \Phi_{k,l}^{(i,u)}(m) d_l^{(u)} \quad (4.37)$$

with

$$C_0 = \sum_{m=1}^{N_r} \left(\int_0^T |v_m(t)|^2 dt + \sum_{i=1}^{N_t} \sum_{k=0}^{N-1} \left| \Phi_{k,k}^{(i,i)}(m) \right|^2 \right) \quad (4.38)$$

60

provided that the signal constellation chosen has a constant envelope, i.e., $|d_k^{(i)}|$ is a constant. Noticing that by definition in (4.32), $\Phi_{k,l}^{(i,u)}(m) = \left[\Phi_{l,k}^{(u,i)}(m)\right]^*$, the expression (4.37) can be further simplified to

$$
\begin{aligned}
\Lambda(\mathbf{d}) \quad \approx \quad & C_0 - \sum_{m=1}^{N_r} \sum_{k=0}^{N-1} 2\mathrm{Re} \left(\sum_{i=1}^{N_t} d_k^{(i)^*} y_k^{(i,m)} \right) \\
& + \sum_{m=1}^{N_r} \sum_{k=0}^{N-1} 2\mathrm{Re} \left(\sum_{i=1}^{N_t-1} d_k^{(i)^*} \sum_{l=0}^{N-1} \sum_{u=i+1}^{N_t} \Phi_{k,l}^{(i,u)}(m) d_l^{(u)} \right).
\end{aligned}
\quad (4.39)
$$

Similar to the single-user case as described in Section 4.3.2.1, it is computationally intractable to implement the ML detector by minimizing (4.39) for large Doppler scaling factor differences among different users. However, for smaller differences it is possible to pursue an approximate ML detection through the Viterbi algorithm since the coupling between different users (defined by $\Phi_{k,l}^{(N_t,i)}(m)$) can be reduced to such a level that only a manageable number of states are needed to account for these cross-user terms. While the approximate ML solution may be computationally affordable for two-user systems (with Doppler scaling factor differences), we point out that for more general cases, e.g. systems with more than two users, suboptimal detectors must be considered due to the resulting high complexity.

4.4.2.2   Linear Detectors

Given (4.35), we adopt two commonly used linear detectors, the LS detector and the MMSE detector. While conceptually simple, the implementation of these detectors requires some care since the matrices $\mathbf{H}$ and $\boldsymbol{\Phi}$ are both singular. The singularity problem is a direct consequence of the fact that different subsets of the signal vector $\mathbf{y}$ are generated from the *same* input signal. That is, the same noise process and multiuser signals are sampled multiple times to constitute the samples at each branch's output. As a result, strong dependence exists among different subsets of the sufficient statistics (that correspond to different branches), and loss of rank for both $\mathbf{H}$ and $\boldsymbol{\Phi}$ is expected.

The optimal solution can nonetheless be obtained through singular value decomposition (SVD) which removes the redundant coordinates in $\mathbf{y}$ [69]. Or, as an approximation, we can also deal with the ill-conditioned matrices by adding a scaled

identity matrix before the inversion is carried out. With this simpler approach, two regularized linear detectors are employed, one for the LS solution and one for the MMSE solution:

$$\tilde{\mathbf{d}}_{\mathrm{LS}} = \mathrm{Dec}\left(\left(\mathbf{\Phi}^{\mathrm{H}}\mathbf{\Phi} + \epsilon\mathbf{I}\right)^{-1}\mathbf{\Phi}^{\mathrm{H}}\mathbf{y}\right) \tag{4.40}$$

and

$$\tilde{\mathbf{d}}_{\mathrm{MMSE}} = \mathrm{Dec}\left(\mathbf{\Phi}^{\mathrm{H}}\left(\mathbf{\Phi}\mathbf{\Phi}^{\mathrm{H}} + \mathbf{\Omega} + \epsilon\mathbf{I}\right)^{-1}\mathbf{y}\right) \tag{4.41}$$

where the regularization factor ϵ is chosen as a small number with respect to the average of the non-zero eigenvalues of $\mathbf{\Phi}\mathbf{\Phi}^{\mathrm{H}}$.

4.4.2.3   Interference Cancelation

Interference-cancelation (IC) is considered as a means of improving the error rate performance of the system. An IC detector forms an estimate of the interference caused by one transmitter to the other, and subtracts this estimate from the desired signal prior to making symbol decisions. The estimation/detection process is performed iteratively, such that the nth iteration yields an interference estimate

$$\mathbf{I}_n(1,m) = \sum_{i=2}^{N_t} \mathbf{\Phi}^{(1,i)}(m)\tilde{\mathbf{d}}_{IC}^{(i)}(n-1)$$

which is used to form the symbol decisions as

$$\tilde{\mathbf{d}}_{IC}^{(1)}(n) = \mathrm{Dec}\left(\sum_{m=1}^{N_r}\left(\mathbf{y}(1,m) - \mathbf{I}_n(1,m)\right)\right). \tag{4.42}$$

The process is analogous for the other transmitters. The IC detector is initialized by symbol decisions that can be obtained using one of the linear detectors discussed previously. Note that after resampling, there is no self-ICI since we only consider Doppler shifts, and the only interference is due to the other transmitter. As will be illustrated through numerical examples, iterative IC detection offers a significant performance improvement over linear detection while maintaining a relatively low complexity.

4.5 Practical Considerations and Robustness of the Proposed Multiple Resampling Receiver Architectures

So far, we have assumed the CSI is known perfectly at the receiver to perform data detection. In practice, however, the CSI needs to be estimated and it is of interest to investigate how the multiple-resampling (MR) schemes perform with the estimated CSI. For this purpose, we adopt two sparse channel estimation schemes, namely a basis-pursuit scheme [70] and an orthogonal matching pursuit (OMP) scheme [66], which are particularly effective for underwater acoustic channels [51].

As pointed out in [71], a sparse estimator, be it BP-based or OMP-based, is subject to a basis mismatch problem when the parameters of the discrete paths are not in the dictionary. For instance, in our case, the path delay and/or Doppler rate of a particular path may occur somewhere between two consecutive dictionary entries instead of appearing very close to either one of them as is quite common for a real channel in the physical world. Due to the basis mismatch problem, there will always be an estimation error in the path delay and Doppler rate estimates, which is determined by the dictionary resolution and cannot be fully resolved by increasing the signal-to-noise ratio (SNR), that is, increasing the resolution may be helpful but cannot completely eradicate this problem. Actually, arbitrarily increasing the dictionary size is prohibited since the columns of a super-resolution dictionary may be highly correlated, rendering the sparse channel estimation problem to be ill-conditioned. Also, unnecessarily high resolution may make the complexity too high for implementation.

To overcome the basis mismatch problem, we propose to perform the channel estimation using a two-step approach. The first step is to use a standard sparse channel estimation technique (either BP or OMP) to obtain the initial estimates $\{\hat{h}_p, \hat{\tau}_p, \hat{a}_p\}_{p=0}^{P-1}$ of the channel parameters, where P is the number of the identified paths. The second step is to refine the initial estimates by employing a least squares (LS) criterion that aims at compensating for the estimation errors due to the basis mismatch. The resulting estimators are called the advanced BP estimator and the advanced OMP estimator,

respectively. In contrast, the estimators without the second step are called the basic BP estimator and the basic OMP estimator, respectively. For simplicity of illustration, dropping the transmitter-receiver pair indices, for each of the transmitter-receiver pairs, a full-blown approach for refinement is to explicitly estimate the basis-mismatch-induced errors, i.e. $(\Delta\hat{h}_p, \Delta\hat{\tau}_p, \Delta\hat{a}_p)$ for each of the identified paths such that the cost function

$$C(\Delta\hat{h}_p, \Delta\hat{\tau}_p, \Delta\hat{a}_p) = |\mathbf{y}_{\text{FFT}} - \hat{\mathbf{y}}_{\text{FFT}}(\Delta\hat{h}_p, \Delta\hat{\tau}_p, \Delta\hat{a}_p)|^2 \tag{4.43}$$

is minimized, where the vector $\mathbf{y}_{\text{FFT}}$ contains frequency domain samples of the FFT demodulator outputs, $\hat{\mathbf{y}}_{\text{FFT}}$ contains the predicted values of these samples, where

$$\hat{\mathbf{y}}_{\text{FFT}}(\Delta\hat{h}_p, \Delta\hat{\tau}_p, \Delta\hat{a}_p) = \sum_{p=0}^{P-1} \hat{\mathbf{H}}_p'(\Delta\hat{h}_p, \Delta\hat{\tau}_p, \Delta\hat{a}_p)\mathbf{d} \tag{4.44}$$

and

$$\hat{H}_p(k,l)' = (\hat{h}_p + \Delta\hat{h}_p)e^{-j2\pi f_l(\hat{\tau}_p + \Delta\hat{\tau}_p)}e^{-j\pi\beta'T}\text{sinc}(\pi\beta'T) \tag{4.45}$$

specifies the entries of the estimated channel matrix, and $\beta' = (k-l)\Delta f - (\hat{a}_p + \Delta\hat{a}_p)f_l$. To obtain $(\Delta\hat{h}_p, \Delta\hat{\tau}_p, \Delta\hat{a}_p)$, we need to take the partial derivative of $C(\Delta\hat{h}_p, \Delta\hat{\tau}_p, \Delta\hat{a}_p)$ with respect to $\Delta\hat{h}_p$, $\Delta\hat{\tau}_p$, and $\Delta\hat{a}_p$ individually and set these derivatives to zero. While the full-blown approach is cumbersome, we point out that since $\Delta\hat{a}_p f_l$ is very small, a simplified approach can be taken by approximating Equation (4.45) as

$$
\begin{aligned}
\hat{H}_p(k,l) &\approx (\hat{h}_p + \Delta\hat{h}_p)e^{-j2\pi f_l(\hat{\tau}_p + \Delta\hat{\tau}_p)}e^{-j\pi(\beta - \Delta\hat{a}_p f_l)T}\text{sinc}(\pi\beta T) \\
&= \underbrace{(\hat{h}_p + \Delta\hat{h}_p)e^{-j2\pi f_c\epsilon_p}}_{\hat{h}_p'}e^{-j2\pi\tilde{f}_l\epsilon_p}e^{-j\pi\beta T}\text{sinc}(\pi\beta T) \\
&= \tilde{h}_p'e^{-j2\pi\tilde{f}_l\epsilon_p}\hat{H}_p(k,l) \tag{4.46}
\end{aligned}
$$

where f_c is the center subcarrier frequency, $\tilde{f}_l = f_l - f_c$, $\epsilon_p = \Delta\hat{\tau}_p - \Delta\hat{a}_p T/2$, $\tilde{h}_p = \hat{h}_p'/\hat{h}_p$, $\beta = (k-l)\Delta f - \hat{a}_p f_l$ and

$$\hat{H}_p(k,l) = \hat{h}_p e^{-j2\pi f_l\hat{\tau}_p}e^{-j\pi\beta T}\text{sinc}(\pi\beta T) \tag{4.47}$$

is specified by the initial estimates $\{\hat{h}_p, \hat{\tau}_p, \hat{a}_p\}_{p=0}^{P-1}$. By this approximation, the unknown parameters in the LS problem reduces to $\{\hat{h}_p', \epsilon_p\}_{p=0}^{P-1}$. Since the partial derivative of the

64

cost function (4.43) with respect to ϵ_p is nonlinear, we pursue the solution of ϵ_p using a standard gradient descend algorithm (GDA) [72], with the gradient

$$\nabla_p^\epsilon = -2\text{Re}\left\{\sum_{k=0}^{N-1} e_k^* \frac{\partial \hat{y}_p(k)}{\partial \epsilon_p}\right\} \tag{4.48}$$

where, defining $\hat{y}_p(k) = \sum_{l=0}^{n-1} \bar{H}(k,l) d_l e^{-j2\pi \tilde{f}_l \epsilon_p}$ with $\bar{H}(k,l) = \tilde{h}_p' \hat{H}_p(k,l)$,

$$e_k = y_k - \sum_{p=0}^{P-1}\sum_{l=0}^{N-1} \bar{H}_p(k,l) d_l e^{-j2\pi \tilde{f}_l \epsilon_p} \tag{4.49}$$

is the prediction error of the kth frequency domain sample y_k and

$$\frac{\partial \hat{y}_p(k)}{\partial \epsilon_p} = \sum_{l=0}^{N-1} \hat{H}_p(k,l) d_l e^{-j2\pi \tilde{f}_l \epsilon_p}(-j2\pi \tilde{f}_l). \tag{4.50}$$

At each iteration of the GDA, the previous value of $\epsilon_p(n-1)$ is updated by

$$\epsilon_p(n) = \epsilon_p(n-1) - \nabla_p^\epsilon \cdot \Delta \tag{4.51}$$

where n is the iteration index and Δ is a tunable step size. Given the updated value of $\epsilon_p(n)$, the LS solution of $\hat{\mathbf{h}}_p' = [\hat{h}_0' \ \hat{h}_1' \ \dots \ \hat{h}_{P-1}']^{\text{T}}$ takes the standard form

$$\hat{\mathbf{h}}_p' = \left(\mathbf{U}^H \mathbf{U}\right)^{-1} \mathbf{U}^H \mathbf{y} \tag{4.52}$$

where $\mathbf{U} = [\mathbf{u}_0 \ \mathbf{u}_1 \ \dots \ \mathbf{u}_{P-1}]$ and

$$\mathbf{u}_p = \tilde{\mathbf{H}}_p(n)\mathbf{d} \tag{4.53}$$

where $\tilde{\mathbf{H}}_p(n) = \frac{\hat{H}_p(k,l)}{\tilde{h}_p} e^{-j2\pi \epsilon_p \tilde{f}_l}$ is the normalized channel matrix evaluated at the nth iteration. Since the initial estimates of the BP or OMP algorithm are refined using this gradient descend algorithm, the requirement for dictionary resolution of the proposed two-step approach can be greatly alleviated, resulting in a reduced computational cost and improved robustness of the sparse channel estimators.

4.6 Numerical Results

To verify the effectiveness of the proposed multiple-resampling designs, we present numerical results comparing their performance with those obtained by the conventional,
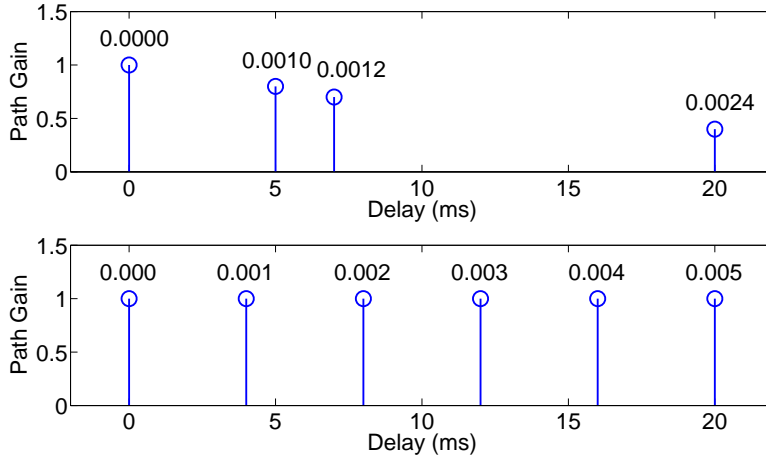
Figure 4.5: Multipath delay profile (labeled with path-specific Doppler rates) of Channel A (top plot) and Channel B (bottom plot).

single-resampling solutions. We start with simulated conditions, where the CSI is assumed to be known perfectly. We then give results for the imperfect CSI case, for which the channel estimates are obtained using compressive-sensing-based sparse channel estimators. Finally, we report results with the proposed detector using experimental data recorded in shallow water (100m) in the recent MACE10 and KAM08 experiments.

4.6.1 Simulation Results with Known CSI

4.6.1.1 Results for the Single-User case

Simulation results are reported for the case of a 512-subcarrier OFDM signal transmitted in the frequency band spanning 30 kHz to 34 kHz, i.e., with an intercarrier spacing of about 7.8 Hz. We consider two channels, which will be referred to as Channel A and Channel B, whose parameters are reported in Figure 4.5. For both channels the path with the strongest power is characterized by a zero Doppler rate. Equivalently, we can interpret the Doppler rates reported in the tables as the residual values after a single-resampling stage matched to the Doppler rate of the strongest path. Hence, no further resampling is needed for the single-resampling demodulator.

We first compare the magnitude of the ICI coefficients in the equivalent discrete channel model at the output of the demodulator for the case of single-resampling de-

modulation and for the case of multiple-resampling demodulation. Results are shown in Figure 4.6 for Channel A and in Figure 4.7 for Channel B; both cases referring to the noise-whitened channel model [73]. Note that the entries on the main diagonal can be interpreted as the subcarrier gains, while the other entries are the ICI terms (see (4.15)). In both figures, it is clear that the ICI power is much stronger for the single-resampling demodulation compared to the case of multiple-resampling demodulation. Namely, for Channel A the ICI power normalized with respect to the power of the terms on the main diagonal is $+0.5$ dB for the single-resampling demodulation and -7.9 dB for the multiple-resampling demodulation, which corresponds to an ICI-suppression gain of 8.4 dB provided by the proposed scheme. For Channel B, which is characterized by greater Doppler rate differences, the ICI-suppression gain is even more remarkable, i.e., about 15.2 dB.

We next compare the BER performance of the two systems for uncoded BPSK transmissions. The BERs characterizing various receivers are shown in Figure 4.8 as a function of the SNR, which is now defined as the ratio of the average power of $v(t)$ over the time interval $[0, T]$ to the average power of the in-band noise. For both demodulation schemes, two different detectors working on the noise-whitened channel model are compared: a symbol-by-symbol detector that neglects all the ICI terms and a more advanced detector that mitigates the ICI through a minimum mean squared error equalization [10, 42]. Maximum-likelihood detection is not considered since its complexity is proportional to the number of non-zero ICI terms, which makes it impractical to implement for the set of parameters adopted here.[3] The results demonstrate that the proposed demodulation scheme can provide impressive performance gains with respect to the single-resampling demodulation benchmark. Particularly, we notice that for the ICI-neglecting receivers, the BER performance difference is consistent with the ICI-suppression properties discussed in the comments of Figure 4.6 and Figure 4.7. For the ICI-aware receivers, we observe that the BER performance improvement is also noticeable. Notably, on Channel B, a simple symbol-by-symbol receiver combined with

---

[3]It is possible to implement Viterbi algorithm where the Doppler rate difference is smaller and the overall bandwidth is small. Examples of this implementation are omitted from this chapter.
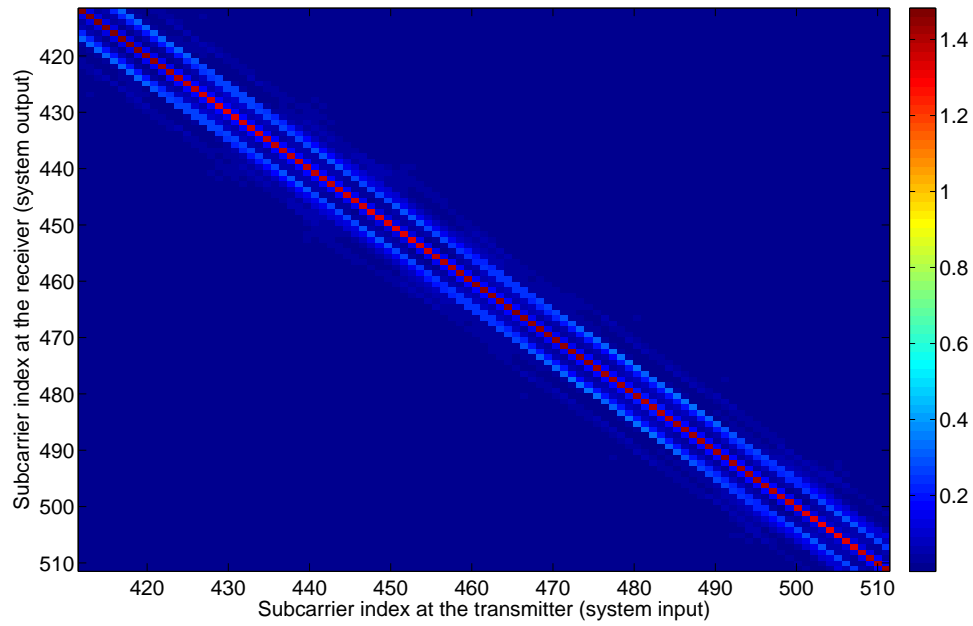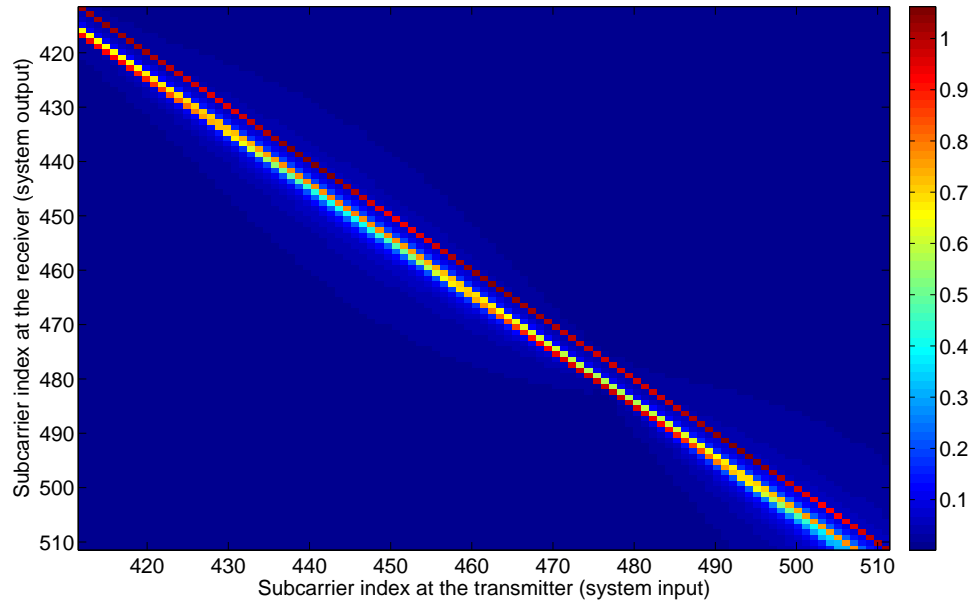
Figure 4.6: Magnitude of the ICI coefficients (see Equations (4.15) and (4.16)) obtained for Channel A after single-resampling demodulation (top plot) and multiple-resampling demodulation (bottom plot).
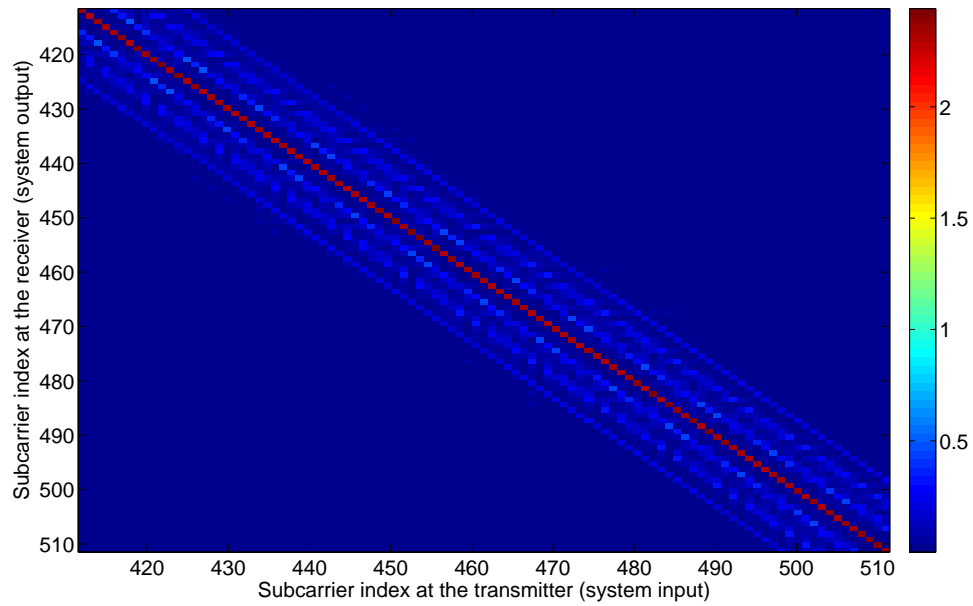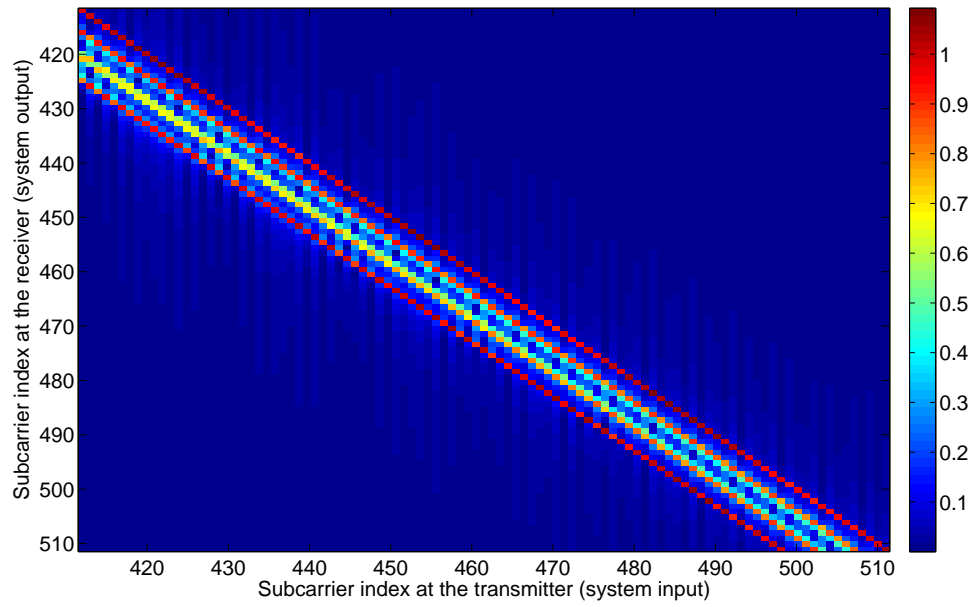
Figure 4.7: Magnitude of the ICI coefficients (see Equations (4.15) and (4.16)) obtained for Channel B after single-resampling demodulation (top plot) and multiple-resampling demodulation (bottom plot).
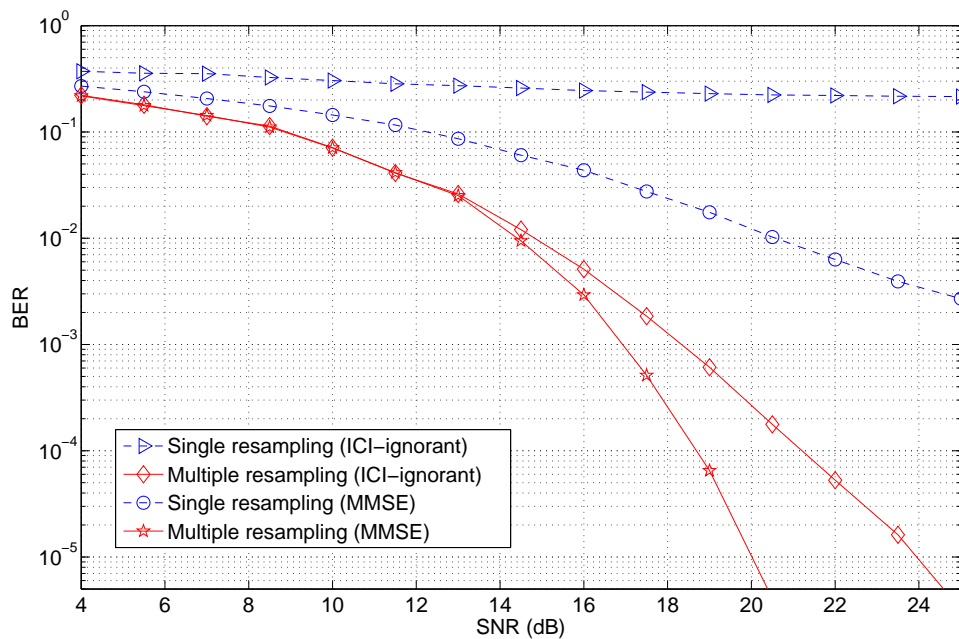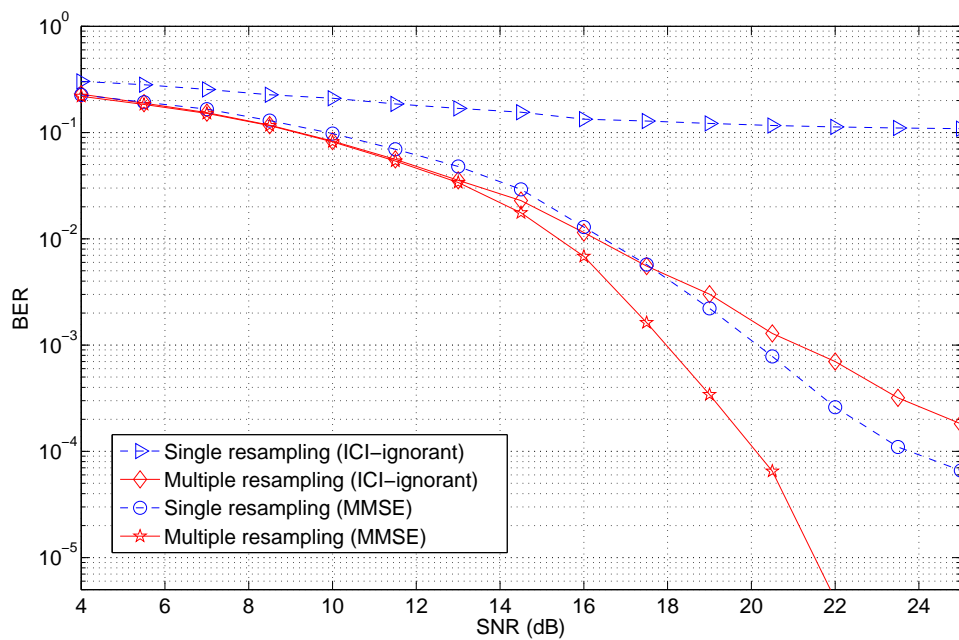
Figure 4.8: BER comparisons for Channel A (top plot) and Channel B (bottom plot).
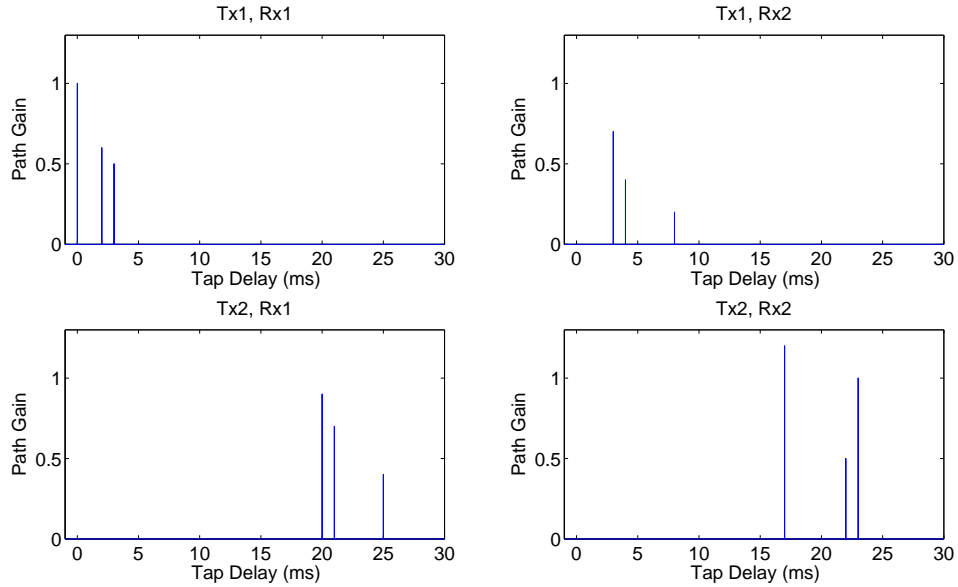
Figure 4.9: Multipath profile of the test channel.

the proposed demodulator outperforms the much more complex linear MMSE solution combined with the standard demodulator.

4.6.1.2   Results for the Multiuser Case

To verify the performance of the proposed multiuser receiver, a similar simulation study is conducted for the case of two transmitters sending messages to a centralized receiver. Figure 4.9 shows the multipath profile of the test channel. The Doppler scaling factors of the two transmitters are set to -1.0×10^{-3}, which corresponds to a relative speed of 1.5 m/s as the transmitter moves away from the receiver, and 1.2×10^{-3}, which corresponds to a relative speed of 1.8 m/s as the transmitter moves towards the receiver. Over this channel, two independent 1024-carrier OFDM signals with the same bandwidth are transmitted, occupying the frequency band 12 kHz to 20 kHz. The intercarrier spacing is 7.8 Hz, which corresponds to an OFDM block duration of 128 ms. A cyclic prefix of length 30 ms is used, resulting in a complete OFDM block of length 158 ms, which is shaped using a rectangular pulse.

Figure 4.10 shows the results of linear detection, focusing on the performance comparison between the multiple-resampling and the single-resampling front-end solu-

71
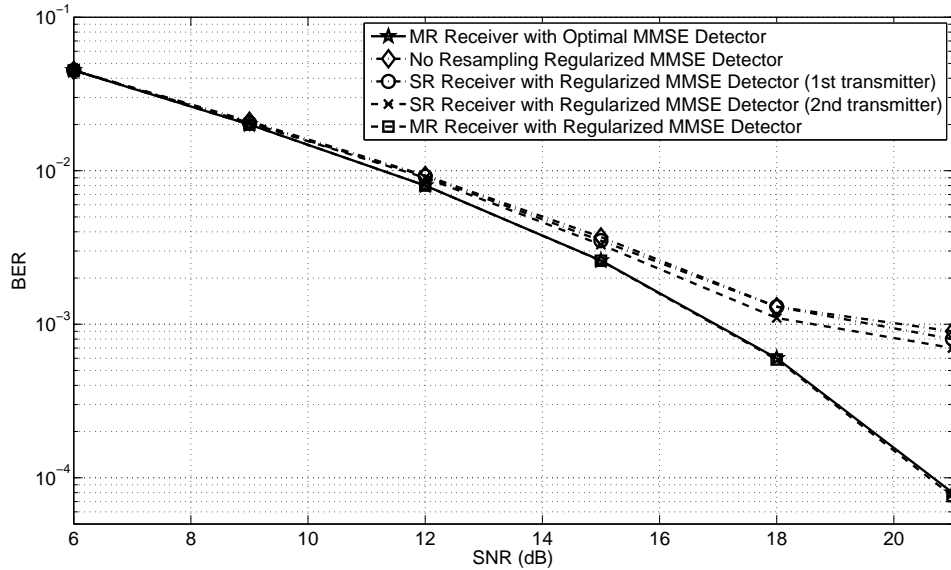
Figure 4.10: Performance of linear detection with multiple-resampling (MR) and single-resampling (SR) front-ends.

tions. Single-resampling includes resampling according to the Doppler scaling factor of the first transmitter and that of the second transmitter. Also included is the case with no resampling. Note that with the transmitters' Doppler scaling factors close in magnitude and opposite in sign, the receiver with no resampling can be interpreted as a special case of the single-resampling receiver [30], whose resampling rate is roughly the average of the two. The results of Figure 4.10 are obtained using the regularized linear MMSE detector with $\epsilon = 0.005$ (the average of the non-zero eigenvalues of $\mathbf{HH}^{\mathrm{H}}$ is 0.086). Included also are the results for the optimal, SVD-based linear MMSE detector. The regularized MMSE detector with multiple resampling performs very close to the optimal MMSE-based solution. More importantly, it offers a substantial performance gain over the single-resampling detectors.

Figure 4.11 shows the performance of various detectors proposed for the multiple-resampling receiver. Included are the regularized MMSE detector, the genie-aided IC detector, in which the interference estimate is obtained using known symbols from the interfering transmitter, and the decision-driven IC detector. The latter is initialized with regularized linear MMSE-algorithm-based decisions, and employs 3 or 9 itera-

72
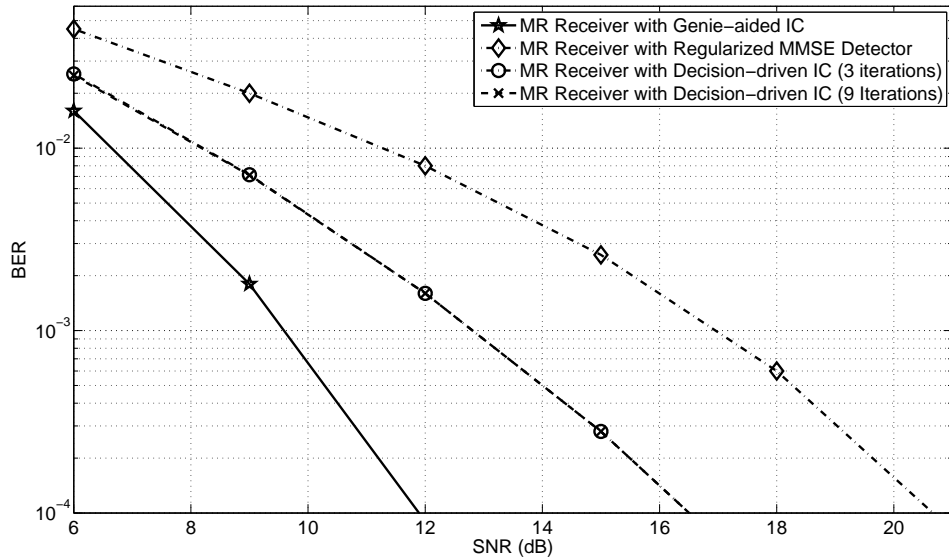
Figure 4.11: Performance of multiple resampling with linear and nonlinear detection schemes.

tions. Clearly, the IC detector provides performance that is closer to the genie-aided IC bound, outperforming the regularized MMSE detector by 3 dB or more. The IC detector takes only three iterations to converge, thus offering a good compromise between performance and complexity. The complexity of ML detection, even in an approximate form, is prohibitive for this test channel (at least 4096 states are required in the Viterbi algorithm), hence it is not employed.

4.6.2 Results on the Robustness of the Proposed Schemes

We have so far demonstrated the BER improvement with the proposed MR solutions when the CSI is available perfectly at the receiver. We now present numerical examples with estimated receiver CSI. Specifically, we focus on the above two-user cooperative MIMO case, where independent data streams are transmitted from nodes subject to user-specific Doppler rates. The multi-path structure and Doppler rate for each transmitter-receiver pair are the same as those in Section 4.6.1.2. Different from the previous section, these channel parameters are not known to the receiver. Instead, they are estimated with the sparse channel estimation algorithms described in Section 4.5.

73
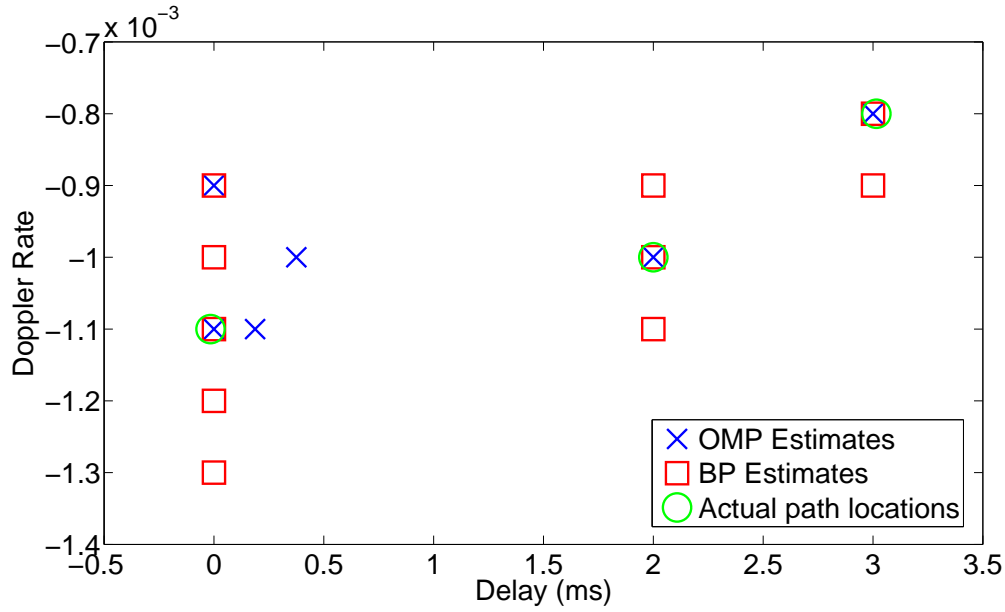
Figure 4.12: Path location estimates of the sparse channel estimators.

Here, for simplicity of demonstration, we assume that the channel parameters do not change for multiple consecutive OFDM blocks so that we can devote the first OFDM block for channel estimation and use the obtained channel estimates for the decoding of all of the following blocks. In reality, more practical schemes will be needed as will be discussed in Section 4.6.3 when we deal with results using real experimental data.

With the known transmitted symbols of the first OFDM block, we build a dictionary with a resolution of $62.5\mu s$ in the tap delay and 1×10^{-4} in the Doppler rate. The dictionary covers a delay spread of 20 ms and a Doppler rate variation of $\pm 5 \times 10^{-4}$ around the nominal values of each user, which is the typical range of (path-specific) Doppler rate variations in the MACE2010 and KAM08 experiments. Note that in order to mimic conditions of a real channel, the tap delay and/or the Doppler rate of each path of the simulated channels are shifted by a small random amount such that their actual values are not in the dictionary. Since the parameters of a real channel may be anywhere between two closest dictionary entries, we specify the injected random perturbations to be uniformly distributed, with a zero mean and a range of half of the dictionary resolution for both the tap delay and the Doppler rate.

With random perturbations being injected only to path delays (while Doppler rates are not perturbed, i.e., Doppler rates of the simulated channels are in the dictionary), Figure 4.12 shows the actual path locations of the transmitter-receiver pair (1,1) overlapped with the estimated path locations obtained by the basis pursuit and the orthogonal matching pursuit algorithms, respectively. As expected, due to the basis mismatch problem stated in Section 4.5, the number of the estimated paths is greater than the actual number for both algorithms. This is because the sparse channel estimators tend to not only identify the dictionary entry closest to an actual path location as a significant path but also include several nearby dictionary entries (around the actual one) in their path estimates. We observe that the BP-based estimator is subject to more false path locations than the OMP-based estimator. Thus, it is not surprising that as shown in Figures 4.13 (with random perturbation being injected only to Doppler rates) and Figure 4.14 (with only path delays being perturbed) the MR receiver using the OMP-based estimator offers a better BER performance than that using the BP-based estimator for both basic and advanced channel estimation configurations (see Section 4.5 for more details). In Figure 4.14, it is also evident that the performance of the MR receiver with the advanced OMP-based estimator is uniformly better than that with the basic OMP-based estimator. The BER performance of this advanced estimator is actually very close to that of the known CSI case, attesting to this approach's superior ability to compensate for the phase distortions due to the model mismatch. We do not observe such an improvement of using the advanced estimator for the BP-based estimators, which is due to the inferior quality of the initial channel estimates obtained by the basic BP estimator.

With the advanced OMP-based estimator, we now show comparisons of BER performance for the MR and the SR receivers under different model mismatch conditions. Particularly, in Figure 4.15, the model mismatch happens in the Doppler rate domain, i.e., the actual Doppler rates are not in the dictionary – recall that they are generated by shifting from the closest dictionary entry by a uniformly distributed random amount. For this condition, we observe a two-fold BER reduction at 21dB SNR when the MR receiver is adopted. Similar results with BER reduction up to six-fold are
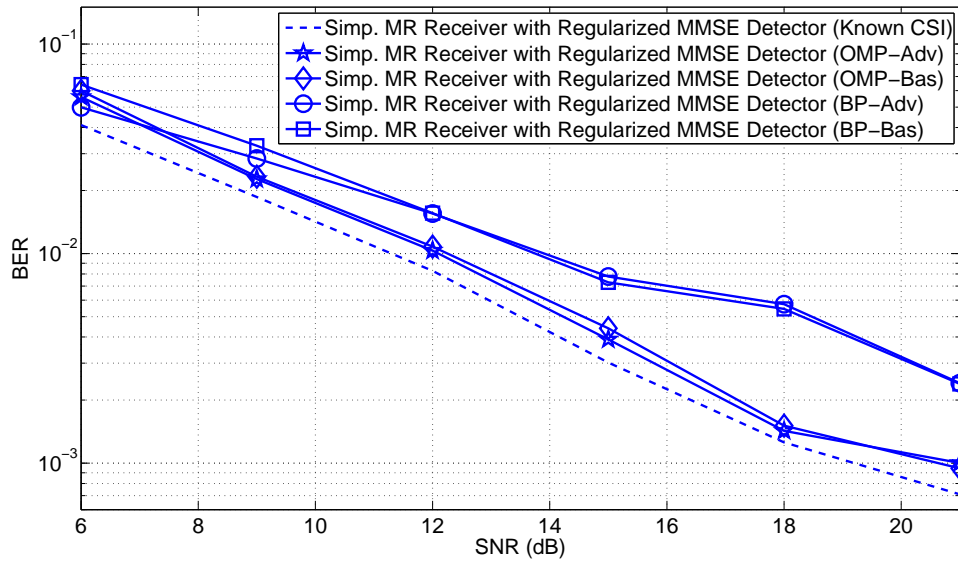
Figure 4.13: BER performance comparison between OMP and BP-based estimators with randomly perturbed Doppler rate.
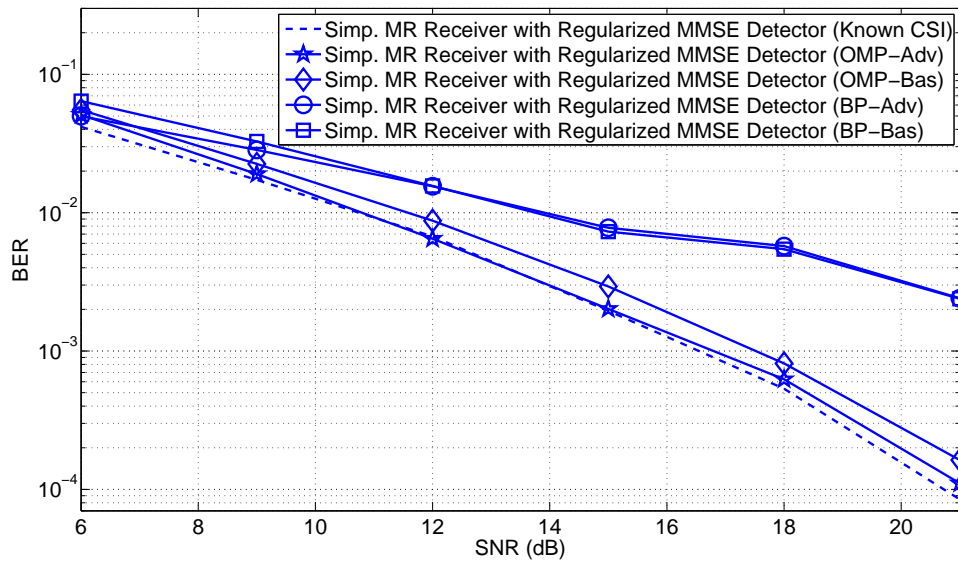
Figure 4.14: BER performance comparison between OMP and BP-based estimators when the path delay is not in the dictionary.
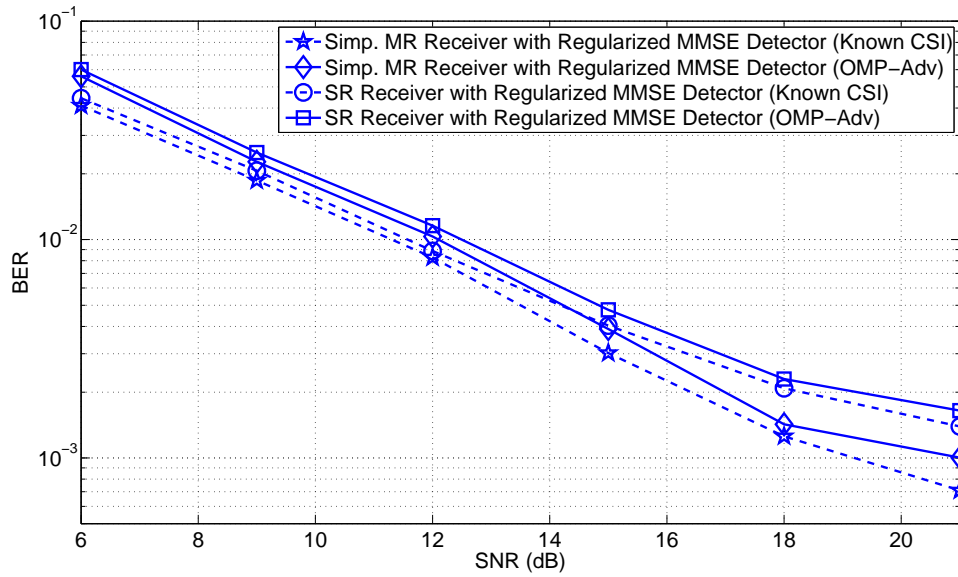
Figure 4.15: BER performance comparison between MR and SR receivers when the Doppler rate is not in the dictionary.
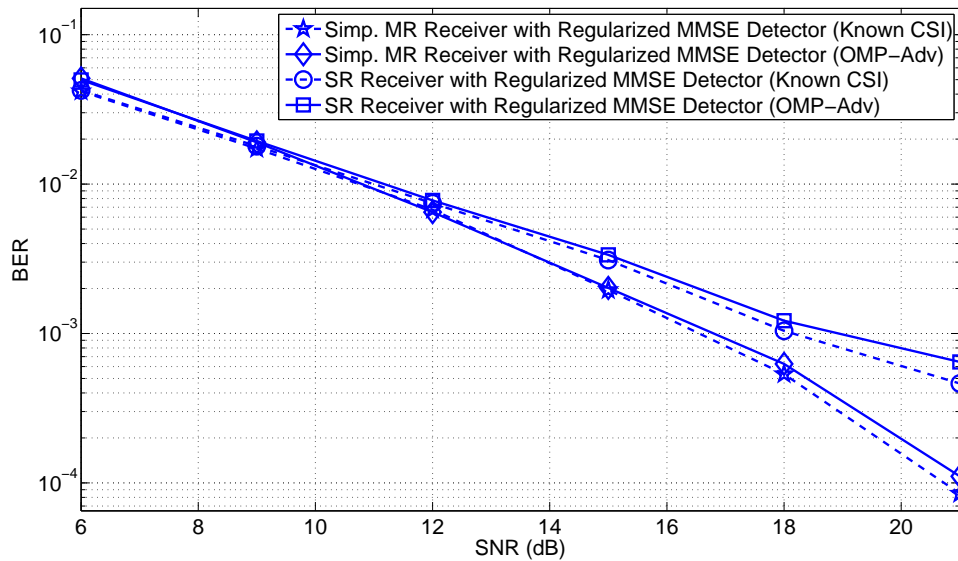
Figure 4.16: BER performance comparison between MR and SR receivers when path delay is not in the dictionary.
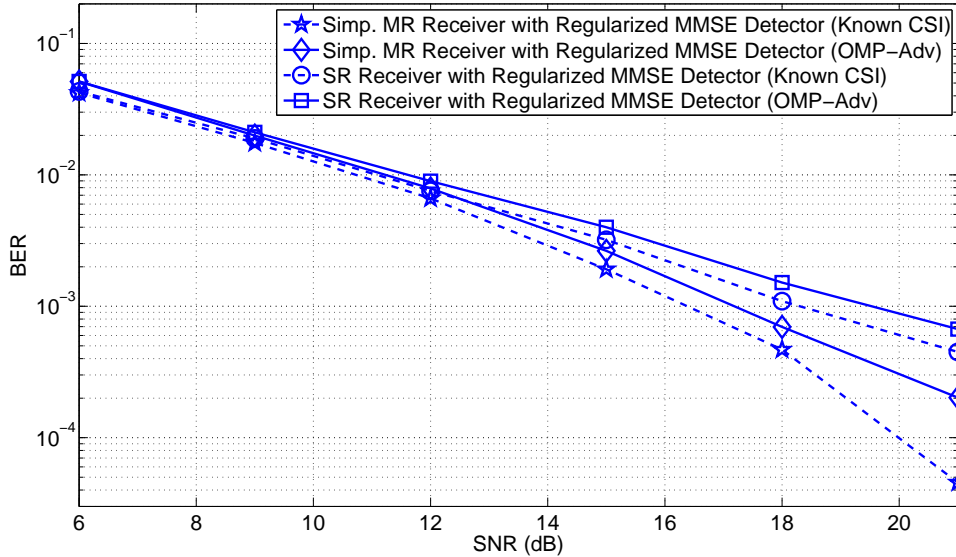
Figure 4.17: BER performance comparison between MR and SR receivers when the Doppler rate and path delay are not in the dictionary.

observed when the model mismatch happens in the tap delay domain (Figure 4.16) and in both domains (Figure 4.17). Particularly, with model mismatch in the tap delays, the error rate reduction is about six-fold at 21dB SNR, while that for the case of mismatched Doppler rates and tap delays (both of them are perturbed with realizations of uniformly distributed random variables with a range of half of the dictionary resolution) is about three-fold at the same SNR level. The amount of BER reduction depends on the resulting channel realizations in different model mismatch conditions.

4.6.3 Experimental Results

To verify the effectiveness of the proposed MR receiver designs with experimental data, we use data recorded in two recent shallow water (100 m water depth) acoustic communications experiments, namely the 2010 MIMO acoustic communications experiment (MACE10) [67], and the Kauai Acomms MURI 2008 (KAM08) experiment conducted in June 2008 – off the western coast of Kauai, Hawaii [2].

4.6.3.1   Results Obtained with the MACE10 Data

During the MACE10 experiment, one mobile source (towed at a nominal speed of about 1 m/s) and four fixed receivers are used. The source is equipped with four ITC 1007 spherical transducers, submerged at a depth of about $30 - 60$ m. The transducer spacings are 48 cm between the first and the second one, 42 cm between the second and the third one, and 48 cm between the last two. Two moored receivers are used, one with 24 elements and the other with 12. The inter-element spacings are 5 cm for the former and 12 cm for the latter. The sampling rate is $39,026.5$ Hz for both. The other two receivers, both with four receiving elements, are suspended from small surface buoys. The inter-element spacing and sampling rate are 20 cm and 50 kHz, respectively, for both. We particularly focus on data recorded at the two suspended receivers when the source was about 1.3 km and 4.3 km from the two receivers, respectively, due to relatively high receiver SNRs. The corresponding transmitted signals are 15 blocks of 512-subcarrier CP-OFDM signals employing QPSK modulation. The sampling rate before digital-to-analog conversion (ADC) is $F_s = 10^7/256 = 39.0625$ kHz, and the bandwidth is $B = F_s/8 \approx 5$ kHz, resulting in a subcarrier spacing of about 10 Hz. The lowest frequency subcarrier is located at $f_0 = 10.580$ kHz. A guard interval of 16 ms is inserted between consecutive blocks to prevent inter-block interference (IBI).

Note that the existing experimental setup supports transmission from a single source to multiple receivers. To mimic the conditions for multiuser transmissions, where independent streams are emitted from multiple spatially separated nodes, as shown in Figure 4.18 we use received signals that correspond to two consecutive blocks recorded at the two receivers and sum them up to form a superimposed signal – effectively each block of the superimposed signal corresponds to 2048 transmitted bits. The superimposed signal thus contains arrivals for two independent transmitted streams with independent multipath structures and different nominal Doppler rates. The latter is due to different relative speeds and directions between the transmitter and the receiver. We note that the difference between the nominal Doppler rates is in the order of 5×10^{-4}, which is
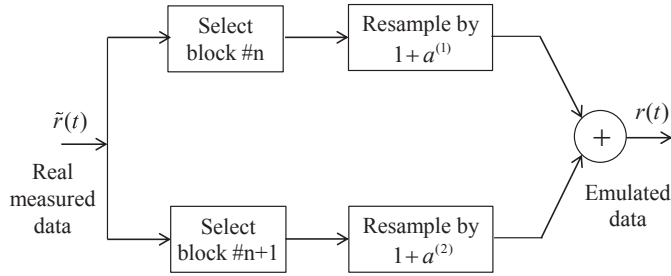
Figure 4.18: Emulation of data received from two transmitters with different Doppler rates using real measured data.

a result of a low nominal speed (1 m/s) of the moving source. To mimic scenarios with larger nominal Doppler rate differences, we resample the received signal from different receivers at different rates before summing them up. Effectively, we introduce additional Doppler scaling to the received signal and as a result, we are able to control the nominal Doppler rate difference in the received signal. As examples, we generate superimposed signals with 4.4×10^{-3} and 8.8×10^{-3} Doppler rate differences – the Doppler rates for the two users are the same in magnitude but opposite in sign. The equivalent speed differences are 6.6 m/s and 13.2 m/s respectively.

We implement the SR and MR receiver designs with the OMP-based channel estimator as in Section 4.6.2. Since the average nominal Doppler rates of the two users is zero, the optimal SR receiver performs no resampling. For the MR receiver, a full-blown implementation requires multiple resampling branches for each user as stated in Appendix A. However, we observe that the path-specific Doppler rate difference is in the order of 2×10^{-4} for each user. Therefore, we adopt a simplified MR receiver implementation with a single resampling branch for each user. The resampling rate is set according to the nominal Doppler rate of that user. The receivers are implemented in a decision-directed fashion. That is, we start the data detection from channel estimates obtained with only pilots signals – the pilot assignment is the similar to that in [51]. The receivers then use the channel estimates to perform the regularized MMSE detection (Section 4.3.2.2), whose tentative decisions are then used for the IC detection described in Section 4.4.2.3. The detected symbols are then used together with the pilot signals for the next round of iterative channel estimation and detection.

In Figure 4.19, we show the BER performance comparison between SR and MR receivers with a Doppler rate difference of 4.4×10^{-3} where the BER results refer to those obtained at the fifth iteration in a 2×4 system configuration, whereas in Figure 4.20 the BER results are obtained at the third iteration with a Doppler rate difference of 8.8×10^{-3}. On average, the MR receiver offers a two-fold BER reduction over the SR receiver for both Doppler rate differences. We point out that using detected symbols for channel estimation in the decision-directed mode may subject the overall system performance to degradation due to possible error propagation. A solution may be to involve explicit channel coding in the loop, where decoded symbols are fed back for the channel estimation. As a preliminary study, we envision a coded system codewords spanning multiple OFDM frames. Even with a relatively high rate low density parity check (LDPC) code (e.g. >0.67), we can bring the uncoded BER of the order of 10% (obtained using channel estimates based solely on pilot symbols) down to the order of 1% [22], with random decoded error locations. In Figures 4.21 and 4.22, we show the BER comparisons of MR and SR receivers assuming coded symbols (with 1% coded BER) used for channel estimation. We observe a two-fold and a three-fold BER reduction for Doppler rate differences of 4.4×10^{-3} and 8.8×10^{-3}, respectively, which implies that an additional performance advantage of the MR receiver is possible when channel coding is involved. In this case, the BER reduction by the MR receiver design tends to be more enhanced as the Doppler rate difference increases.

4.6.3.2   Results Obtained with the KAM08 Data

Let us now consider communication data collected in the KAM08 experiment. Similar to Section 4.6.3.1, we focus on the results for a 512-carrier OFDM system, where a BPSK modulation is used. The signal has a frequency band spanning 12 kHz to 20 kHz and a cyclic prefix of 20 ms, which implies a word duration of 276 ms. The experimental data is collected in the presence of motion between the transmitter and the receiver. Namely, the transmitter is submerged at a depth spanning 20 m to 50 m, depending on the specific experiment, and is towed at a nominal speed of 3 knots (i.e., about 1.54 m/s), while the receiver is a 16-element vertical array. The sampling rate
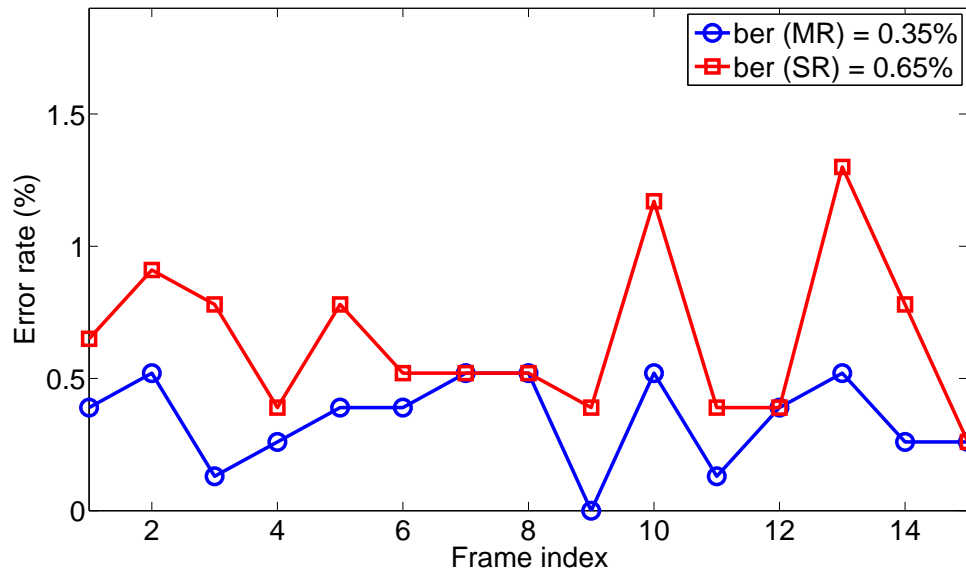
Figure 4.19: BER performance comparison between MR and SR receivers with decision-directed mode ($\Delta a = 4.4 \times 10^{-3}$).
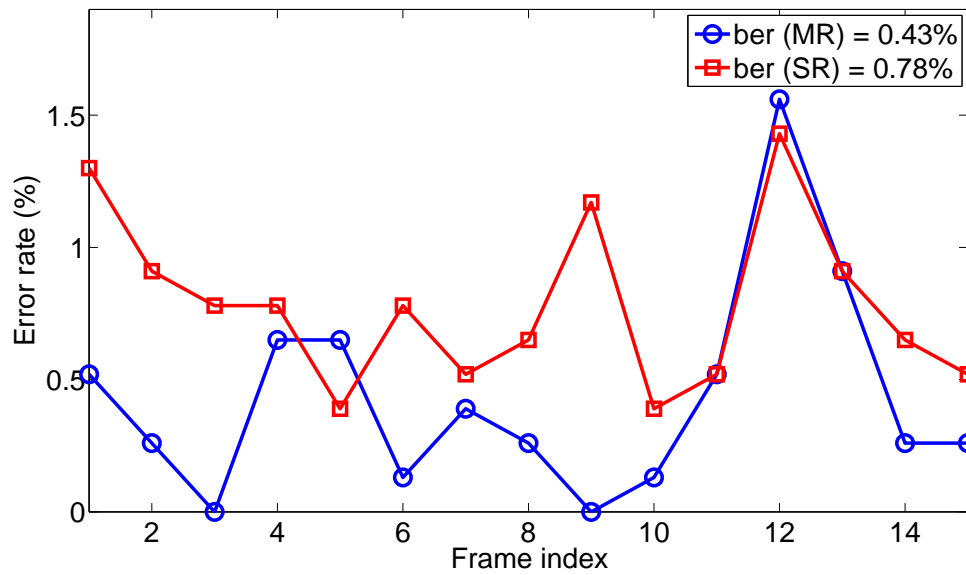
Figure 4.20: BER performance comparison between MR and SR receivers with decision-directed mode ($\Delta a = 8.8 \times 10^{-3}$).
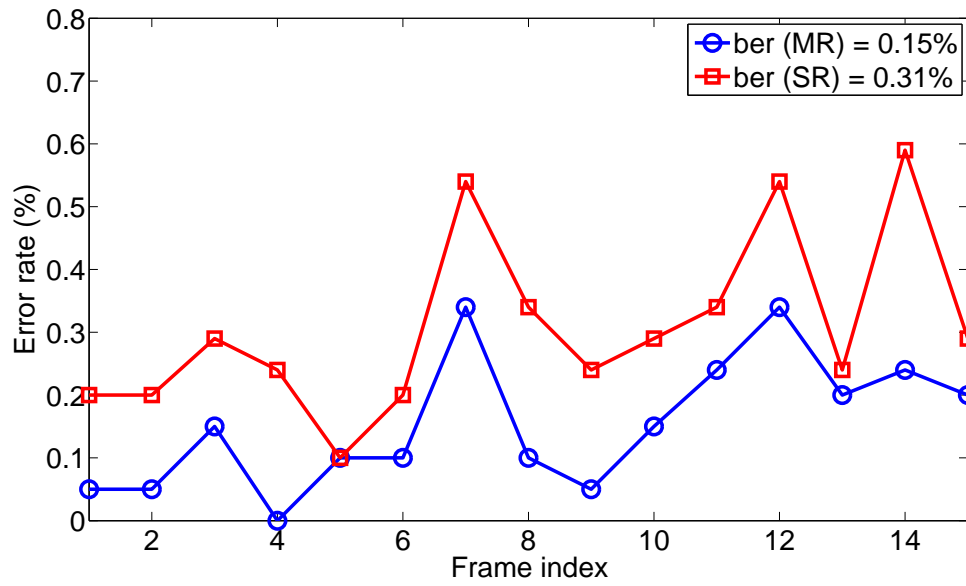
Figure 4.21: BER performance comparison between MR and SR receivers with channel coding ($\Delta a = 4.4 \times 10^{-3}$).
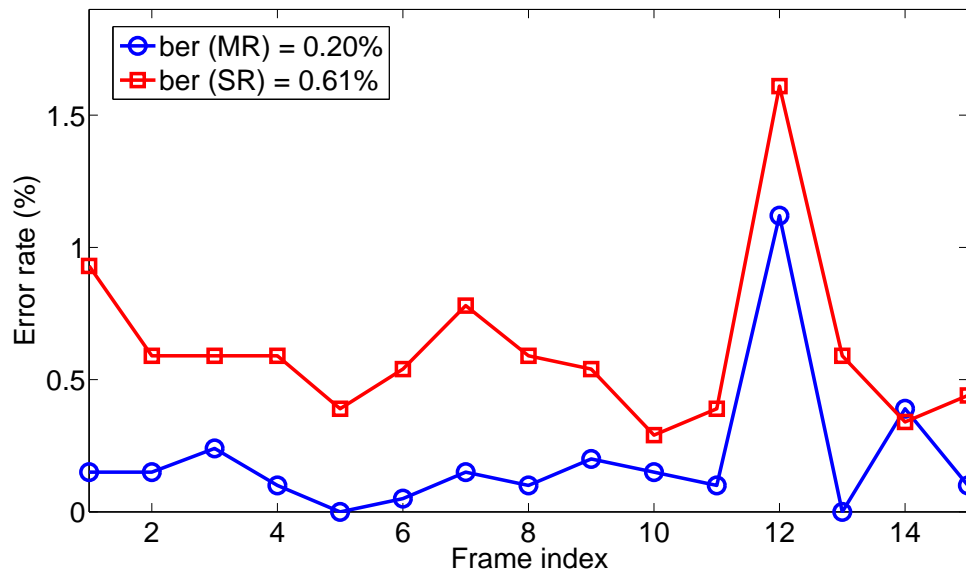
Figure 4.22: BER performance comparison between MR and SR receivers with channel coding ($\Delta a = 8.8 \times 10^{-3}$).
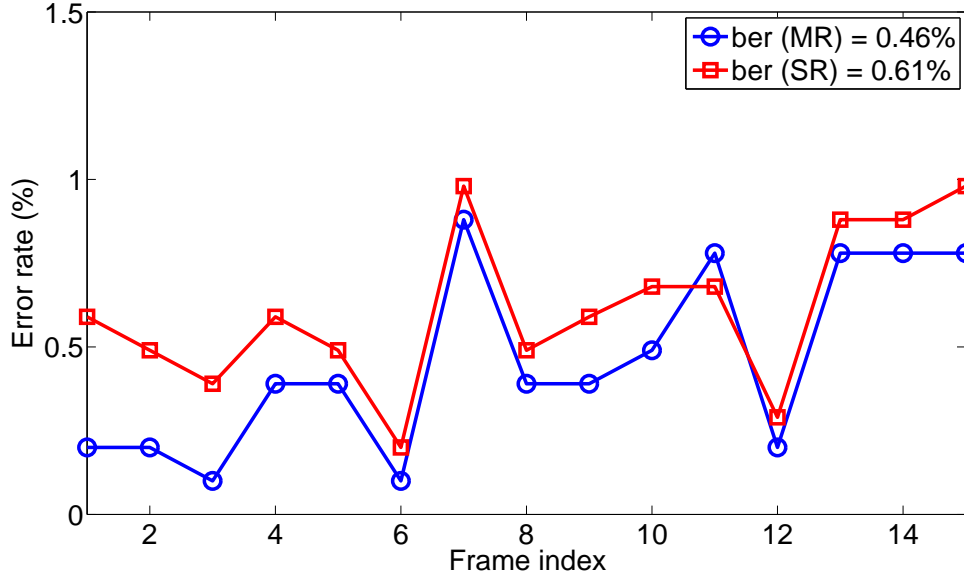
Figure 4.23: BER performance comparison between MR and SR receivers with channel coding ($\Delta a = 4.4 \times 10^{-3}$).

at the receiver is 50 kHz. The inter-element spacing is 3.75 m, with the top element deployed at a nominal depth of 42.25 m. Particularly, we consider the case when the transmitter/receiver separation is approximately 2 km, and the towing ship is moving towards the fixed receiver, with the transmitting transducer being about 25 m below the sea surface.

Adopting the same approach as described in Section 4.6.3.1, we pre-distort the received signals to form composite signals that have controlled Doppler rate differences. We notice that compared to the MACE10 experiment, the received signals are subject to a lower SNR and therefore an inferior channel estimation quality. To make up the performance loss, we use 2×6 systems instead of the 2×4 systems in Section 4.6.3.1. Adopting coded symbols of 1% coded BER for channel estimation, we see a similar tendency of the MR receivers to perform better than the SR receivers As shown in Figure 4.23. However, due to the inaccurate channel estimates, the performance advantage of the MR receivers is not as pronounced as the case of the results of MACE experiment.

4.7 Chapter Summary

In this chapter, we have investigated novel receiver front-end designs for UWA channels with path/user specific Doppler distortions. In particular, we focused on OFDM transmissions in the context of single-user SISO and multiuser MIMO scenarios. In the latter case, a centralized receiver was considered (with collocated receiver elements) communicating with multiple distributed users, which transmit independent data streams simultaneously in the same frequency band. We pointed out the inadequacy of standard single-resampling designs and proposed a set of new designs based on multiple-resampling front ends. For single-user systems, a resampling branch is needed for each cluster of arrivals that share a common Doppler rate, whereas for multiuser MIMO systems each branch corresponds to the Doppler rate of a particular user, provided that path-specific Doppler for each user can be neglected. Via extensive simulations and (emulated) experimental data studies, we have demonstrated that the multiple resampling designs offer significant performance gains in terms of BER and ICI power reduction compared to the single-resampling designs.

Chapter 5

MULTIPLE RESAMPLING RECEIVERS FOR ORTHOGONAL FREQUENCY

DIVISION MULTIPLE ACCESS SYSTEMS

In Chapter 4, we have investigated OFDM receiver designs for UWA channels with path and/or user-specific Doppler distortions. A family of OFDM receivers have been invented, where multiple-resampling branches are involved, each tasked with the Doppler distortion of a particular group of signal arrivals, which share a common Doppler rate. The effectiveness of this novel design have been verified in both single-user and cooperative multiuser settings, with simulations as well as emulations based on real data recorded in the KAM08 and the recent MACE 2010 experiments.

In this chapter, we investigate the possibility of using orthogonal frequency division multiple access (OFDMA) for design of efficient underwater acoustic networks, where a large number of communication nodes may be present. Similar to the case of UWA OFDM systems, a major challenge for the OFDMA-based UWA communication systems is the Doppler-induced frequency scaling, which may cause severe intercarrier interference (ICI), and depending on the particular user subcarrier assignment, can introduce a destructive level of interuser interference (IUI). As described in Chapters 3 and 4, the commonly-adopted Doppler mitigation technique of OFDM based transmissions uses a single-resampling stage, which, while effective in peer-to-peer communication scenarios, might be suboptimal and may fail in a large multiuser system, where users can experience significantly different Doppler scaling effects.

We develop a unique OFDMA receiver front end, which enables compensation of each user-specific Doppler by means of multiple resampling branches. With this new design, we investigate two subcarrier allocation schemes, namely the contiguous carrier assignment, and the interleaved carrier assignment schemes. We demonstrate the effectiveness of multiple-resampling designs and study the differences between the two assignment schemes both via simulations as well as emulations obtained by real data recorded in the recent MACE 10 Experiment.

The chapter is organized as follows: Section 5.1 provides the background material for UWA multiuser systems and summarizes the proposed UWA-OFDMA system design. In Section 5.2, we describe the UWA-OFDMA system model. In Section 5.3, we present the proposed receiver front-end design. In Sections 5.4 and 5.5, we consider practical detection and decoding schemes which exploit the benefits of the front-end structure proposed, and the required channel estimation algorithm, respectively. In Section 5.6, we present numerical results comparing different receivers and subcarrier assignment schemes. Finally, we conclude the chapter in Section 5.7.

5.1   Introduction

Research in underwater acoustic sensor networks, where a number of underwater sensors and vehicles are coordinated to perform collaborative tasks, has seen significant growth in recent years [15]. The most common applications include undersea explorations, environmental monitoring, disaster prevention, and distributed tactical surveillance [15]. Facing significant challenges posed by the underwater acoustic (UWA) channels, such as large latencies, long multipath delay spreads, fast channel variations, and very limited bandwidths [1], these networks need carefully designed multiple access schemes. For UWA networks, while time division multiple access (TDMA) [18] and code division multiple access (CDMA) [19] have been investigated, there are no results on orthogonal frequency division multiple access (OFDMA), which is the topic of this chapter. OFDMA divides the useful frequency band into a set of orthogonal subcarriers, which are shared among different users to allow for multiple access. The major advantages of OFDMA systems include robustness to large multipath delay spreads, high spectral efficiencies, and the ability to exploit the multiuser and/or multipath diversity [34]. However, intercarrier inference (ICI) and interuser inference (IUI) – arising from motion-induced Doppler shift – pose significant challenges. While various Doppler shift compensation schemes are available for UWA OFDM systems [5, 66], there is no practical scheme tailored for UWA OFDMA systems. Most existing Doppler mitigation techniques are

designed for narrow-band radio terrestrial links [33], and hence may not be suitable for wide-band UWA links [1]. The commonly-adopted approach for Doppler mitigation of UWA OFDM systems employs a single resampling stage to compensate for the *common* Doppler scaling factor [66]. However, this design does not account for user-specific Doppler distortions, which arise as a result of spatially separated users moving at speeds and in directions that are significantly different from each other.

To solve this problem, we extend our results of the OFDM receiver designs invented in Chapter 4, and propose a multiple resampling (MR) OFDMA receiver front end, where each resampling branch is tasked with addressing the Doppler scaling effect of a particular user [74]. Different from the OFDM receiver developed in the cooperative multiuser settings, where frequency domain samples on subcarriers of the entire frequency band are generated for each user, this OFDMA-specific multiple-resampling front end extracts only the frequency domain samples corresponding to the subset of subcarriers allocated to each user. The new front-end design keeps the sufficient statistics for post data detection and decoding. Coupled with this, we introduce an interference cancelation (IC) based detection algorithm, initialized by a multiuser minimum mean square error (MMSE) detector. Furthermore, channel coding is incorporated into the system via the use of low density parity check (LDPC) codes in order to exploit the multipath diversity provided by the channel. To investigate the impact of different subcarrier assignments on the multipath diversity, we experiment with two schemes: the first one is a contiguous assignment scheme (hereafter referred to as Scheme 1), which allocates a contiguous block of subcarriers to one user; while the second one is an interleaved subcarrier assignment (hereafter referred to as Scheme 2), which allocates subcarriers periodically to each user. To enable the overall receiver design, we develop a specialized OFDMA channel estimator which does not depend on any particular pilot and/or subcarrier assignment scheme. To verify the effectiveness of our receiver design, we use simulations and emulations using data recorded in the MACE 2010 Experiment.

5.2   System Model

We consider a coded OFDMA system with N_u spatially separated users and a centralized receiver with N_r-receive elements. In total, there are N subcarriers shared by all the users, where each user is allocated a non-overlapping subset of size K to transmit its data and/or pilot symbols. The symbols are obtained by mapping a sequence of channel-coded and interleaved bits to a suitable complex-valued constellation, such as phase-shift keying (PSK) or quadrature amplitude modulation (QAM). Specifically, we adopt LDPC coding, which spreads each codeword across M OFDMA blocks [75].

The transmitted signal for each user is given by

$$s_u(t) = \mathrm{Re}\left\{ \sum_{k \in \mathcal{S}_u} d_k e^{j2\pi f_k t} \right\}, \quad t \in \{-T_g, T\} \tag{5.1}$$

where $\mathcal{S}_u$ is the set containing subcarrier indices belonging to the u-th user, d_k is the symbol transmitted on the k-th subcarrier, $f_k = f_0 + k/T$ is the frequency of the k-th subcarrier (f_0 is the center carrier frequency), $1/T$ is the spacing between consecutive subcarriers, and T_g is the duration of the cyclic prefix [65]. $\mathcal{S}_u$ depends on the particular subcarrier assignment scheme. Assuming no transmitter side channel state information (CSI), for Scheme 1, $\mathcal{S}_u$ includes a block of adjacent subcarriers that occupy one of the N_u contiguous frequency subbands. For Scheme 2, however, $\mathcal{S}_u$ is comprised of subcarriers that are separated from each other by N_u subcarriers and are spread across the entire band.

The signal arriving at the m-th receiver, after down-shifting by f_0, is given by

$$v_m(t) = \sum_{u=1}^{N_u} \sum_{k \in \mathcal{S}_u} d_k P_k^m(t) + w_m(t) \tag{5.2}$$

where $w_m(t)$ is the additive white Gaussian noise (AWGN) with power spectral density (PSD) N_0, and

$$P_k^m(t) = \sum_{p=0}^{N_p^{u,m}-1} \alpha_k^{m,p} e^{j2\pi a_u f_0 t} e^{j2\pi(t+a_u t)k/T} R\left(t + a_u t - \tau_u^{m,p}\right), \forall k \in \mathcal{S}_u \tag{5.3}$$

where $N_p^{u,m}$ is the number of paths for the (u, m)-th transmitter-receiver pair, $R(t)$ is a rectangular pulse spanning the interval $t \in [-T_g, T]$, $\alpha_k^{m,p} = h_u^{m,p} e^{-j2\pi f_k \tau_u^{m,p}}$, $\forall k \in \mathcal{S}_u$,

89

and a_u, $h_u^{m,p}$, and $\tau_u^{m,p}$ are each individual path's Doppler scaling factor, path gain, and path delay, respectively. Note that the term $P_k^m(t)$ implicitly depends on the user index as well (through the subcarrier index k).

5.3   OFDMA Receiver Front End

Following a similar procedure employed in the case of OFDM systems described in Chapter 4, we aim to identify a set of frequency domain samples for the joint maximum likelihood (ML) detection of the N_u users in a OFDMA system. The result of this effort is a set of matched-filter outputs obtained through correlating $v_m(t)$ with pulses $P_k^m(t)$, i.e.,

$$y_k^m = \int_{-\infty}^{\infty} v_m(t) P_k^m(t)^* dt, \ \ k = 0, 1, \ldots, N - 1. \tag{5.4}$$

Focusing on the subset $\{y_k^m\}_{k \in \mathcal{S}_u}$, it can be shown that these samples can be obtained by an FFT operation [65])

$$y_k^m \approx \alpha_k^{m*} \int_0^T v_{u,m}\left(\frac{t}{1 + a_u}\right) e^{-j2\pi kt/T} dt, \ \ \forall k \in \mathcal{S}_u \tag{5.5}$$

where $\alpha_k^m = \sum_{p=0}^{N_p^{u,m}-1} \frac{\alpha_k^{m,p}}{1+a_u}$, $\forall k \in \mathcal{S}_u$ and $v_{u,m}(t) = v_m(t)e^{-j2\pi a_u f_0 t}$ is the frequency shifted version of $v_m(t)$. Note that Equation (5.5) is very similar to Equation (4.30) in Chapter 4 for the case of multiuser MIMO OFDM systems. The major difference here is that for the OFDMA system, each user is allocated a subset of the entire frequency band, and thus the frequency domain samples (5.5) include only a subset of the subcarriers corresponding the user's resource allocation.

Figure 5.1 illustrates the proposed receiver front end (assuming Scheme 1 is used). There are N_u resampling branches, each branch compensating for the corresponding user's Doppler shift in two steps: the first step involves compensation of the common Doppler frequency shift $a_u f_0$, and the second step deals with the residual shifts by resampling according to the user's Doppler scaling factor a_u. Note that after the FFT demodulation, each branch extracts only the K samples corresponding to each user's subcarrier assignment.
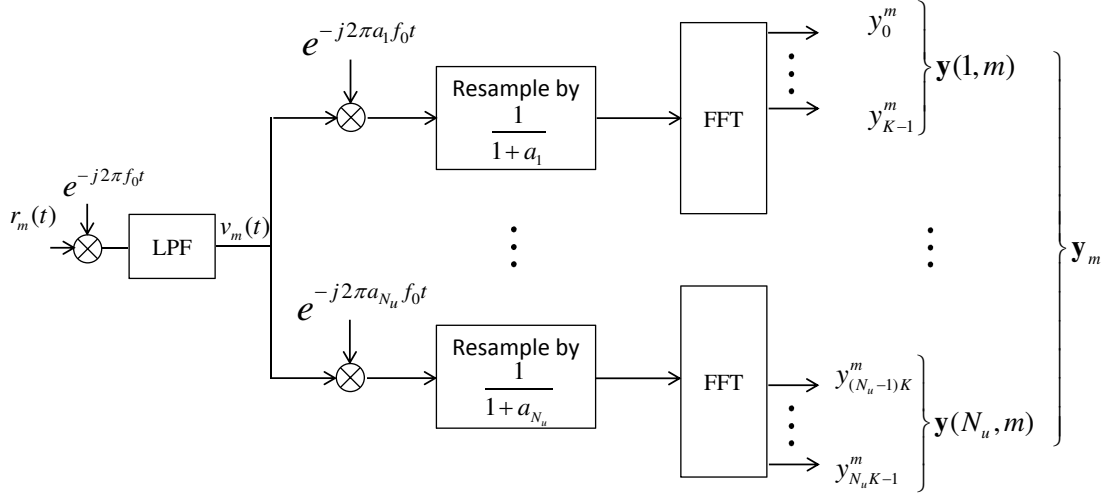
Figure 5.1: The OFDMA MR front end for the mth receiving element.

5.4 Data Detection and Channel Decoding

While ML detection is optimal in terms of error probability, its computational cost may be too high. To strike a balance between performance and complexity, we devise an interference-cancelation (IC)-based detection and decoding scheme that takes advantage of the proposed front-end design for both the uncoded case and the coded case.

5.4.1 Interference Cancelation Based Data Detection

We define $\mathbf{y} = \left[\mathbf{y}_1^{\mathrm{T}}, \ldots, \mathbf{y}_{N_r}^{\mathrm{T}}\right]^{\mathrm{T}}$, where $\mathbf{y}_m = \left[y_0^m, y_1^m, \ldots, y_{N-1}^m\right]^{\mathrm{T}}$ is the vector containing all users' FFT outputs at the m-th receiving element. We can write

$$\mathbf{y} = \mathbf{\Phi}_A \mathbf{d} + \mathbf{w} \tag{5.6}$$

where $\mathbf{\Phi}_A = \left[\mathbf{\Phi}_1^{\mathrm{T}}, \ldots, \mathbf{\Phi}_{N_r}^{\mathrm{T}}\right]^{\mathrm{T}}$ is the overall system's channel matrix, $\mathbf{d} = [d_0, \ldots, d_{N-1}]^{\mathrm{T}}$ contains the transmitted symbols from all the users, and $\mathbf{w} = \left[\mathbf{w}_1^{\mathrm{T}}, \ldots, \mathbf{w}_{N_r}^{\mathrm{T}}\right]^{\mathrm{T}}$ is the noise vector. $\mathbf{\Phi}_m$ and $\mathbf{w}_m$ are, respectively, the channel matrix and noise vector of the m-th receiving element. To simplify the notation, from now on we drop the element

91

index m, and write the expression of the channel matrix of the m-th element as

$$\mathbf{\Phi} = \begin{bmatrix} \Phi_{0,0} & \Phi_{0,1} & \cdots & \Phi_{0,N-1} \\ \Phi_{1,0} & \Phi_{1,1} & \cdots & \Phi_{1,N-1} \\ \vdots & \vdots & \ddots & \vdots \\ \Phi_{N-1,0} & \Phi_{N-1,1} & \cdots & \Phi_{N-1,N-1} \end{bmatrix} \tag{5.7}$$

where

$$\Phi_{k,l} = \int_0^T P_k(t)P_l^*(t)dt. \tag{5.8}$$

Note that $\forall k \neq l$, $\Phi_{k,l}$ could represent the inter-carrier interference among the sub-carriers of a user (if both carriers k and l are assigned to one user), or the cross-user interference (if k and l are assigned to two different users). Similar to the derivation in [65], it can be shown that the noise covariance matrix $\mathbf{\Omega} = \mathrm{E}[\mathbf{w}\mathbf{w}^H]$ has elements $\Omega_{k,l} = N_0 T \cdot \Phi_{k,l}$. We can obtain a set of tentative decisions on $\mathbf{d}$ by a standard linear MMSE detector, i.e.,

$$\tilde{\mathbf{d}}_{\mathrm{JMMSE}} = \mathrm{Dec}\left(\mathbf{\Phi}_A{}^{\mathrm{H}} \left(\mathbf{\Phi}_A \mathbf{\Phi}_A^{\mathrm{H}} + \mathbf{\Omega} \right)^{-1} \mathbf{y} \right). \tag{5.9}$$

Taking $\tilde{\mathbf{d}}_{\mathrm{JMMSE}}$ as what is transmitted, we cancel the cross-user components in each resampling branch, i.e.,

$$\mathbf{z}(u) \approx \mathbf{\Phi}_{u,u}\mathbf{d}_u + \mathbf{w}_u \tag{5.10}$$

where the vectors $\mathbf{z}(u)$ and $\mathbf{w}_u$ are, respectively, the 'interference-free' output and noise component of the u-th branch, and $\mathbf{\Phi}_{u,u}$ is the sub-matrix of $\mathbf{\Phi}_A$ corresponding to the intended user. Note that when channel coding is incorporated, the tentative decisions used in the interference cancellation step would be generated at the output of the corresponding channel decoder. For this case, one would expect that the residual interference will be much less since some errors will be corrected by the channel decoder.

We can then proceed with a second MMSE detection, i.e.,

$$\tilde{\mathbf{d}}_{\mathrm{MMSE}}^u = \mathrm{Dec}\left(\mathbf{\Phi}_{u,u}{}^{\mathrm{H}} \left(\mathbf{\Phi}_{u,u} \mathbf{\Phi}_{u,u}^{\mathrm{H}} + \mathbf{\Omega}_{u,u} \right)^{-1} \mathbf{z}(u) \right) \tag{5.11}$$

92

where $\tilde{\mathbf{d}}_{\mathrm{MMSE}}^{u}$ contains the MMSE-based decisions for the u-th user and $\boldsymbol{\Omega}_{u,u}$ is the noise covariance matrix of the noise subset $\mathbf{w}_u$. We point out that with the proposed interference cancelation algorithm, once the tentative decisions are available, the subsequent interference cancelation and MMSE detection steps can be run separately for different users in parallel. The sizes of the matrices involved in each user's MMSE detection are $N_r \times K$. It is also worth mentioning that the proposed design is not dependent on any particular subcarrier assignment scheme – the matrices and vectors involved in the computation automatically adapt when a new subcarrier assignment is employed. Note that compared to other multiple-access systems, systems based on the OFDMA could allow for more users to transmit simultaneously. This is because users are assigned different non-overlapping carrier subsets $\mathcal{S}_u$, and hence suffer less from the IUI problem, provided that multiple resampling front end is used.

5.4.2   Exploiting Diversity via Channel Coding

To exploit the multipath diversity provided by the channel, we consider an LDPC coded system. As stated earlier, at the transmitter, the information bits are interleaved and encoded using an LDPC channel encoder. The coded bits are mapped to a sequence of complex-valued modulation symbols for transmission. At the receiver, soft information of the detected symbols is transferred to the LDPC decoder implemented using the standard sum-product algorithm [75]. The input and output of the decoder are the log-likelihood ratios (LLR) of the coded bits. Considering binary phase shift keying (BPSK) transmissions, the input LLRs are given by

$$\mathrm{LLR}_k^{in} = \log \frac{P(\hat{d}_k | d_k = \text{`0'})}{P(\hat{d}_k | d_k = \text{`1'})} \tag{5.12}$$

where LLR_k^{in} is the log-likelihood ratio of the k-th bit, $\hat{d}_k$ is the estimate of the transmitted symbol corresponding to this bit, and $P(\hat{d}_k | d_k = \text{`0'})$ and $P(\hat{d}_k | d_k = \text{`1'})$ are, respectively, the conditional probabilities of $\hat{d}_k$ given that logical '0' or '1' is transmitted. In our case, $\hat{d}_k$ is the k-th detected symbol obtained at the detector output.

Since most of the inter-user interference and inter-carrier interference has been taken care of in the detection stage, we neglect the residual interference and write each

of the detected symbols as

$$\hat{d}_k = G_k d_k + n_k \tag{5.13}$$

where G_k is the effective channel gain for the k-th subcarrier, and n_k is the additive noise excluding the residual interference. We point out that n_k is obtained by multiplying the jointly Gaussian noise vector $\mathbf{w}_u$ by the corresponding user's MMSE weight vector, and is therefore Gaussian. This enables us to compute the input LLRs as

$$\mathrm{LLR}_k^{in} = -2\hat{d}_k/\sigma^2 \tag{5.14}$$

where $\sigma = \frac{\sqrt{\mathrm{var}(n_k)}}{G_k}$ is the normalized standard deviation of n_k and $\mathrm{var}(n_k)$ is its variance. Defining $\mathbf{W}_u$ as the MMSE weight matrix – containing all the equalization coefficients – of the u-th user, we compute the equivalent channel and noise covariance matrices at this user's MMSE detector output as $\tilde{\mathbf{\Phi}}_{u,u} = \mathbf{W}_u\mathbf{\Phi}_{u,u}$ and $\tilde{\mathbf{\Omega}}_{u,u} = \mathbf{W}_u\mathbf{\Omega}_{u,u}\mathbf{W}_u^H$, where $(\cdot)^H$ denotes conjugate transpose. Then, for any $k \in \mathcal{S}_u$, G_k and $\mathrm{var}(n_k)$ can be obtained as the I_u^k-th diagonal element of $\tilde{\mathbf{\Omega}}_{u,u}$ and $\tilde{\mathbf{\Phi}}_{u,u}$, respectively, where I_u^k is the u-th user's symbol index corresponding to subcarrier k.

5.5   Channel Estimation

To estimate the path gain, path delay and Doppler scaling factor of each arrival, we adopt the orthogonal matching pursuit algorithm [66] (developed for single-user OFDM systems) to OFDMA systems. Following a similar procedure as described in Chapter 4, using pilots and decoded data symbols, a channel estimation data matrix (usually called 'dictionary') is first constructed: the columns are the projected channel outputs of all the subcarriers for each pair of the predefined path delays and Doppler scaling factors. Note that for an OFDMA system, since we have N_u users (each assigned a non-overlapping subset of all subcarriers), there are N_u sub-matrices in the complete dictionary. Each of these sub-matrices corresponds to a particular user. Otherwise, the dictionary construction is identical to what has been described in [66] in the case of OFDM systems. With the OFDMA dictionary, we proceed to use the standard orthogonal matching pursuit (OMP) algorithm to obtain an estimate of the (sparse)

channel [66]. Note that the proposed OFDMA channel estimator is not dependent on any particular pilot and subcarrier assignment scheme.

5.6 Numerical Results

In this section, we present simulation results as well as emulations with experimental data to verify the effectiveness of the front-end designs as well as to compare the two subcarrier assignment schemes (Scheme 1 and 2 as described previously).

5.6.1 Simulation Results
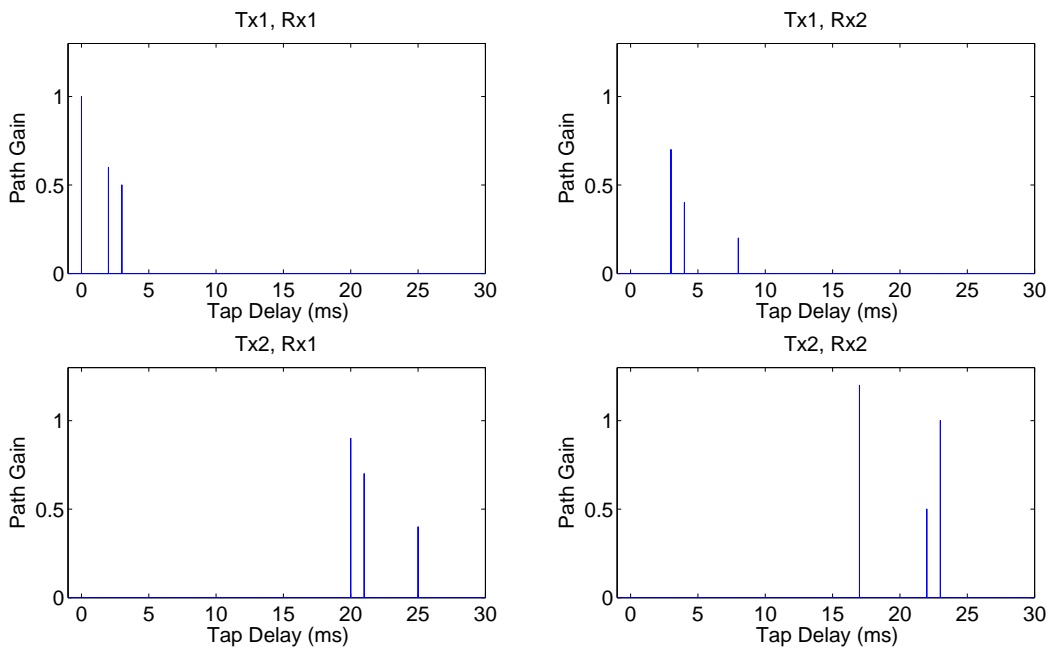
Figure 5.2: Pair-wise multipath structure of the test channel.

We consider an OFDMA system formed by two spatially separated users (each with one transmitting element) and one centralized receiver (with two receiving elements) utilizing the frequency band 12-16 kHz. The total number of subcarriers is 256 (each user is assigned 128 of them). We adopt a set of deterministic channels for different transmitter-receiver pairs and model the users' motions by suitable Doppler scaling effects. All four channels (from the transmitters to the two receiver elements) contain three non-zero paths as illustrated in Figure 5.2. The Doppler scaling factor for the
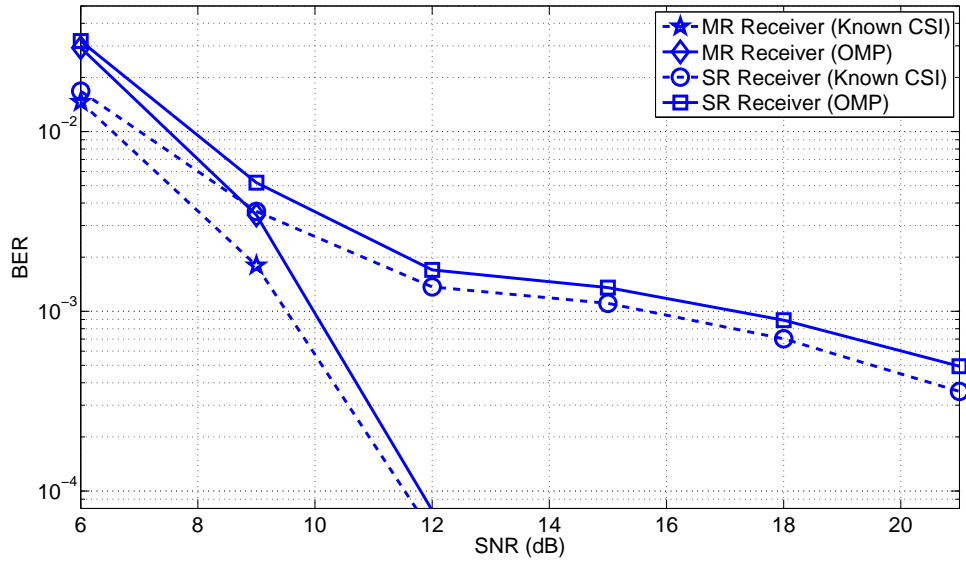
(a) Scheme 1.
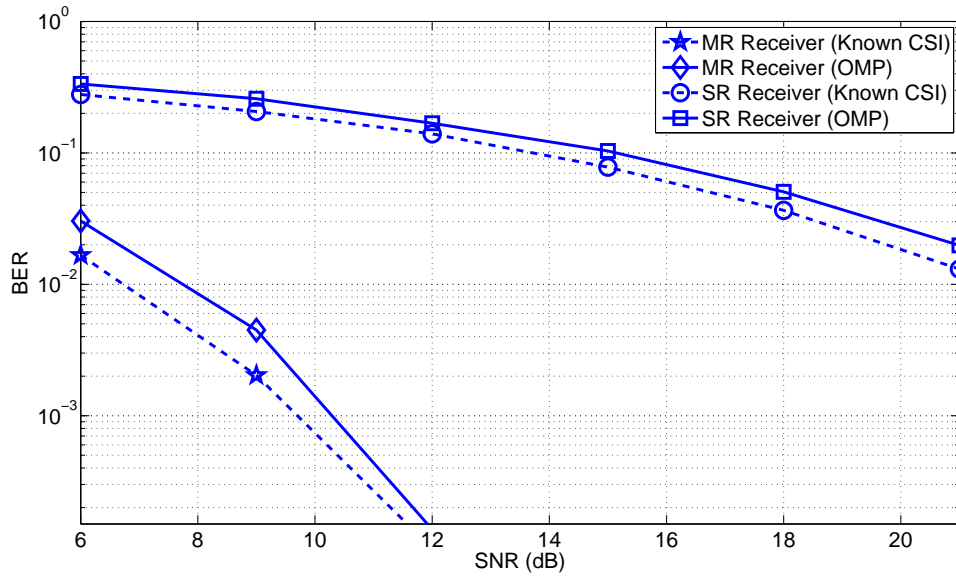
(b) Scheme 2.

Figure 5.3: BER comparison between the MR and SR receivers.

first user is set to -1.0×10^{-3}, and that for the second user is taken as 1.2×10^{-3}. The corresponding relative speeds of these two users with respect to the centralized receiver are -1.5 m/s and 1.8 m/s, respectively.

In Figure 5.3, bit error rate (BER) results are reported for the MR and SR receivers where the overall system performance with perfect receiver CSI and with es-

timated CSI are evaluated. It is observed that, for both contiguous and interleaved subcarrier assignment schemes (Scheme 1 and Scheme 2), the MR receiver greatly outperforms the SR receiver while the difference is even more pronounced for Scheme 2. This is because for the interleaved subcarrier assignment, the user-specific Doppler shifts tend to move subcarriers assigned to one user to frequencies dedicated to the other user(s), resulting in significant interference when FFT demodulation is used without compensating for these shifts. The MR receiver, in contrast, does not suffer from this problem since the user specific Doppler shifts are properly taken care of.

Consider the contiguous subcarrier assignment scheme. When each user is allocated a sufficiently large bandwidth, this scheme will benefit from multipath diversity offered by a typical UWA channel. On the other hand, if the total bandwidth available to a user is not large and Scheme 1 is used, then the overall multi-path diversity available cannot be exploited. To illustrate this point further, in the rest of this subsection, we adopt a different multipath structure and compare the performance of the two subcarrier assignment schemes when the MR receiver is used. Both a deterministic channel and a random channel are employed. For the deterministic case, the impulse responses and the frequency responses of the channel pairs are as shown in Figure 5.4. The new frequency band employed is $0.6 - 0.8$ kHz while the other parameters of the OFDMA set-up are the same as the previous example. Also, rate 0.9 and 0.8 LDPC codes of length 512 (designed for AWGN channels) are employed (spreading the codewords across four consecutive OFDMA blocks). For this hypothetical channel example, the frequency response of the lower half band is 0.9-6.1 dB less than that of the upper half band, resulting in noticeable difference of signal quality between the two subbands. Therefore, it is expected that the overall system performance will suffer if Scheme 1 is employed compared to Scheme 2 which can potentially take advantage of multipath diversity for both users.

Figure 5.5 shows the coded BERs of the interleaved and contiguous OFDMA systems for the deterministic channel case, where perfect receiver CSI and correct feedback decisions (for interference cancelation) are used. 30 iterations are performed in

97
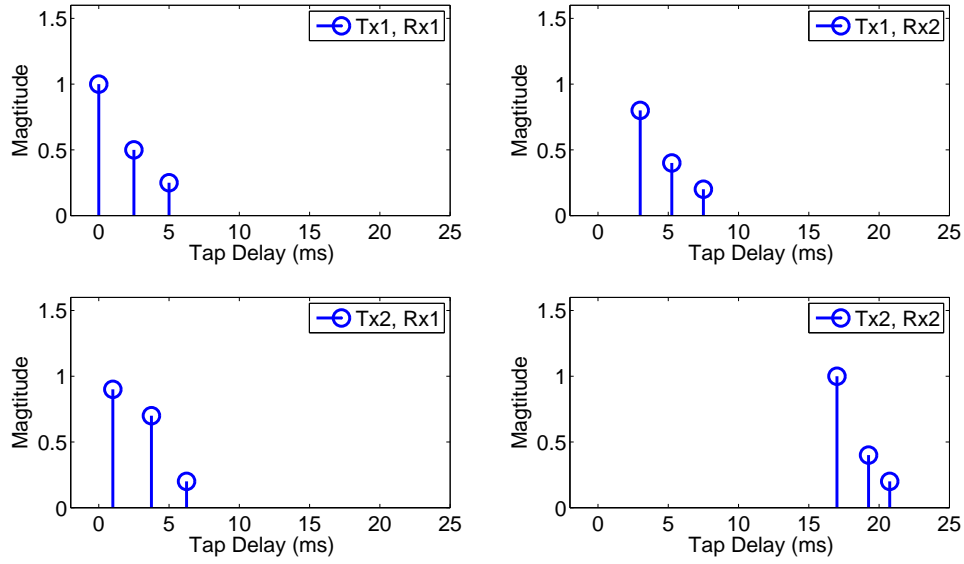
(a) Impulse response.
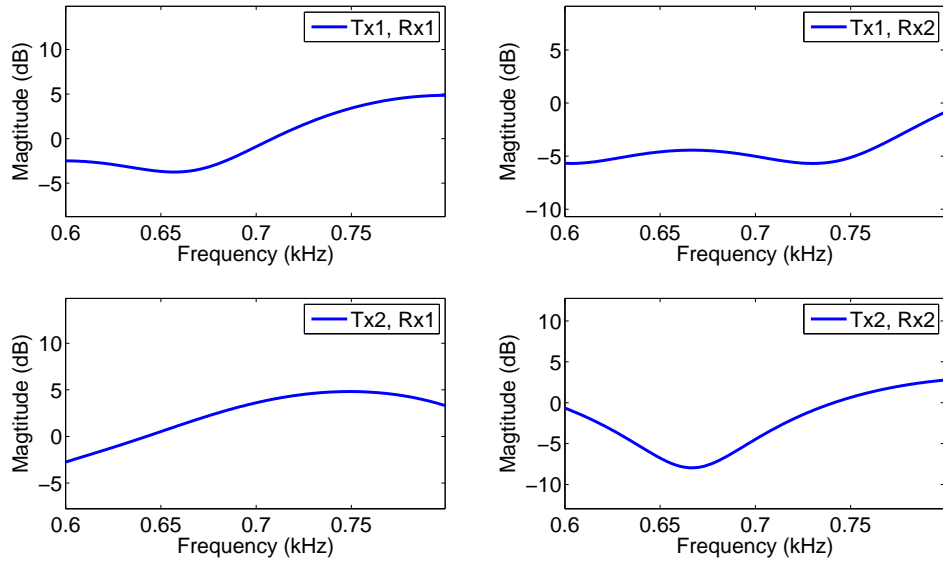
(b) Frequency response.

Figure 5.4: The deterministic channel used for simulation.
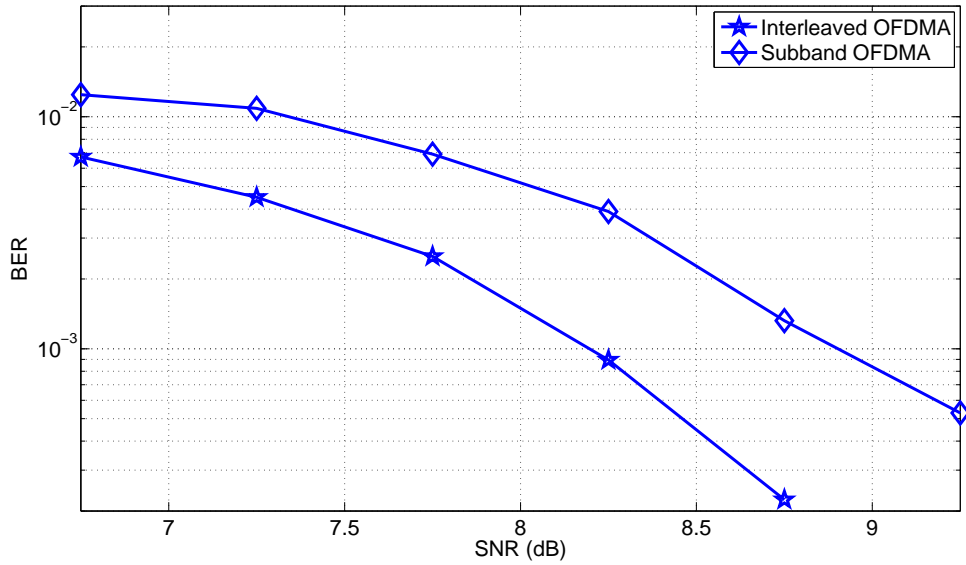
(a) Rate 0.9 LDPC code performance.
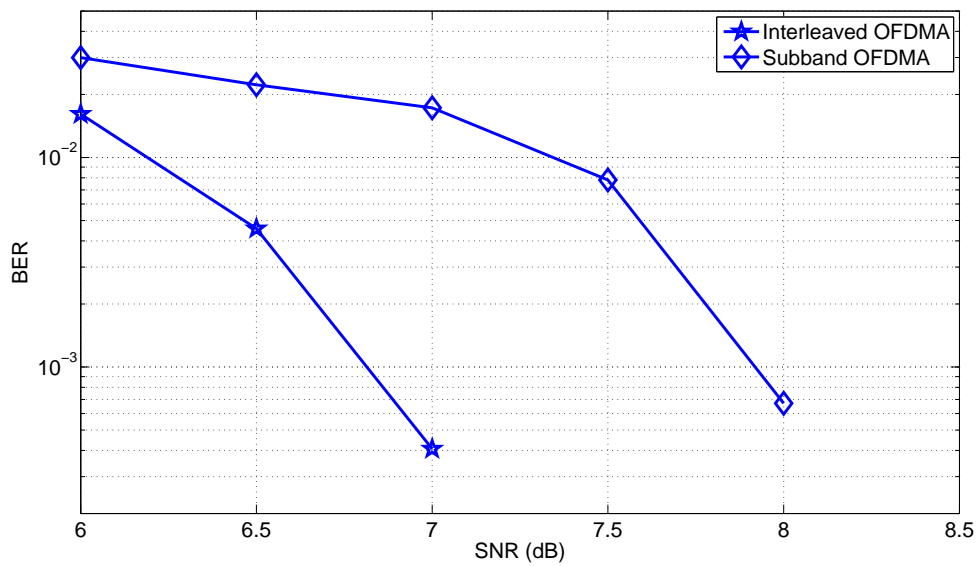
(b) Rate 0.8 LDPC code performance.

Figure 5.5: Coded BER performance over the deterministic channel example.

the sum-product algorithm. Clearly, the interleaved subcarrier assignment scheme outperforms the contiguous one considerably for both code rates.

To simulate a random channel, we consider the same multipath structure, but generate channel taps using a Rician distribution (see [59]). We assume that the channel

99
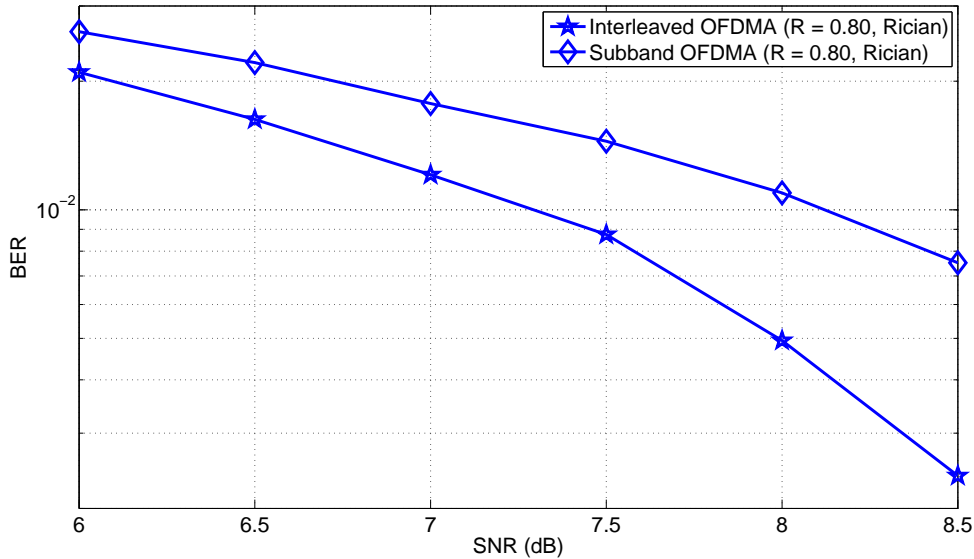
Figure 5.6: Coded BER performance on a Rician channel.

remains constant for each OFDMA block, and changes independently from one block to the next. The expected values of the realizations are equal to the tap gains of the deterministic channels, while the K factor is chosen to be 6 dB. In total, one hundred random channel realizations are generated. In Figure 5.6, we show the average coded BER obtained over different channel realizations for the rate 0.8 LDPC code adopted earlier. We observe that the interleaved system offers a performance gain of about 1 dB over Scheme 1, which is consistent with the results obtained for the deterministic case.

5.6.2 Experimental (Emulation) Results

We now examine the impact of different receiver front-end designs with emulations based on real data recorded in the MACE 10 underwater acoustic communications experiment, where one mobile source (towed at a nominal speed of about 1 m/s) and four fixed receivers were used. We control user-specific Doppler scaling effects by resampling the received signals at different rates. The originally transmitted signals are OFDM signals occupying the 10-15 kHz frequency band. The total number of subcarriers is 512, rendering a subcarrier spacing of about 10 Hz. To emulate an OFDMA system, we separate groups of subcarriers belonging to different contiguous subbands using

bandpass filters, and then resample the bandpass-filtered signals at different rates before adding them up. Effectively, we create received signals for a contiguous OFDMA system with controlled Doppler scaling factor differences. We only consider Scheme 1 as the interleaved subcarrier assignment is very difficult to emulate.

We consider two OFDMA systems, one with two users and the other with three users. The subcarriers are evenly distributed among the users (for the three-user system, the last two subcarriers are not used for transmission). For the two-user system, we adopt Doppler scaling factors of -2×10^{-3}, and 2×10^{-3}, corresponding to relative speeds of -3 m/s and 3 m/s with respect to the receiver. In the case of the three-user system, the Doppler scaling factors are -4×10^{-3} for user 1, and 2×10^{-3} for users 2 and 3 (the corresponding relative speeds are -6 m/s for user 1 and 3 m/s for users 2 and 3). Figure 5.7 shows the user-averaged BER performance of these systems. Fourteen blocks are processed in total, which includes a total of 7168 BPSK symbols. For both two-user and three-user systems, it is observed that the BER of the MR receiver is consistently and significantly lower than that of the SR receiver confirming our findings through simulations.
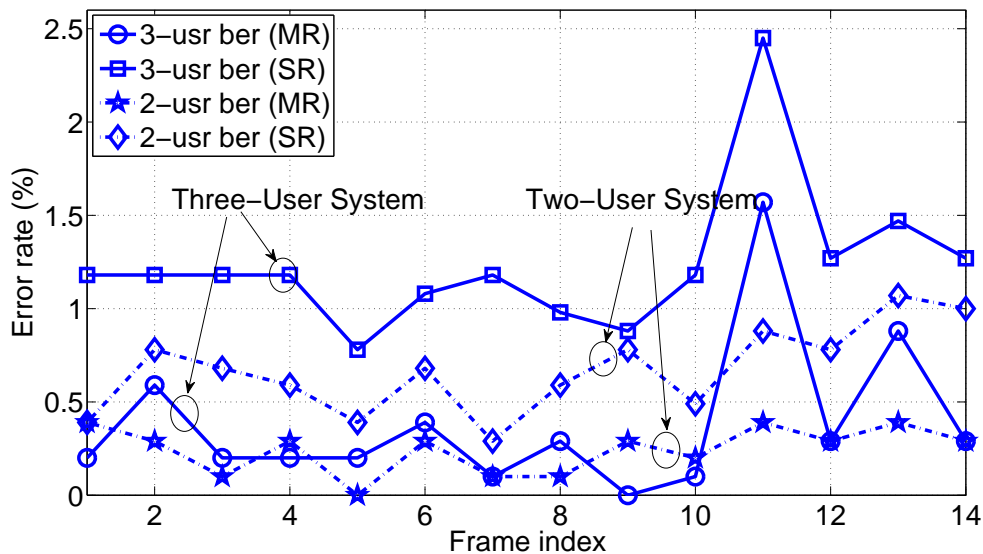
Figure 5.7: BER performance of the emulated OFDMA systems.

5.7 Chapter Summary

In this chapter, we investigated applicability of OFDMA for UWA communication networks, using two different subcarrier assignment schemes (contiguous and interleaved). To compensate for the user-specific Doppler scaling effects, a multiple resampling front end is found to be necessary. Following this stage, interference cancelation is employed based on sparse channel estimation and iterative decoding. Note that this post-detection stage does not vary with particular pilot and/or carrier assignment. Via simulations and emulations based on experimental data, we demonstrate significant performance advantages of the proposed multiple-resampling design. As for the contiguous versus interleaved subcarrier assignment strategies, there is not a clear winner; however, the interleaved assignment may be desirable when many users share a limited spectrum and each has access to only a small portion of the overall bandwidth.

Chapter 6

CAPACITY EVALUATION OF OFDM SYSTEMS OVER DOPPLER DISTORTED

UNDERWATER ACOUSTIC CHANNELS

In the previous chapters, we have developed various OFDM receiver, which outperform the conventional/standard receivers for Doppler-distorted underwater acoustic channels. In this chapter, we investigate the performance of the proposed multiple-resampling and conventional single-resampling receivers using the channel capacity of the equivalent discrete-time models as a metric. For both receivers, we consider discrete channel models that characterize the relationships between the transmitted symbols and the corresponding receiver's demodulation output. We derive the channel matrices and the noise covariance matrices that uniquely define these channels, and propose numerically stable methods to evaluate the corresponding channel capacities. Via numerical evaluations, we demonstrate that the MR receiver offers a higher channel capacity than the SR receiver when the channel is affected by path-specific Doppler distortions.

The chapter is organized as follows. Section 6.1 introduces some of the existing capacity results for UWA channels, and summarizes our methodology for the channel capacity comparison of the MR and SR receivers. Section 6.2 gives the system model. In Sections 6.3 and 6.4, we derive the discrete channel models for the SR and the MR receivers, respectively. In Section 6.5, we present numerically stable methods for channel capacity evaluation based on these discrete models. In Section 6.6, we report numerical evaluation results and our findings on the differences in the capacities supported by the SR and MR receivers. Finally, Section 6.7 concludes the chapter.

6.1 Introduction

As an effective way to characterize the ultimate transmission rate of UWA communications, channel capacity analysis of the UWA channels have recently gained some attention [76–79]. Most of these analysis techniques either focus on channels unaffected by Doppler [79–82] (i.e., time-invariant) or channels, which are subject to the Doppler spreading effect (i.e., random tap gain variations) only [76,77,83]. In the latter case, the

103

channels can be well-represented by the basis expansion model (BEM) proposed in [45]. The problem is, as has been witnessed by several recent at sea underwater acoustic communication experiments [2, 67], that the UWA channels, in most cases, are subject to Doppler scaling effects instead of Doppler spreading. This fact limits the use of the BEM-based methods for capacity analysis in many practical scenarios.

In this chapter, our objective is to study the difference between the MR and SR receivers using channel capacity as a performance metric. In particular, our channel capacity analysis starts by examining the frequency-domain samples obtained at a particular receiver's demodulation output. We then describe the equivalent discrete channel model that characterizes these demodulated samples. The equivalent discrete channels are uniquely defined by channel matrices, which specify the subcarrier gain and the crosstalk among different subcarriers, and the noise covariance matrix. While the discrete model for the SR receiver is relatively straightforward, that for the MR receiver is more involved. In particular, unlike the case of the SR receiver, where the noise is white, the noise of the output of the MR receiver is colored.

We point out that given the discrete channel models, the capacity analysis of the corresponding receivers boils down to the capacity analysis of standard MIMO channels with large fixed channel matrices and noise covariance matrices. To enable numerically stable capacity evaluation based on these large linear systems, we adopt singular value decomposition (SVD) based methods to break down the problem into that of an equivalent set of decoupled channels. Via numerical evaluations, we demonstrate that, while Doppler rate difference may cause the SR receiver to suffer a noticeable channel capacity loss, the MR receiver may be able to properly cope with it and even exploit it as a performance benefit to increase the channel capacity. The channel capacity difference does not disappear even if the subcarriers are well-separated.

6.2   OFDM System Model

Consider an N-subcarrier OFDM system with a cyclic prefix (CP) duration T_g, a block duration T, and modulation symbols belonging to a complex-valued constellation. The

transmitted signal can be written as [25]

$$s(t) = \text{Re} \left\{ \sum_{k=-N/2}^{N/2-1} d_k e^{j2\pi f_k t} R(t) \right\} \tag{6.1}$$

where f_c is the center subcarrier frequency, $\{d_k\}$ are the data symbols modulated onto the frequency $f_k = f_c + k/T$, $R(t)$ is the modulation pulse of duration $T + T_g$, and $\text{Re}\{\cdot\}$ denotes the real part of its argument. Throughout the chapter we assume that the CP is sufficiently long to prevent inter-block interference. Hence, we focus on a single-block OFDM signal. Further, we assume that $R(t)$ is a rectangular pulse.

The transmitted signal, $s(t)$, travels through a time-varying UWA channel, where we assume that the channel variations are only caused by the Doppler scaling effects (over the codeword). As reported in several at sea UWA communications experiments, this condition is typical for many real UWA channels [2, 67]. Therefore, we are able to formulate the received signal as

$$r(t) = \sum_{p=0}^{N_p-1} h_p s \left(t + a_p t - \tau_p \right) + u(t) \tag{6.2}$$

where N_p is the number of paths, h_p, τ_p, and a_p (assumed constant for the frame duration and perfectly known to the receiver) are, respectively, the path gain, delay, and Doppler scaling factor of the pth path, and $u(t)$ is a white Gaussian process with power spectral density $\frac{N_0}{2}$.

Assuming perfect timing synchronization and cyclic prefix removal [25], we express the lowpass equivalent (LPE) of the resulting signal (with respect to the center carrier frequency f_c) as

$$y(t) = v(t) + n(t) \tag{6.3}$$

where

$$v(t) = \sum_{p=0}^{N_p-1} \sum_{k=-N/2}^{N/2-1} \underbrace{h_p e^{-j2\pi f_k \tau_p}}_{\alpha_{p,k}} d_k e^{j2\pi k(1+a_p)t/T} e^{j2\pi a_p f_c t}, \tag{6.4}$$

105

contains the scaled and delayed signal arrivals and $n(t) = \text{LPF}\left\{u(t)e^{-j2\pi f_c t}\right\}$ is the filtered in-band noise with power spectral density

$$S_n(f) = \begin{cases} N_0, & f \in \left[-\frac{B}{2}, \frac{B}{2}\right], \\ 0, & \text{elsewhere.} \end{cases} \tag{6.5}$$

6.3 Discrete Channel Model of the Single-Resampling Receiver

In order to cope with the Doppler-induced distortions, conventional OFDM receivers (as described in Chapter 4 as the SR receivers) usually employ a Doppler mitigation stage, which does a one-time resampling of the received signal based on the average Doppler rates of all paths [30]. For simplicity, we assume zero average Doppler rate[1] such that the SR receiver can be implemented as a simple correlator, i.e.,

$$y_k = \int_0^T y(t)e^{-j2\pi kt/T} dt. \tag{6.6}$$

The corresponding equivalent discrete channel model can therefore be written as

$$y_k = \sum_{m=-N/2}^{N/2-1} H_{k,m} d_m + w_k \tag{6.7}$$

where $H_{k,m}$ is the intercarrier interference (ICI) coefficient, which defines the interference of the m-th subcarrier to the k-th subcarrier, and w_k is the noise. Derivation of $H_{k,m}$ can be found in [64] and Chapter 4, while, the noise cross-correlation, which defines the statistical behavior of w_k, is given by

$$\text{E}\left[w_k w_m^*\right] \approx N_0 T \delta(k-m), \tag{6.8}$$

where the approximation holds as $\{w_k\}_{k=-N/2}^{N/2-1}$, when evaluated in the discrete-time domain, are nothing but a set of uncorrelated random variables – generated by a unitary transformation (specified by the FFT matrix) of the white inband noise samples.

6.4 Discrete Channel Model of the Multiple-Resampling Receiver

Unlike the SR receiver, which is implemented as a simple correlator, the MR receiver in Chapter 4 effectively matched-filters the lowpass equivalent $y(t)$ by correlating it with

---

[1]For the case of non-zero average Doppler rate, we can always adopt a time-scaling stage to pre-compensate for the non-zero average Doppler scaling such that the methods/models based on the zero average Doppler rate assumption will apply with appropriately redefined channel transfer function.

the modulation pulse of each subcarrier [64]. The result of this matched-filtering process is a set of sufficient statistics that can be exploited for effective data detection. To find the discrete channel model of this receiver, we first write its output as

$$
\begin{aligned}
z_k &= \int_0^T y(t) \sum_{p=0}^{N_p-1} \alpha_{p,k}^* e^{-j2\pi a_p f_c t} e^{-j2\pi k(1+a_p)t/T} dt \\
&= \sum_{m=0}^{N-1} \Phi_{k,m} d_m + \eta_k,
\end{aligned}
\tag{6.9}
$$

where $\Phi_{k,m}$ is the ICI coefficient that defines the interference from the m-th subcarrier to the k-th subcarrier, and

$$
\eta_k = \int_0^T n(t) \sum_{p=0}^{N_p-1} \alpha_{p,k}^* e^{-j2\pi a_p f_c t} e^{-j2\pi k \Delta f(1+a_p)t} dt
\tag{6.10}
$$

is the noise term that contains correlated versions of the noise $n(t)$ sampled at different rates. It is shown in Chapter 4 that the matched-filter based receiver can be effectively implemented as a front end-structure which includes multiple-resampling branches, each mitigating the Doppler distortion of a particular path.

Derivation of $\Phi_{k,m}$ appeared in our previous work [64] and in Chapter 4. We herein give its final expression as

$$
\begin{aligned}
\Phi_{k,m} &= \int_{-\infty}^{\infty} P_m(t) P_k^*(t) dt \\
&= \sum_{p=0}^{N_p-1} \sum_{q=0}^{N_p-1} \alpha_{p,k}^* \alpha_{q,m} \int_0^T e^{-j2\pi(1+a_p)f_k t} e^{-j2\pi(1+a_q)f_m t} dt
\end{aligned}
\tag{6.11}
$$

where

$$
P_k(t) = \begin{cases} \sum_{p=0}^{N_p-1} \alpha_{p,k} e^{j2\pi a_p f_c t} e^{j2\pi k \Delta f(1+a_p)t}, & t \in [0, T] \\ 0, & \text{elsewhere} \end{cases}
\tag{6.12}
$$

is the equivalent modulation pulse for the transmitted symbol of the k-th subcarrier. Regarding the noise terms $\{\eta_k\}$, we point out that unlike the SR case, for which the noise is approximately white, strong correlation exists among the noise variables. Particulary, the noise cross-correlation is found to be approximately a scaled version of the MR receiver's ICI coefficient, i.e.,

$$
\mathrm{E}\left[\eta_k \eta_m^*\right] \approx N_0 \Phi_{k,m},
\tag{6.13}
$$

where the approximation holds for the similar reason discussed in Section 6.3. The detailed derivation of this result can be found in Appendix B. Note that the arguments in this chapter can be generalized to an arbitrary OFDM shaping pulse and the case of colored in-band noise. Interested readers are referred to Appendices C and D for details.

6.5   Capacity Evaluation

Capacity evaluation is based on the discrete channel models described in Sections 6.3 and 6.4. We confine ourselves to the standard OFDM modulation scheme and particular receiver designs, namely the SR and the MR receivers. Perfect receiver CSI and no transmitter CSI are assumed. Under these assumptions, equal power is allocated to all the carriers, with the power constraint $\mathrm{E}\left\{|d_k|^2\right\} = 1$.

6.5.1   SR Receiver

The discrete channel model (6.7) is mathematically equivalent to that of a fixed MIMO system with AWGN. Defining the receiver-side SNR as

$$\gamma = \frac{\frac{1}{B}\int_0^T |v(t)|^2 dt}{N_0 T}, \tag{6.14}$$

the capacity C_{SR} of this system (with Gaussian signaling and equal transmitted signal power constraint $\mathrm{E}\left\{|d_k|^2\right\} = 1$) is given in [68] by

$$C_{\mathrm{SR}} = \log\det\left(\mathbf{H}\mathbf{H}^{\mathrm{H}} + N_0 T \cdot \mathbf{I}\right) \tag{6.15}$$

where $\{\cdot\}^{\mathrm{H}}$ denotes the conjugate transpose, $\mathbf{H}$ is the channel matrix whose entry on the k-th row and the m-th column is given by the ICI coefficient $H_{k,m}$, and $\mathbf{I}$ is an identity matrix.

Direct evaluation of C_{SR} for large $\mathbf{H}$ is numerically unstable. We thus adopt an equivalent expression for Equation (6.15) based on singular value decomposition (SVD), i.e., $\mathbf{H}\mathbf{H}^{\mathrm{H}} = \mathbf{U}\mathbf{\Sigma}\mathbf{V}^{\mathrm{H}}$, where $\mathbf{U}$ and $\mathbf{V}$ are unitary matrices and $\mathbf{\Sigma}$ is a diagonal matrix containing the singular values $\lambda_k = \sigma_k^2$. The resulting capacity formula is given by

$$C_{\mathrm{SR}} = \sum_{k=0}^{N-1} \log\det\left(N_0 T + \lambda_k\right). \tag{6.16}$$

108

We follow a similar approach for capacity evaluation of the MR receiver, in this case, using the discrete channel model in (6.9). Direct evaluation is numerically unstable as in the case of the SR receiver. In addition to this, we also want to account for the general case, in which the channel matrix $\boldsymbol{\Phi}$ (with entries $\Phi_{k,m}$) and/or the noise covariance matrix $\boldsymbol{\Omega}$ (with entries $\mathrm{E}\{\eta_k \eta_m{}^*\}$) are singular.

To tackle the problem of singularity, we start from

$$
\begin{aligned}
C_{\mathrm{MR}} &= \log\det\left(\mathrm{E}\left[\mathbf{y}\mathbf{y}^{\mathrm{H}}\right]\right) - \log\det\left(\mathrm{E}\left[\boldsymbol{\eta}\boldsymbol{\eta}^{\mathrm{H}}\right]\right) \\
&= \log\det\left(\boldsymbol{\Phi}\boldsymbol{\Phi}^{\mathrm{H}} + \boldsymbol{\Omega}\right) - \log\det\left(\boldsymbol{\Omega}\right),
\end{aligned}
\tag{6.17}
$$

where, just as in the case of the SR receiver, Gaussian signaling and equal power allocation are assumed. Noticing that the singularity issue is caused by the fact that the signal vector $\mathbf{y}$ has redundant coordinates, we first aim at identifying and removing the coordinates that bear no information. That is, we apply a SVD, which, by a linear transformation, turns $\mathbf{y}$ into two parts: the first part has entries with non-zero eigenvalues, and the second part has those whose eigenvalues are zero. We keep only the first part of the linearly transformed signal, which effectively yields a new linear system given by

$$
\tilde{\mathbf{y}} = \tilde{\boldsymbol{\Sigma}}\tilde{\mathbf{d}} + \tilde{\boldsymbol{\eta}},
\tag{6.18}
$$

where $\tilde{\mathbf{y}}$, $\tilde{\mathbf{d}}$, and $\tilde{\boldsymbol{\eta}}$, are, respectively, the output vector, input vector and noise of the new linear system, and $\tilde{\boldsymbol{\Sigma}}$ is the new channel mixing matrix.

Referring to (6.18), we can apply two other SVD's, one for the new signal vector $\tilde{\mathbf{y}}$'s covariance matrix, and the other for the new noise vector's covariance matrix. The capacity of the MR receiver can now be expressed as the difference between entropies of the signal and the noise,

$$
C_{\mathrm{MR}} = \sum_{k=0}^{M-1} \log\det\left(\lambda_k^y\right) - \log\det\left(\lambda_k^\eta\right)
\tag{6.19}
$$
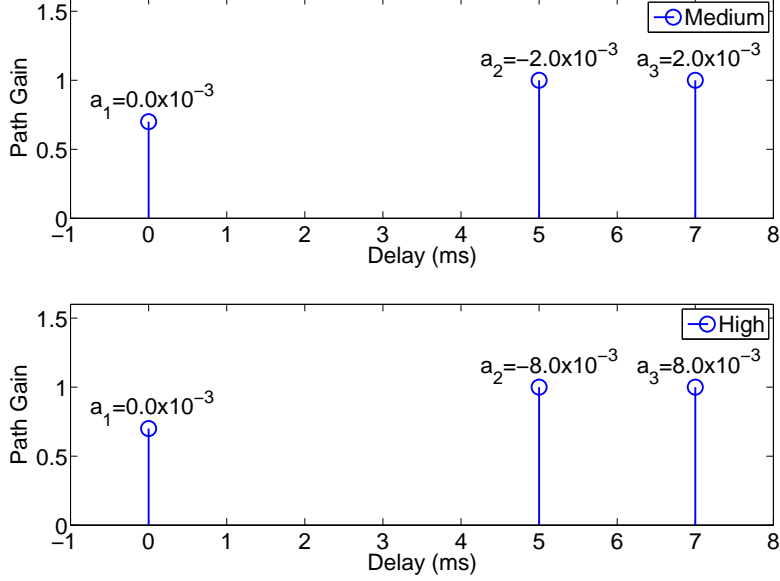
Figure 6.1: Multipath delay profile of Channel A.

where λ_k^y and λ_k^η are, respectively, the singular values of $\tilde{\mathbf{y}}$'s covariance matrix and that of $\tilde{\boldsymbol{\eta}}$'s covariance matrix.

6.6   Numerical Examples

Using several numerical examples, we now demonstrate the capacity difference between the MR and the SR systems, where the capacity is evaluated both over channels with fixed h_p, a_p, and τ_p in Equation (6.2), and random channels. The channel capacity in the former case can be interpreted as an instantaneous capacity of the channel (where the path gains and delays are constant over one OFDM block). For the latter, the path gains are realizations of a set of Rician random variables – the path delays are still fixed. In this case, the channel capacity can be interpreted as the ergodic capacity of the channel.

6.6.1   Capacity Results of Channels with Fixed Parameters

We consider two sparse UWA channels, namely Channel A and Channel B. As shown in Figure 6.1 and Figure 6.2, each of these channels has three dominant paths, where each path is associated with a different Doppler scaling factor (indicated next to the

110
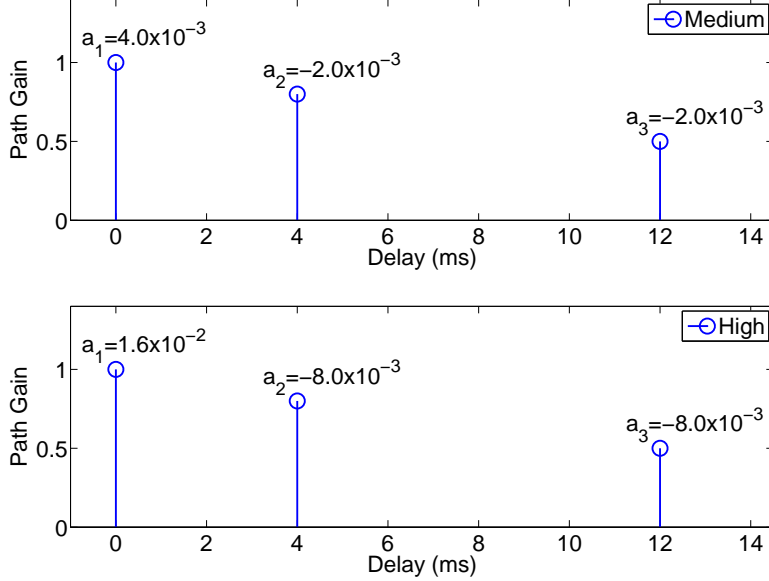
Figure 6.2: Multipath delay profile of Channel B.

corresponding paths). We choose two levels of the Doppler scaling factor difference. The medium level corresponds to an average Doppler scaling factor difference of 4.0×10^{-3} (equivalent to a speed difference of 6.0 m/s for acoustical waves traveling along different propagation paths), and the high level is associated with a Doppler scale difference of 1.6×10^{-2} (equivalent to a speed difference of 24 m/s). Over the two channels, we transmit an OFDM signal with bandwidth $B = 2$ kHz (in the band $25 - 27$ kHz), and a different number of subcarriers indicated by N in Table 6.1. We adopt the equivalent discrete channel models of Section 6.2 and capacity evaluation methods of Section 6.5 to compare the resulting channel capacity of the MR and the SR receivers.

In Figure 6.3, we compare the capacity of the MR and SR receivers for Signal 1 parameter set over channel A. Results are examined under the medium and the high Doppler scale differences as depicted in Figure 6.1. The subcarrier spacing in this case is 3.9 Hz. For both Doppler scale differences, we observe that the MR receiver is able to offer higher channel capacity compared to the SR receiver. It is also noticed that as the Doppler scale difference increases, the channel capacity of the SR receiver degrades, which may imply a potential information loss when the SR receiver is used. On the

111

	Signal 1	Signal 2
N	512	256
Δf (Hz)	3.9	7.8

Table 6.1: OFDM signal parameters.
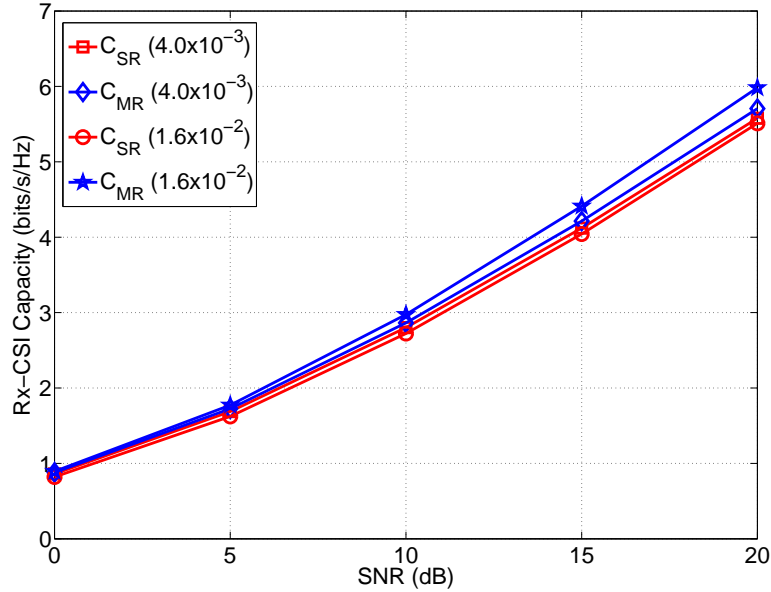
Figure 6.3: Capacity comparison for SR and MR receivers with 512 subcarriers transmitted over Channel A.

contrary, for the MR receiver, the channel capacity is observed to improve as we increase the Doppler scale difference. This tells us that instead of suffering from the increased Doppler scale difference, the MR receiver design may in fact be able to exploit and translate it into an actual performance benefit.

Similar results are observed for Signal 2 parameter set as shown in Figure 6.4, where with a reduced OFDM block size, the subcarrier spacing is increased to 7.8 Hz. The performance degradation in the case of the SR receiver and performance improvement in the case of the MR receiver are almost the same as those for the previous example. We observe that the information loss due to the SR receiver may not be mitigated by simply increasing the frequency separation between the consecutive subcarriers. On the contrary, the MR receiver may be beneficial regardless of the choice of the subcarrier separation. Interestingly, Figures 6.3 and 6.4 are almost identical. This
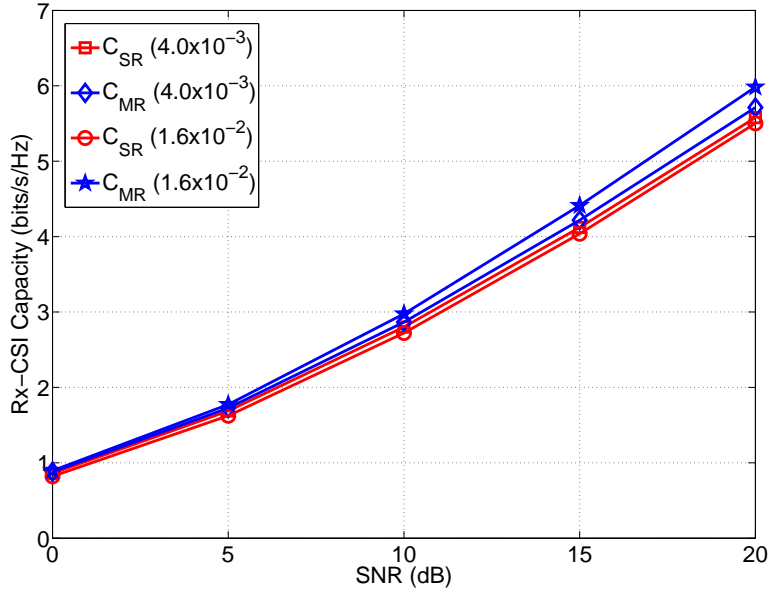
Figure 6.4: Capacity comparison for SR and MR receivers with 256 subcarriers transmitted over Channel A.

is because for OFDM systems with a large number of subcarriers (in our case, 512 and 256), the frequency response of the channel can be adequately 'sampled' by the evenly distributed subcarriers such that there may be very little distortion in the sampled version of the channel, and therefore, ignoring the overhead due to the cyclic prefix, the corresponding system capacity converges to the ultimate capacity of the channel [84]. In our case, the above statement is obviously valid since the subcarrier spacings (3.9 Hz for the first case, 7.8 Hz for the second case) are both much less than the channel's coherence bandwidth of 140 Hz.

In Figures 6.5, and 6.6, we show similar channel capacity comparison results for signals transmitted over Channel B. In particular, we observe further differentiated channel capacity results between the MR and SR receiver designs. In addition, as the Doppler scale difference increases, the channel capacity of the SR receiver tends to degrade faster compared to Channel A, implying a severe information loss caused by the suboptimal SR receiver design. Similar to the case of Channel A, increasing the subcarrier spacing (by decreasing the number of subcarrier) does not narrow the performance gap, which reiterates the fact that the MR receiver should still be considered even if

113
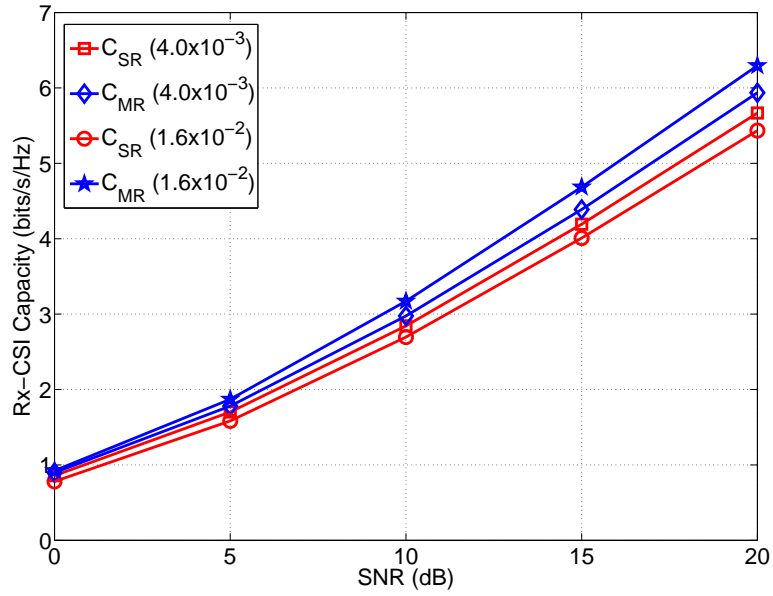
Figure 6.5: Capacity comparison for SR and MR receivers with 512 subcarriers transmitted over Channel B.
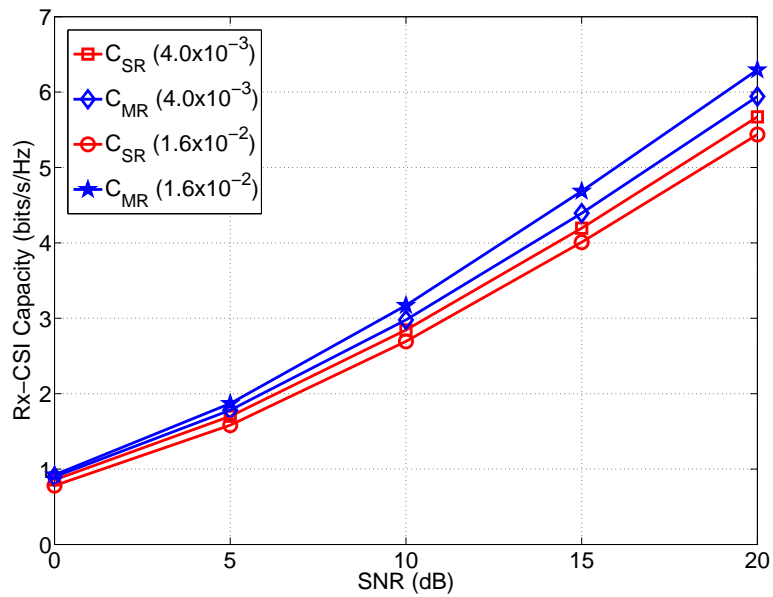
Figure 6.6: Capacity comparison for SR and MR receivers with 256 subcarriers transmitted over Channel B.
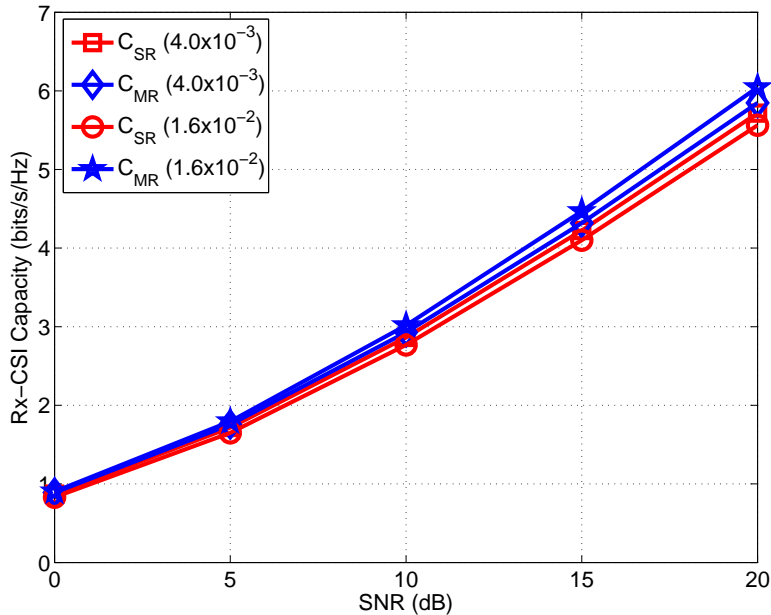
Figure 6.7: Capacity comparison for SR and MR receivers with 512 subcarriers transmitted over random Channel A.

subcarriers are well separated from each other.

6.6.2 Capacity Results of Random Channels

We now evaluate channel capacity over two sets of random channels, hereafter referred to as random Channel A and random Channel B. Here, the path gains are subject to Rician distributions with a 12 dB K factor, while the path delays are fixed – the multipath structures of the random channels are the same as those of the fixed channels considered previously. As reported in [59], Rician distribution is a good statistical fit for the channel tap gains observed in UWA channels. Using 256-subcarrier OFDM as the transmitted signal, we show the corresponding ergodic channel capacities in Figure 6.7 (Channel A), and Figure 6.8 (Channel B), respectively. The capacity curves are obtained by averaging instantaneous capacities of 100 different Rician channel realizations. As demonstrated in these figures, previous observations made for the fixed channel cases also apply to the case of random channels, where MR receivers remain advantageous compared to SR receivers if the Doppler distortions of these channels are path-specific.

115
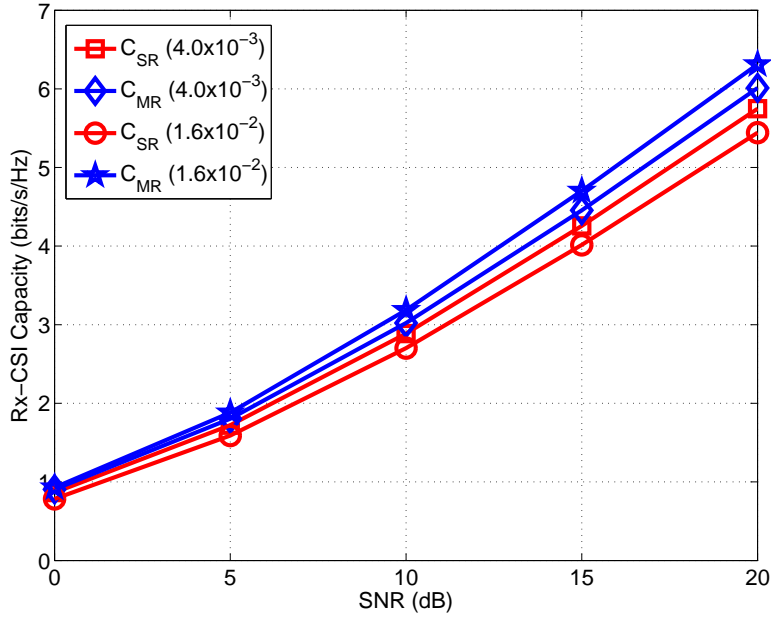
Figure 6.8: Capacity comparison for SR and MR receivers with 256 subcarriers transmitted over random Channel B.

6.7   Chapter Summary

In this chapter, by utilizing the discrete channel models pertaining to different receiver designs, we evaluated and compared the channel capacities of the conventional SR and the proposed MR receivers. The channel capacity comparisons made in this chapter complement the error rate studies conducted in Chapter 4, and reveals the limits of reliable transmission rates when the SR and MR receivers are employed. In particular, numerical examples demonstrate that the MR receiver is superior to the SR receiver in coping with the path-specific Doppler distortions, and offers a higher channel capacity. Furthermore, it may potentially transform the Doppler rate differences into actual performance benefits. In contrast, the SR receiver suffers a noticeable channel capacity loss.

Chapter 7

SUMMARY AND FUTURE WORK

Due to limited bandwidth and large multipath spreads of UWA channels, OFDM has recently emerged as a promising modulation alternative for UWA communications, thanks to its high bandwidth efficiency and superior performance over severely dispersive channels. However, with the increase of the OFDM frame length, the generally-held time-invariance assumption is no longer valid due to the highly dynamic nature of the UWA environments as well as strong motion-induced Doppler distortions. As such, interference arises among subcarriers and can cause significant degradation in the system performance.

In this thesis, we have devised various strategies for ICI mitigation. For ICI due to random channel variations, we developed two adaptive frequency domain equalization schemes. The first scheme utilizes a decision feedback equalizer (DFE) coupled with a second order phase tracking loop to account for the phase rotations (of the equalizer's tap coefficients) due to timing synchronization errors. The second scheme adopts a linear MMSE equalizer exploiting the frequency domain channel estimates obtained by closed-loop tracking through a second order gradient algorithm, where special care was taken for the timing synchronization errors as well. Both schemes exploit the fact that the ICI may only arise in several neighboring subcarriers (after initial Doppler mitigation), which results in effective frequency domain equalizers that only had a very limited number of tap coefficients. Via simulations as well as emulations based on experimental data, we demonstrated that the proposed ICI mitigation schemes achieve significant performance gains.

For ICI due to time variations caused by path and/or user specific Doppler scaling effects, we invented a family of unique multi-rate resampling receiver designs, where each resampling branch is tasked with the Doppler distortion of each particular path and/or user. To exploit the benefits of these designs, we also developed customized sparse channel estimation and data detection schemes. The proposed channel estimator,

by advancing the existing estimators with a local search step, alleviates the basis mismatch problem faced by the commonly-used sparse channel estimation algorithms such as basis pursuit and orthogonal matching pursuit algorithms. The proposed data detector, by augmenting linear detectors with an additional interference cancelation step, strikes a balance between performance and complexity. The proposed multi-rate resampling designs were explored both for single-user (peer-to-peer) and multiuser MIMO communications scenarios. It has been shown through extensive simulations and real data based emulations that for both single-user and multiuser scenarios, the multi-rate resampling receivers are able to offer significant performance gains over the conventional single-resampling receivers.

To facilitate multiple access over a UWA channel, we have also investigated OFDMA systems, where the benefits of multipath diversity was exploited through contiguous and interleaved subcarrier assignment schemes and LDPC channel coding. We presented a complete receiver design, including an OFDMA-specific multi-rate resampling front end and an interference-cancelation-based detection/decoding back end, both of which are enabled for practical use by an effective sparse channel estimation scheme. The effectiveness of the proposed design was verified both via simulations as well as emulations based on real experimental data.

Finally, to complement the error rate studies for the MR and SR receivers, we also compare their performance difference in terms of the channel capacity they offer by exploiting capacity evaluation techniques based on the equivalent discrete channel models. Through numerical examples, we demonstrate that, for UWA channels affected by path-specific Doppler distortions, the MR receiver offers a higher channel capacity than that achieved by the SR receiver. Moreover, the MR receiver may exploit the Doppler rate difference as a performance benefit, while the SR receiver may suffer a noticeable channel capacity loss.

We now would like to cite a number of possible future research avenues. For UWA channels affected by path and/or user-specific Doppler distortions, besides exploiting the receiver-side CSI, one may also develop different ways to exploit the trans-

mitter side CSI. For instance, the overall system performance can be further improved if the transmitter knows the Doppler scaling factors, path gains, and path delays at the receiver side. Benefiting from this information, it may be possible to allocate the transmission power and adjust the signal constellations efficiently to increase the overall data throughput/channel capacity. In addition, the transmitter-side CSI can also help combat the user-specific Doppler distortions. For example, one may implement a resampling stage at the transmitting node such that the Doppler distortions at the receiver can be greatly reduced.

Another direction one might pursue is the utilization of space-frequency block codes to exploit the diversity gain offered by cooperative multiuser MIMO transmissions. Here, the interesting topic might be how the the user specific Doppler distortions can be handled at the receiver-side with properly designed receiver structures and decoding algorithms. It is possible that the multiple-resampling design will still be adopted, however, it is unclear that whether or not the orthogonality property of the original codes can still be maintained.

Last but not the least, one might also pursue a more fundamental channel capacity analysis that starts from the continuous time domain waveforms channel model instead of the discrete channel models that are tied to particular receiver designs. The question is how the path/user specific Doppler scalings will affect the channel capacity. This seems to be a challenging problem; however, it would help answer the channel capacity of a linear time-varying channel in a fundamental way. It would also be interesting to compare this capacity result with what have been obtained for OFDM adopting MR and SR receiver designs.

REFERENCES

[1] M. Stojanovic, "Underwater Acoustic Communications: Design Considerations on the Physical Layer," in *Proc. Wireless on Demand Network Systems and Services*, Jan. 2008, pp. 1–10.

[2] W. S. Hodgkiss, H. C. Song, M. Badiey, A. Song, and M. Siderius, "Kauai Acomms MURI 2008 (KAM08) Experiment — Trip Report," Tech. Rep., Jul. 2008.

[3] M. Stojanovic, "Recent Advances in High-Speed Underwater Acoustic Communications," *IEEE Journal of Oceanic Engineering*, vol. 21, no. 2, pp. 125–136, Apr. 1996.

[4] J. G. Proakis, *Digital Communications*, 4th ed. McGraw-Hill, 2001.

[5] M. Stojanovic, "Low Complexity OFDM Detector for Underwater Acoustic Channels," in *Proc. IEEE Oceans 2006*, Boston, MA, Sep. 2006, pp. 1–6.

[6] Y. Emre, V. Kandasamy, T. M. Duman, P. Hursky, and S. Roy, "Multi-Input Multi-Output OFDM for Shallow-Water UWA Communications," in *Proc. Acoustics*, Jun. 2008, pp. 13–17.

[7] B. Li, J. Huang, S. Zhou, K. Ball, M. Stojanovic, L. Freitag, and P. Willett, "Further Results on High-Rate MIMO-OFDM Underwater Acoustic Communications," in *Proc. IEEE Oceans 2008*, Quebec City, Canada, Sep. 2008, pp. 1–6.

[8] ——, "MIMO-OFDM for High Rate Underwater Acoustic Communications," *IEEE Journal of Oceanic Engineering*, vol. 34, no. 4, pp. 634–645, Oct. 2009.

[9] S. Mason, C. Berger, S. Zhou, K. Ball, L. Freitag, and P. Willett, "An OFDM Design for Underwater Acoustic Channels with Doppler Spread," in *Proc. Digital Signal Processing Workshop and 5th IEEE Signal Processing Education Workshop*, Jan. 2009, pp. 138–143.

[10] K. Tu, D. Fertonani, T. M. Duman, and P. Hursky, "Mitigation of Intercarrier Interference in OFDM Systems over Underwater Acoustic Channels," in *Proc. IEEE Oceans 2009*, Bremen, Germany, 6 pages, May 2009.

[11] M. Stojanovic, "MIMO OFDM over Underwater Acoustic Channels," in *Proc. 43rd Asilomar Conference on Signals, Systems and Computers*, Pacific Grove, California, Nov. 2009, pp. 605–609.

[12] B. Li, S. Zhou, M. Stojanovic, L. Freitag, and P. Willett, "Multicarrier Communication over Underwater Acoustic Channels with Nonuniform Doppler Shifts," *IEEE Journal of Oceanic Engineering*, vol. 33, no. 2, pp. 198–209, Apr. 2008.

120

[13] X. Huang and H. Wu, "Robust and Efficient Intercarrier Interference Mitigation for OFDM Systems in Time-Varying Fading Channels," *IEEE Transactions on Vehicular Technology*, vol. 56, no. 5, pp. 2517–2528, Sep. 2007.

[14] I. F. Akyildiz, D. Pompili, and T. Melodia, "Underwater Acoustic Sensor Networks: Research Challenges," *Ad Hoc Networks (Elsevier)*, vol. 3, no. 3, pp. 257–279, May 2005.

[15] Z. Jiang, "Underwater Acoustic Networks – Issues and Solutions," *Int. J. Intelligent Ctrl. and Sys.*, vol. 13, no. 3, pp. 152–161, Sep. 2008.

[16] H. C. Song, W. S. Hodgkiss, W. A. Kuperman, T. Akal, and M. Stevenson, "Multiuser Communications using Passive Time Reversal," *IEEE Journal of Oceanic Engineering*, vol. 32, no. 4, pp. 915–926, Oct. 2007.

[17] M. Vayapeyam, S. Vedentam, U. Mitra, J. Preisig, and M.Stojanovic, "Distributed Space-Time Cooperative Schemes for Underwater Acoustic Communications," *IEEE Journal of Oceanic Engineering*, vol. 33, no. 4, pp. 489–501, Oct. 2008.

[18] G. Acar and A. E. Adams, "ACMENet: an Underwater Acoustic Sensor Network Protocol for Real-Time Environmental Monitoring in Coastal Areas," *IEE Proc., Radar Sonar Navig.*, vol. 153, no. 4, pp. 365–380, Aug. 2006.

[19] D. Pompili, T. Melodia, and I. F. Akyildiz, "A CDMA-based Medium Access Control Protocol for Underwater Acoustic Sensor Networks," *IEEE Trans. on Wireless Communications*, vol. 8, no. 4, pp. 1899–1909, Apr. 2009.

[20] M. Stojanovic, J. Catipovic, and J. G. Proakis, "Phase Coherent Digital Communications for Underwater Acoustic Channels," *IEEE Journal of Oceanic Engineering*, vol. 19, no. 1, pp. 100–111, Jan. 1994.

[21] E. Bejjani and J. C. Belfiore, "Multicarrier Coherent Communications for the Underwater Acoustic Channel," in *Proc. IEEE Oceans 1996*, Sep. 1996, pp. 1125–1130.

[22] J. Huang, S. Zhou, and P. Willett, "Nonbinary LDPC Coding for Multicarrier Underwater Acoustic Communication," *IEEE JSAC Special Issue on Underwater Wireless Communications and Networks*, vol. 26, no. 9, pp. 1684–1696, Dec. 2008.

[23] N. N. Soreide, C. E. Woody, and S. M. Holt, "Overview of Ocean Based Buoys and Drifters: Present Applications and Future Needs," in *Proc. IEEE Oceans 2001*, Honolulu, HI, Nov. 2001, pp. 2470 – 2472.

[24] X. Yang, K. G. Ong, W. R. Dreschel, K. Zeng, C. S. Mungle, and C. A. Grimes, "Design of a Wireless Sensor Network for Long-term, In-Situ Monitoring of an Aqueous Environment," *Sensors*, vol. 2, pp. 455–472, 2002.

[25] A. R. S. Bahai, B. R. Saltzberg, and M. Ergen, *Multi-Carrier Digital Communications: Theory and Applications of OFDM*. New York: Kluwer Academic/Plenum Publishers, 1999.

[26] L. Zou, Q. Chang, C. Xiu, and Q. Zhang, "Channel Estimation and ICI Cancellation for OFDM Systems in Fast Time-Varying Environments," *IEICE Transactions on Communications*, vol. E91-B, no. 4, pp. 1203–1206, Apr. 2008.

[27] S. J. Hwang and P. Schniter, "Efficient Multicarrier Communication for Highly Spread Underwater Acoustic Channels," *IEEE Journal on Selected Areas in Communication*, vol. 26, no. 9, pp. 1674–1683, Dec. 2008.

[28] W. S. Hou and B. S. Chen, "ICI Cancellation for OFDM Communication Systems in Time-Varying Multipath Fading Channels," *IEEE Transactions on Wireless Communications*, vol. 4, no. 5, pp. 2100–2110, 2005.

[29] A. F. Molisch, M. Toeltsch, and S. Vermani, "Iterative Methods for Cancellation of Intercarrier Interference in OFDM Systems," *IEEE Transactions on Vehicular Technology*, vol. 56, no. 4, pp. 2158–2167, Jul. 2007.

[30] S. Yerramalli and U. Mitra, "On Optimal Resampling for OFDM Signaling in Doubly-Selective Underwater Acoustic Channels," in *Proc. IEEE Oceans 2008*, Quebec City, Canada, Sep. 2008, pp. 1–6.

[31] C. Boulanger, G. Loubet, and J. R. Lequepeys, "Spreading Sequences for Underwater Multiple-Access Communications," in *Proc. IEEE 1998 OCEANS Conference*, Nice , France, Oct. 1998, pp. 1038–1042.

[32] S. Manohar, D. Sreedhar, V. Tikiya, and A. Chockalingam, "Cancellation of Multiuser Interference Due to Carrier Frequency Offsets in Uplink OFDMA," *IEEE Transactions on Wireless Communications*, vol. 6, no. 7, pp. 2560–2571, Jul. 2007.

[33] M. Morelli, C. C. J. Kuo, and M. Pun, "Synchronization Techniques for Orthogonal Frequency Division Multiple Access (OFDMA): A Tutorial Review," *Proc. of the IEEE*, vol. 95, no. 7, pp. 1394–1427, Jul. 2007.

[34] F. Bouabdallah and R. Boutaba, "A Distributed OFDMA Medium Access Control for Underwater Acoustic Sensors Networks," in *Proc. 2011 IEEE Int. Conf. on Communications*, Kyoto, Japan, Jun. 2011, pp. 1–5.

[35] M. Hayajneh, I. Khalil, and Y. Gadallah, "An OFDMA-Based MAC Protocol for Under Water Acoustic Wireless Sensor Networks," in *Proc. the 2009 International Conference on Wireless Communications and Mobile Computing*, Leipzig, Germany, Jun. 2009.

[36] J. Tao, Y. R. Zheng, and C. Xiao, "Channel Equalization for Single Carrier MIMO Underwater Acoustic Communications," *EURASIP Journal on Advances in Signal Processing*, vol. 2010, Jul. 2010, 17 pages.

[37] D. Gesbert, M. Kountouris, R. W. Heath, C. Chae, and T. Sälzer, "From Single User to Multiuser Communications: Shifting the MIMO Paradigm," vol. 24, no. 5, pp. 36–46, Oct. 2007.

[38] H. C. Song, J. S. Kim, W. S. Hodgkiss, W. A. Kuperman, and M. Stevenson, "High-Rate Multiuser Communications in Shallow Water," *J. Acoust. Soc. Am.*, vol. 128, no. 5, pp. 2920–2925, Nov. 2010.

[39] H. C. Song, P. Roux, W. S. Hodgkiss, W. A. Kuperman, T. Akal, and M. Stevenson, "Multiple-Input-Multiple-Output Coherent Time Reversal Communications in a Shallow-Water Acoustic Channel," *IEEE Journal of Oceanic Engineering*, vol. 31, no. 1, pp. 170–178, Jan. 2006.

[40] K. Tu, D. Fertonani, T. M. Duman, M. Stojanovic, J. G. Proakis, and P. Hursky, "Mitigation of Intercarrier Interference for OFDM over Time-Varying Underwater Acoustic Channels," *IEEE Journal of Oceanic Engineering*, vol. 3, no. 2, pp. 156–171, Apr. 2011.

[41] J. A. C. Bingham, "Multicarrier Modulation for Data Transmission: An Idea Whose Time Has Come," *Electron. Lett.*, vol. 28, pp. 5–14, May 1990.

[42] T. Wang, J. G. Proakis, and J. R. Zeidler, "Techniques for Suppression of Intercarrier Interference in OFDM Systems," in *Proc. IEEE Wireless Communications and Networking Conference*, Mar. 2005, pp. 39–49.

[43] L. Rugini, P. Banelli, and G. Leus, "Simple Equalization of Time-Varying Channels for OFDM," *IEEE Communications Letters*, pp. 619–621, Jul. 2005.

[44] Z. Tang, R. C. Cannizzaro, G. Leus, and P. Banelli, "Pilot-Assisted Time-Varying Channel Estimation for OFDM Systems," *IEEE Transactions on Signal Processing*, vol. 55, no. 5, pp. 2226–2238, May 2007.

[45] C. Tepedelenlioglu and G. B. Giannakis, "Blind Estimation and Equalization of Time- and Frequency-Selective Channels Using Filterbank Precoders," in *Proc. 32nd Asilomar Conf. on Signals, Systems, and Computers*, Pacific Grove, CA, Nov. 1998, pp. 1138–1142.

[46] K. Fang, L. Rugini, and G. Leus, "Iterative Channel Estimation and Turbo Equalization for Time-Varying OFDM Systems," in *Proc. IEEE Int. Conf. Acoustics, Speech and Signal Processing (ICASSP 2008)*, Las Vegas, Nevada, Mar. 2008, pp. 2909–2912.

[47] K. Fang *et al.*, "Low-Complexity Block Turbo Equalization for OFDM Systems in Time-Varying Channels," *IEEE Transactions on Signal Processing*, vol. 56, no. 11, pp. 5555–5566, Nov. 2008.

[48] L. Rugini, P. Banelli, and G. Leus, "Low-Complexity Banded Equalizers for OFDM Systems in Doppler Spread Channels," *EURASIP J. Appl. Signal Processing*, vol. 2006, pp. 1–13, 2006, Article ID 67404.

[49] P. Schniter, "Low-Complexity Equalization of OFDM in Doubly Selective Channels," *IEEE Transactions on Signal Processing*, vol. 52, no. 4, pp. 1002–1011, Apr. 2004.

[50] S. Mason, C. R. Berger, S. Zhou, K. R. Ball, L. Freitag, and P. Willett, "Receiver Comparisons on an OFDM Design for Doppler Spread Channels," in *Proc. MTS/IEEE Oceans*, Bremen, Germany, May 2009.

[51] C. R. Berger, S. Zhou, J. Preisig, and P. Willett, "Sparse Channel Estimation for Multicarrier Underwater Acoustic Communication: From Subspace Methods to Compressed Sensing," *IEEE Transactions of Signal Processing*, vol. 58, no. 3, pp. 1708–1721, Mar. 2010.

[52] J. J. van de Beek, M. Sandell, and P. O. Borjesson, "ML Estimation of Time and Frequency Offset in OFDM Systems," *IEEE Transactions on Signal Processing*, vol. 45, no. 7, pp. 1800–1805, Jul. 1997.

[53] S. Coleri, M. Ergen, A. Puri, and A. Bahai, "Channel Estimation Techniques Based on Pilot Arrangement in OFDM Systems," *IEEE Trans. Broadcast.*, vol. 48, no. 3, pp. 223–229, Nov. 2002.

[54] M. Hsieh and C. Wei, "Channel Estimation for OFDM Systems Based on Comb-Type Pilot Arrangement in Frequency Selective Fading Channels," *IEEE Trans. Consumer Electronics*, vol. 44, no. 1, pp. 217–225, Feb. 1998.

[55] S. Das and P. Schniter, "Max-SINR ISI/ICI-Shaping Multicarrier Communication over the Doubly Dispersive Channel," *IEEE Transactions on Signal Processing*, vol. 55, no. 12, pp. 5782–5795, Dec. 2007.

[56] M. Hampejs, P. Svac, G. Tauböck, K. Gröchenig, F. Hlawatsch, and G. Matz, "Sequential LSQR-based ICI Equalization and Decision-Feedback ISI Cancellation

in Pulse-Shaped Multicarrier Systems," in *Proc. IEEE SPAWC 2009*, Perugia, Italy, Jun. 2009.

[57] U. Mengali and A. N. D'Andrea, *Synchronization Techniques for Digital Receivers*. Plenum Press, 1997.

[58] A. Goldsmith, *Wireless Communications*. Cambridge University Press, 2005.

[59] A. Radosevic, J. Proakis, and M. Stojanovic, "Statistical Characterization and Capacity of Shallow Water Acoustic Channels," in *Proc. IEEE Oceans 2009*, Bremen, Germany, May 2009.

[60] W. Yu and W. Rhee, "Degrees of Freedom in Wireless Multiuser Spatial Multiplex Systems with Multiple Antennas," *IEEE Transactions on Communications*, vol. 54, no. 10, pp. 1747–1753, 2006.

[61] Q. H. Spencer, A. L. Swindlehurst, and M. Haardt, "Zero-Forcing Methods for Downlink Spatial Multiplexing in Multiuser MIMO Channels," *IEEE Trans. Signal Processing*, vol. 52, no. 2, pp. 461–471, 2004.

[62] N. H. Dawod, R. Hafez, and I. Marsland, "Uplink Multiuser MIMO-OFDM in Widely Spaced Antenna Arrays," in *Proc. Canadian Conference on Electrical and Computer Engineering*, May 2005, pp. 155–159.

[63] S. Venkatesan, A. Lozano, and R. Valenzuela, "Network MIMO: Overcoming Intercell Interference in Indoor Wireless Systems," in *Proc. 41st Asilomar Conf. on Signals, Systems, and Computers*, Pacific Grove, CA, Nov. 2007, pp. 83–87.

[64] K. Tu, D. Fertonani, and T. M. Duman, "OFDM Receiver for Underwater Acoustic Channels with Non-Uniform Doppler Arrivals," in *Proceedings of the 10th European Conference on Underwater Acoustics*, Istanbul, Turkey, Jul. 2010, pp. 973–978.

[65] K. Tu, T. M. Duman, J. G. Proakis, and M. Stojanovic, "Cooperative MIMO-OFDM Communications: Receiver Design for Doppler Distorted Underwater Acoustic Channels," in *Proc. Asilomar Conf. on Signals, Systems, and Computers*, Pacific Grove, CA, Nov. 2010.

[66] W. Li and J. C. Presig, "Estimation of Rapidly Time-Varying Sparse Channels," *IEEE Journal of Oceanic Engineering*, vol. 32, no. 4, pp. 927–939, Oct. 2007.

[67] K. Davidson, "MACE10 - Mobile Acoustic Communications Experiment 2010 — Quick-Look Cruise Report," Tech. Rep., Aug. 2010.

[68] T. M. Duman and A. Ghrayeb, *Coding for MIMO Communication Systems*. New York: John Wiley and Sons, Inc., 2007.

[69] G. H. Golub and C. F. V. Loan, *Matrix Computations*, 3rd ed. Baltimore: Johns Hopkins University Press, 1999.

[70] S. J. Wright, R. D. Nowak, and M. A. T. Figueiredo, "Sparse Reconstruction by Separable Approximation," *IEEE Transactions on Signal Processing*, vol. 57, no. 7, pp. 2479 – 2493, Jul. 2009.

[71] Y. Chi, L. L. Scharf, A. Pezeshki, and A. R. Calderbank, "Sensitivity to Basis Mismatch in Compressed Sensing," *IEEE Transactions on Signal Processing*, vol. 59, no. 5, pp. 2182–2195, Feb. 2011.

[72] S. Haykin, *Adaptive Filter Theory*, 4th ed. Prentice Hall, 2001.

[73] G. D. Forney, Jr., "Maximum-Likelihood Sequence Estimation of Digital Sequences in the Presence of Intersymbol Interference," *IEEE Transactions on Information Theory*, vol. 18, no. 3, pp. 363–379, 1972.

[74] K. Tu, T. M. Duman, M. Stojanovic, and J. G. Proakis, "OFDMA for Underwater Acoustic Communications," in *Forty-Ninth Annual Allerton Conference*, Urbana-Champaign, IL, Sep. 2010, invited paper.

[75] D. J. C. Mackay, "Good Error-Correcting Codes Based on Very Sparse Matrices," *IEEE Trans. on Information Theory*, vol. 45, no. 2, pp. 399–431, Mar. 1999.

[76] A. P. Kannu and P. Schniter, "On the Spectral Efficiency of Noncoherent Doubly Selective Block-Fading Channels," *IEEE Transactions on Information Theory*, vol. 56, no. 6, pp. 2829–2844, Jun. 2010.

[77] U. Salim and D. Slock, "Asymptotic Capacity of Underspread and Overspread Stationary Time- and Frequency-Selective Channels," in *Proc. Information Theory and Applications Workshop*, San Diego, CA, Jan. 2008, pp. 562–570.

[78] E. Zwecher and D. Porrat, "Training over Sparse Multipath Channels in the Low SNR Regime," Tech. Rep., Jan. 2010, arXiv:1001.4382v1.

[79] A. P. Kannu and P. Schniter, "On Communication over Unknown Sparse Frequency-Selective Block-Fading Channels," Tech. Rep., Jun. 2010, arXiv:1006.1548.

[80] S. Shamai, H. A. Ozarow, and A. D. Wyner, "Information Rates for a Discrete-Time Gaussian Channel with Intersymbol Interference and Stationary Inputs," *IEEE Trans. on Inform. Theory*, vol. 37, pp. 1527–1539, Nov. 1991.

[81] Z. Zhang, T. M. Duman, and E. M. Kurtas, "Achievable Information Rates and Coding for MIMO Systems over ISI Channels and Frequency-Selective Fading

Channels," *IEEE Transactions on Communications*, vol. 52, no. 10, pp. 1698–1710, 2004.

[82] A. Radosevic, D. Fertonani, T. M. Duman, J. G. Proakis, and M. Stojanovic, "Bounds on the Information Rate for Sparse Channels with Long Memory and i.u.d. Inputs," to appear in IEEE Transactions on Communications in 2012.

[83] W. U. Bajwa, A. M. Sayeed, and R. Nowak, "Learning Sparse Doubly-Selective Channels," in *Proc. 46th Annu. Allerton Conf. Communication, Control, and Computing*, Monticello, IL, Sep. 2008, pp. 575–582.

[84] H.Bölcskei, D. Gesbert, and A. J. Paulraj, "On the Capacity of OFDM-Based Spatial Multiplexing Systems," *IEEE Transactions on Communications*, vol. 50, no. 2, pp. 225–234, Feb. 2002.

APPENDIX A

RECEIVER DESIGN FOR USER AND PATH-SPECIFIC DOPPLER

With the cases of the path-specific and the user-specific Doppler discussed individually, it is straightforward to extend their results to more general scenarios, where both user-specific and path-specific Doppler distortions exist. Defining $a_c^{(i)}$ the user and path-specific Doppler scaling factor of the c-th cluster's arrivals (see Figure A.1), the input-output relationship between the ith transmitter and the mth receiver can be written as

$$y_{i,m}(t) = \sum_{c=0}^{M_c-1} \sum_{p=0}^{N_{c,p}^{(i,m)}-1} h_{c,p}^{(i,m)} s_i \left(t + a_c^{(i,m)}t - \tau_{c,p}^{(i,m)} \right) \tag{A.1}$$

where M_c is the largest number of clusters among all transmitter-receiver pairs, $N_{c,p}^{(i,m)}$ is the number of paths in each cluster, and $h_{c,p}^{(i,m)}$ and $\tau_{c,p}^{(i,m)}$ are respectively the path gain and delay of the pth path in a cluster. The corresponding baseband received signals can be formulated as

$$v_m(t) = \sum_{i=1}^{N_t} \sum_{k=0}^{N-1} d_k^{(i)} P_k^{(i,m)}(t) + w_m(t) \tag{A.2}$$

where m is the index of receiving element, $w_m(t)$ is a circularly-symmetric complex AWGN with power spectral density (PSD) N_0, and

$$P_k^{(i,m)}(t) = \sum_{c=0}^{M_c-1} \sum_{p=0}^{N_{c,p}^{(i,m)}-1} \alpha_{c,p}^{(i,m)}(k) e^{j2\pi a_c^{(i,m)} f_0 t} e^{j2\pi \left(t+a_c^{(i,m)} t \right) k/T} R \left(t + a_c^{(i,m)}t - \tau_{c,p}^{(i,m)} \right) \tag{A.3}$$

with $\alpha_{c,p}^{(i,m)}(k) = h_{c,p}^{(i,m)} e^{-j2\pi f_k \tau_{c,p}^{(i,m)}}$.

Following the same process as described in Sections 4.3 and 4.4, a set of desired sufficient statistics can be derived, which yield a similar multiple resampling structure, with each resampling branch corresponding to a unique path and user-specific Doppler scaling factor $a_c^{(i,m)}$ as shown in Figure A.2. Here, the sufficient statistics are given by

$$y_k^{(i,m)} \approx \sum_{c=0}^{M_c-1} \alpha_c^{(i,m)}(k)^* \int_0^T v_m^{(i,c)} \left(\frac{\xi}{1+a_c^{(i,m)}} \right) e^{-j2\pi k\xi/T} d\xi \tag{A.4}$$

where

$$v_m^{(i,c)}(t) = v_m(t) e^{-j2\pi a_c^{(i,m)} f_0 t} \tag{A.5}$$

and,

$$\alpha_c^{(i,m)}(k) = \sum_{p=0}^{N_{c,p}^{(i,m)}-1} \frac{\alpha_{c,p}^{(i,m)}(k)}{1+a_c^{(i,m)}}. \tag{A.6}$$
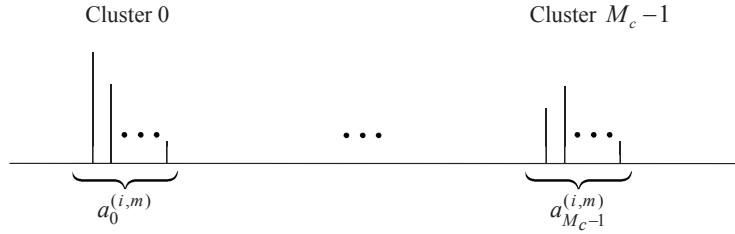
129

Figure A.1: Clusters with path and user-specific Doppler scaling factors for the transmitter-receiver pair (i,m).
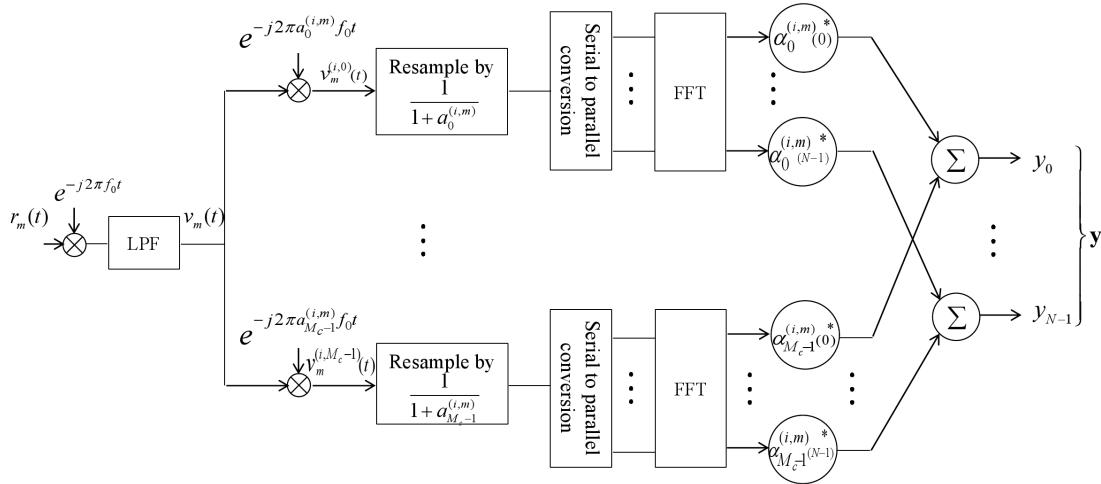
Figure A.2: The multiple-resampling front-end for the mth receiving element and the ith user.

To exploit the benefits of the sufficient statistics, one can employ similar data detection schemes as those in Section 4.4. We point out that with the addition of the path-specific Doppler, the channel matrix characterizing these sufficient statistics contains both cross-user terms and self-ICI terms. Therefore, the ML detector is computationally unaffordable even in its approximate form. One can easily extend the linear detectors developed in Section 4.4 for data detection, however, we know that they are suboptimal in terms of minimizing error rates. Thus, we focus on the extension of the interference cancellation based scheme that is shown to be a good compromise between performance and complexity.

The modified interference cancellation scheme follows a similar iterative procedure as that in Section 4.4. The difference is that for the generalized case, after the

estimate of cross-user interference

$$\mathbf{I}_n(1,m) = \sum_{i=2}^{N_t} \boldsymbol{\Phi}^{(1,i)}(m)\tilde{\mathbf{d}}_{IC}^{(i)}(n-1)$$

is subtracted from the desired signal, i.e.

$$\mathbf{z}_n(1,m) = \mathbf{y}(1,m) - \mathbf{I}_n(1,m) \qquad (\text{A.7})$$

due to the Doppler scaling factor difference among different paths, there will still be some residual self-ICI. However, note that assuming perfect cross-user interference cancelation, this residual ICI only contains the contribution from the desired user itself. In other words, for the co-channel interference (CCI)-removed signal $\mathbf{z}_n(1,m)$, the single-user model in Section 4.3.2.1 will apply, i.e.,

$$\mathbf{z}_n(1,m) = \boldsymbol{\Phi}^{(1,1)}(m)\mathbf{d}^{(1)} + \mathbf{w}(1,m). \qquad (\text{A.8})$$

Grouping all the CCI-removed signals $\mathbf{z}_n(1,m)$ together, we have the aggregate signal model

$$\underbrace{\begin{bmatrix} \mathbf{z}_n(1,1) \\ \mathbf{z}_n(1,2) \\ \dots \\ \mathbf{z}_n(1,N_r) \end{bmatrix}}_{\mathbf{z}_n^{(1)}} = \underbrace{\begin{bmatrix} \boldsymbol{\Phi}^{(1,1)}(1) \\ \boldsymbol{\Phi}^{(1,1)}(2) \\ \dots \\ \boldsymbol{\Phi}^{(1,1)}(N_r) \end{bmatrix}}_{\boldsymbol{\Phi}^{(1,1)}} \mathbf{d}^{(1)} + \underbrace{\begin{bmatrix} \mathbf{w}(1,1) \\ \mathbf{w}(1,2) \\ \dots \\ \mathbf{w}(1,N_r) \end{bmatrix}}_{\mathbf{w}(1)} \qquad (\text{A.9})$$

where the noise vector $\mathbf{w}(1)$ is characterized by its covariance matrix

$$\boldsymbol{\Omega}^{(1)} = \begin{bmatrix} \boldsymbol{\Omega}^{(1,1)}(1) & \mathbf{0} & \dots & \mathbf{0} \\ \mathbf{0} & \boldsymbol{\Omega}^{(1,1)}(2) & \dots & \mathbf{0} \\ \mathbf{0} & \mathbf{0} & \ddots & \mathbf{0} \\ \mathbf{0} & \mathbf{0} & \dots & \boldsymbol{\Omega}^{(1,1)}(N_r) \end{bmatrix}.$$

We thus adopt the linear detectors used by the single-user case to form symbol decisions of $\mathbf{d}^{(1)}$. If the LS detector is to be applied, we use

$$\tilde{\mathbf{d}}_{LS}^{(1)}(n) = \text{Dec}\left(\left(\boldsymbol{\Phi}^{(1,1)\,\mathrm{H}} \boldsymbol{\Phi}^{(1,1)} \right)^{-1} \boldsymbol{\Phi}^{(1,1)\,\mathrm{H}} \mathbf{z}_n(1) \right) \qquad (\text{A.10})$$

and if the MMSE detector is to be applied, we use

$$\tilde{\mathbf{d}}_{\mathrm{MMSE}}^{(1)}(n) = \mathrm{Dec}\left(\boldsymbol{\Phi}^{(1,1)\,\mathrm{H}}\left(\boldsymbol{\Phi}^{(1,1)}\boldsymbol{\Phi}^{(1,1)\,\mathrm{H}} + \boldsymbol{\Omega}^{(1)}\right)^{-1}\mathbf{z}_n(1)\right). \qquad (\mathrm{A.11})$$

The interference cancellation based estimation/detection process is performed iteratively and is identical for all the other users. Just as the initialization process used by Section 4.4.2.3, the modified IC detector is initialized by symbol decisions obtained using one of the linear detectors discussed previously.

APPENDIX B

NOISE CROSS-CORRELATION FOR THE MR RECEIVER

The noise correlation $\mathrm{E}\left[\eta_k \eta_m^*\right]$ can be written as

$$
\begin{aligned}
\mathrm{E}\left[\eta_k \eta_m^*\right] &= \int_0^T \int_0^T \mathrm{E}\left[u(t)u^*(\tau)\right] P_k^*(t)P_m(\tau)dtd\tau \\
&= \int_0^T \int_0^T \mathrm{E}\left[u(t)u^*(\tau)\right] \sum_{p=0}^{N_p-1} \alpha_{p,k}^* e^{-j2\pi f_k(1+a_p)t} \\
&\qquad\qquad\qquad \times \sum_{q=0}^{N_p-1} \alpha_{q,k} e^{j2\pi f_m(1+a_q)\tau} dtd\tau, \qquad (B.1)
\end{aligned}
$$

where the autocorrelation of the noise process $u(t)$ is given by the inverse Fourier transform of its power spectral density $S_w(f)$, i.e.,

$$
\begin{aligned}
\mathrm{E}\left[u(t)u^*(\tau)\right] &= \int_{-\infty}^{\infty} S_w(f) e^{j2\pi f(t-\tau)} df \\
&= \int_{-\frac{B}{2}}^{\frac{B}{2}} N_0 e^{j2\pi f(t-\tau)} df \\
&= g(t-\tau). \qquad (B.2)
\end{aligned}
$$

Substituting Equation (B.2) into (B.1), we rewrite Equation (B.1) as

$$
\begin{aligned}
\mathrm{E}\left[\eta_k \eta_m^*\right] &= \sum_{p=0}^{N_p-1} \sum_{q=0}^{N_p-1} \alpha_{p,k}^* \alpha_{q,m} \int_0^T e^{-j2\pi f_k(1+a_p)t} \underbrace{\left[\int_0^T g(t-\tau) e^{j2\pi f_m(1+a_q)\tau} d\tau\right]}_{\theta_m'(t)} dt \\
&= \sum_{p=0}^{N_p-1} \sum_{q=0}^{N_p-1} \alpha_{p,k}^* \alpha_{q,m} \int_0^T e^{-j2\pi f_k' t} \mathcal{F}^{-1}\left\{\Theta_m'(f)\right\} dt \qquad (B.3)
\end{aligned}
$$

where $f_k' = (1+a_p)f_k$ and $f_m' = (1+a_q)f_m$ are respectively the Doppler-shifted subcarrier frequencies of the m-th and the k-th transmitted symbols, and $\theta_m'(t)$ is the filtered version of the frequency-shifted subcarrier with index m. Here, the frequency response of the filter $g(t)$ is given by the power spectral density of $u(t)$, which yields the frequency domain representation of $\theta_m'(t)$ as

$$
\Theta_m'(f) = \begin{cases} N_0 T \cdot \mathrm{sinc}\left(\pi(f-f_m')T\right) e^{-j\pi(f-f_m')T}, & f \in \left[-\frac{B}{2}, \frac{B}{2}\right], \\ 0, & \text{elsewhere.} \end{cases} \qquad (B.4)
$$

Note that the integral in the expression (B.3) can be interpreted as the cross-correlation between the k-th frequency-shifted subcarrier and the filtered version of the m-th frequency-shifted subcarrier. Defining the frequency domain representations of the k-th

134

and the m-th subcarriers as

$$\Psi'_k(f) = T \cdot \text{sinc}\left(\pi(f - f'_k)T\right) e^{-j\pi(f-f'_k)T}, \tag{B.5}$$

and,

$$\Psi'_m(f) = T \cdot \text{sinc}\left(\pi(f - f'_m)T\right) e^{-j\pi(f-f'_m)T}, \tag{B.6}$$

we can re-write the cross-correlation in the integral in the frequency domain, which effectively yields

$$\begin{aligned}
\text{E}\left[\eta_k \eta_m^*\right] &= N_0 \sum_{p=0}^{N_p-1} \sum_{q=0}^{N_p-1} \alpha_{p,k}^* \alpha_{q,m} \int_{-\frac{B}{2}}^{\frac{B}{2}} \Psi'_k(f)\Psi'_m(f)df \\
&\approx N_0 \sum_{p=0}^{N_p-1} \sum_{q=0}^{N_p-1} \alpha_{p,k}^* \alpha_{q,m} \int_{-\infty}^{\infty} \Psi'_k(f)\Psi'_m(f)df
\end{aligned} \tag{B.7}$$

where the approximation is accurate if $\frac{B}{2} - f_{N-1} \gg 1/T$, such that the distortion on the m-th subcarrier (caused by the lowpass filtering through $g(t)$) can be neglected for all the subcarrier frequencies including the highest one.

To compute Equation (B.7), we explicitly write the time domain representations of $\Psi'_k(f)$ and $\Psi'_m(f)$, i.e.,

$$\psi'_k(t) = \begin{cases} e^{j2\pi f'_k t}, & t \in [0,T] \\ 0, & \text{elsewhere} \end{cases} \tag{B.8}$$

and

$$\psi'_m(t) = \begin{cases} e^{j2\pi f'_m t}, & t \in [0,T] \\ 0, & \text{elsewhere} \end{cases} \tag{B.9}$$

and then evaluate the noise correlation using these time domain expressions, i.e.,

$$\begin{aligned}
\text{E}\left[\eta_k \eta_m^*\right] &\approx N_0 \sum_{p=0}^{N_p-1} \sum_{q=0}^{N_p-1} \alpha_{p,k}^* \alpha_{q,m} \int_{-\infty}^{\infty} \psi'_k(-t)\psi'_m(t)dt \\
&= N_0 \sum_{p=0}^{N_p-1} \sum_{q=0}^{N_p-1} \alpha_{p,k}^* \alpha_{q,m} \int_0^T e^{-j2\pi f'_k t} e^{j2\pi f'_m t}dt \\
&= N_0 \Phi_{k,m}.
\end{aligned} \tag{B.10}$$

Note that $\Phi_{k,m}$ in general has both non-zero diagonal and off-diagonal elements, rendering a set of colored noise $\{\eta_k\}$, whose pair-wise correlation is the ICI coefficient $\Phi_{k,m}$ scaled by the noise PSD N_0.

APPENDIX C

DISCRETE CHANNEL MODELS WITH GENERALIZED MODULATION PULSE

In this Appendix, we discuss the discrete channel models for the capacity characterization of pulse-shaped multi-carrier communications. In these cases, the transmitted signal can be written as

$$s(t) = \text{Re} \left\{ \sum_{k=0}^{N-1} d_k e^{j2\pi f_k t} \tilde{R}(t) \right\} \tag{C.1}$$

where $\tilde{R}(t)$ is an arbitrary shaping pulse with duration $T + T_g$, and the definitions of other parameters are the same as those in Equation (6.1). Following a similar procedure as in Section 6.2, we can write the lowpass equivalent of the CP-removed received signal as

$$y_g(t) = v_g(t) + n(t) \tag{C.2}$$

where

$$v_g(t) = \sum_{p=0}^{N_p-1} \sum_{k=-N/2}^{N/2-1} \alpha_{p,k} d_k e^{j2\pi k(1+a_p)/T} e^{j2\pi a_p f_c t} \tilde{R}_p(t) \tag{C.3}$$

and $n(t)$ is the in-band noise with power spectral density N_0. Unlike Equation (6.3), for which the explicit modulation pulse is omitted (since it has unity magnitude over the observation window $[0, T]$), the explicit modulation pulse $\tilde{R}_p(t)$ is incorporated into the signal arrivals in the definition of $v_g(t)$, where $\tilde{R}_p(t)$ is path-specific and can be written as

$$\tilde{R}_p(t) = \begin{cases} \tilde{R}\left(t + a_p t - \tau_p\right), & t \in [0, T] \\ 0, & \text{elsewhere} \end{cases} \tag{C.4}$$

The change in the signal arrivals results in different channel matrices for both the MR and the SR receivers, while in terms of the noise cross-correlation, only the MR receiver is affected. In particular, following a procedure in parallel to that in Section 6.3, the new channel matrix for the SR receiver is given as

$$H_{k,m}^g = \int_0^T e^{-j2\pi[(k-m)/T + a_p f_m]t} \tilde{R}_p(t) dt. \tag{C.5}$$

Here, since $\tilde{R}_p(t)$ is strictly time-limited within the duration $[0, T]$, we can let the integration interval go to infinity and perceive Equation (C.5) as a Fourier transform

138

evaluated at zero frequency, i.e.,

$$
\begin{aligned}
H_{k,m}^g &= \left\{ \int_{-\infty}^{\infty} e^{-j2\pi[(k-m)/T + a_p f_m]t} \tilde{R}_p(t) e^{-j2\pi ft} dt \right\}_{f=0} \\
&= \tilde{R}_p^f(-(k-m)/T - a_p f_m)
\end{aligned}
\tag{C.6}
$$

where the second equality holds since the Fourier transform of the time-domain multiplication equals the frequency domain convolution of the two signals involved in the multiplication. Note that the effect of the convolution is to shift $\tilde{R}_p^f(f)$, the frequency domain representation of $\tilde{R}_p(t)$, $(k-m)/T + a_p f_m$ Hz to the right.

As far as the MR receiver is concerned, following a similar procedure as in Section 6.4, we start by writing the new equivalent modulation pulse as

$$
P_k^g(t) = \sum_{p=0}^{N_p-1} \alpha_{p,k} e^{j2\pi a_p f_0 t} e^{j2\pi k \Delta f (1+a_p) t} \tilde{R}_p(t),
\tag{C.7}
$$

We then adopt matched-filtering [64] and substitute the modulation pulse in the expression with Equation (C.7), which yields a new discrete channel model as

$$
\begin{aligned}
z_k^g &= \int_0^T y(t) \sum_{p=0}^{N_p-1} \alpha_{p,k}^* e^{-j2\pi a_p f_0 t} e^{-j2\pi k \Delta f (1+a_p) t} \tilde{R}_p(t) dt \\
&= \sum_{m=0}^{N-1} \Phi_{k,m}^g d_m + \eta_k^g,
\end{aligned}
\tag{C.8}
$$

where

$$
\begin{aligned}
\Phi_{k,m}^g &= \int_{-\infty}^{\infty} P_m^g(t) P_k^g(t)^* dt \\
&= \sum_{p=0}^{N_p-1} \sum_{q=0}^{N_p-1} \alpha_{p,k}^* \alpha_{q,m} \int_0^T e^{-j2\pi(1+a_p)f_k t} e^{-j2\pi(1+a_q)f_m t} \tilde{R}_p(t) \tilde{R}_q(t) dt
\end{aligned}
\tag{C.9}
$$

The noise correlation can be assessed using a procedure analogous to that of Appendix B, i.e., it can be approximated by the corresponding ICI coefficient scaled by N_0, i.e.,

$$
\mathrm{E}\left[\eta_k^g \eta_m^{g\,*} \right] \approx N_0 \Phi_{k,m}^g.
\tag{C.10}
$$

Here, the details of the derivation are omitted – interested readers are advised to review the material in Appendix B.

APPENDIX D

DISCRETE CHANNEL MODELS WITH COLORED NOISE POWER SPECTRUM

For channels with colored noise, we adopt a general noise PSD $N(f)$ instead of N_0 for Equation (6.2). Note that the MR receivers are developed under the assumption of white Gaussian noise. To make these receivers applicable for the case of colored noise, we whiten the noise using the whitening filter with frequency response $H_w(f) = \sqrt{N_0/2N(f)}$. We point out that in addition to shaping the noise, whitening filter also changes the magnitude of each frequency-shifted subcarriers in the signal arrivals. For instance, the k-th subcarrier in the p-th arrival

$$
\begin{aligned}
s_{p,k}(t) &= h_p d_k e^{j2\pi f_k(t+a_p t-\tau_p)} \\
&= \alpha_{p,k} e^{j2\pi f'_{p,k} t} d_k,
\end{aligned}
\tag{D.1}
$$

is scaled by the frequency response of the whitening filter evaluated at $f'_{p,k} = (1+a_p) f_k$, to produce $s^w_{p,k}(t) = H_w(f'_{p,k}) s_{p,k}(t)$. We can thus write the whitened signal as

$$
r_w(t) = \sum_{p=0}^{N_p-1} h_p \sum_{k=-N/2}^{N/2-1} H_w(f'_{p,k}) d_k e^{j2\pi f_k(t+a_p t-\tau_p)} R(t+a_p t - \tau_p) + u_w(t), \tag{D.2}
$$

where $w(t)$ is additive white Gaussian noise with power spectral density $N_0/2$. After perfect timing synchronization and cyclic prefix removal, we can write the lowpass equivalent of the resulting signal as

$$
y_w(t) = v_w(t) + n(t) \tag{D.3}
$$

where

$$
v_w(t) = \sum_{p=0}^{N_p-1} \sum_{k=-N/2}^{N/2-1} \underbrace{H_w(f'_{p,k}) \alpha_{p,k}}_{\alpha^w_{p,k}} d_k e^{j2\pi k(1+a_p)/T} e^{j2\pi a_p f_c t} \tag{D.4}
$$

and $n(t)$ is the in-band noise with power spectral density N_0. With the new lowpass equivalent model in Equation (D.3), it is straightforward to find out the discrete channel models for the MR and SR receivers following the same procedure as in Section 6.4 and 6.3. The details are omitted.